

Supporting Information
for
**Nuclear Resonance Vibrational Spectroscopic (NRVS)
Definition of the Fe(IV)₂ Intermediate Q in Methane
Monooxygenase and its Reactivity**

Ariel Benjamin Jacobs,^a Rahul Banerjee,^b Dory Ellen Deweese,^a Augustin Braun,^a Jeffrey Thomas Babicz, Jr.,^a Leland Bruce Gee,^a Kyle David Sutherlin,^a Lars Hendrik Böttger,^a Yoshitaka Yoda,^c Makina Saito,^d Shinji Kitao,^e Yasuhiro Kobayashi,^e Makoto Seto,^e Kenji Tamasaku,^f John D. Lipscomb,^{b,*} Kiyoun Park,^{g,*} Edward I. Solomon^{a,h,*}

^aDepartment of Chemistry, Stanford University, 333 Campus Drive, Stanford, California, 94305, United States

^bDepartment of Biochemistry, Molecular Biology and Biophysics, University of Minnesota, Minneapolis, Minnesota 55391 U.S.A.

^cJapan Synchrotron Radiation Research Institute, Hyogo 679-5198, Japan

^dDepartment of Physics, Graduate School of Science, Tohoku University, Sendai, Miyagi 980-8578 Japan

^eInstitute for Integrated Radiation and Nuclear Science, Kyoto University, Osaka, 590-0494

^fRIKEN SPring-8 Center, RIKEN, Sayo, Hyogo, 679-5148, Japan

^gDepartment of Chemistry, Korea Advanced Institute of Science and Technology (KAIST), Daejeon 34141, Republic of Korea

^hStanford Synchrotron Radiation Light Source, SLAC National Accelerator Laboratory, Stanford University, Menlo Park, California, 94025, United States

Supporting Information References

- (1) Banerjee, R.; Meier, K. K.; Münck, E.; Lipscomb, J. D. Intermediate P* from Soluble Methane Monooxygenase Contains a Diferrous Cluster. *Biochemistry* **2013**, *52* (25), 4331–4342. <https://doi.org/10.1021/bi400182y>.
- (2) Banerjee, R.; Komor, A. J.; Lipscomb, J. D. *Use of Isotopes and Isotope Effects for Investigations of Diiron Oxygenase Mechanisms*, 1st ed.; Elsevier Inc., 2017; Vol. 596. <https://doi.org/10.1016/bs.mie.2017.07.016>.
- (3) Castillo, R. G.; Banerjee, R.; Allpress, C. J.; Rohde, G. T.; Bill, E.; Que, L.; Lipscomb, J. D.; DeBeer, S. High-Energy-Resolution Fluorescence-Detected X-Ray Absorption of the Q Intermediate of Soluble Methane Monooxygenase. *J. Am. Chem. Soc.* **2017**, *139* (49), 18024–18033. <https://doi.org/10.1021/jacs.7b09560>.
- (4) Dassama, L. M. K.; Yosca, T. H.; Conner, D. A.; Lee, M. H.; Streit, B. R.; Green, M. T.; Dubois, J. L.; Krebs, C.; Bollinger, J. M. O₂-Evolving Chlorite Dismutase as a Tool for Studying O₂-Utilizing Enzymes. *Biochemistry* **2012**, *51*, 1607.
- (5) Gunnlaugsson, H. P. Spreadsheet Based Analysis of Mössbauer Spectra. *Hyperfine Interact.* **2016**, *237* (1), 13–18. <https://doi.org/10.1007/s10751-016-1271-z>.
- (6) Smith, M. C.; Xiao, Y.; Wang, H.; George, S. J.; Coucouvanis, D.; Koutmos, M.; Sturhahn, W.; Alp, E. E.; Zhao, J.; Cramer, S. P. Normal-Mode Analysis of FeCl₄⁻ and Fe₂S₂Cl₄²⁻ via Vibrational Mossbauer, Resonance Raman, and FT-IR Spectroscopies. *Inorg. Chem.* **2005**, *44* (16), 5562–5570.
- (7) Sturhahn, W. CONUSS and PHOENIX: Evaluation of Nuclear Resonant Scattering Data. *Hyperfine Interact.* **2000**, *125*, 149–172. <https://doi.org/10.1023/A:1012681503686>.
- (8) Gee, L. B.; Wang, H.; Cramer, S. P. *NRVS for Fe in Biology: Experiment and Basic Interpretation*, 1st ed.; Elsevier Inc., 2018; Vol. 599. <https://doi.org/10.1016/bs.mie.2017.11.002>.
- (9) Lee, S. J.; McCormick, M. S.; Lippard, S. J.; Cho, U.-S. Control of Substrate Access to the Active Site in Methane Monooxygenase. *Nature* **2013**, *494* (7437), 380–384. <https://doi.org/10.1038/nature11880>.
- (10) Frisch, J. M. et al. No Title. *Gaussian 16, Revis. C.01* Gaussian Inc.: Wallington CT.
- (11) Frisch, J. M. et al. No Title. *Gaussian 09, Revis. E.01* Gaussian Inc.: Wallington CT.
- (12) Becke, A. D. Density-Functional Exchange-Energy Approximation with Correct Asymptotic Behavior. *Phys. Rev. A* **1988**, *38*, 3098–3100. <https://doi.org/10.1063/1.1749835>.
- (13) Park, K.; Bell, C. B.; Liu, L. V.; Wang, D.; Xue, G.; Kwak, Y.; Wong, S. D.; Light, K. M.; Zhao, J.; Alp, E. E.; Yoda, Y.; Saito, M.; Kobayashi, Y.; Ohta, T.; Seto, M.; Que, L.; Solomon, E. I. Nuclear Resonance Vibrational Spectroscopic and Computational Study of

- High-Valent Diiron Complexes Relevant to Enzyme Intermediates. *Proc. Natl. Acad. Sci. U. S. A.* **2013**, *110* (16), 6275–6280. <https://doi.org/10.1073/pnas.1304238110>.
- (14) Park, K.; Tsugawa, T.; Furutachi, H.; Kwak, Y.; Liu, L. V.; Wong, S. D.; Yoda, Y.; Kobayashi, Y.; Saito, M.; Kurokuzu, M.; Seto, M.; Suzuki, M.; Solomon, E. I. Nuclear Resonance Vibrational Spectroscopy and DFT Study of Peroxo-Bridged Biferric Complexes: Structural Insight into Peroxo Intermediates of Binuclear Non-Heme Iron Enzymes. *Angew. Chemie - Int. Ed.* **2013**, *52* (4), 1294–1298. <https://doi.org/10.1002/anie.201208240>.
- (15) Tomasi, J.; Mennucci, B.; Cammi, R. Quantum Mechanical Continuum Solvation Models. *Chem. Rev.* **2005**, *105* (8), 2999–3093. <https://doi.org/10.1021/cr9904009>.
- (16) Becke, A. D. Density-Functional Thermochemistry. III. The Role of Exact Exchange. *J. Chem. Phys.* **1993**, *98* (7), 5648–5652. <https://doi.org/10.1063/1.464913>.
- (17) Park, K.; Solomon, E. I. Modeling Nuclear Resonance Vibrational Spectroscopic Data of Binuclear Nonheme Iron Enzymes Using Density Functional Theory. *Can. J. Chem.* **2014**, *92*, 975. <https://doi.org/10.1139/cjc-2014-0067>.
- (18) Yanai, T.; Tew, D. P.; Handy, N. C. A New Hybrid Exchange-Correlation Functional Using the Coulomb-Attenuating Method (CAM-B3LYP). *Chem. Phys. Lett.* **2004**, *393* (1–3), 51–57. <https://doi.org/10.1016/j.cplett.2004.06.011>.
- (19) Tenderholt, A. L. No Title. *QMForge* Version 3.0.
- (20) Kieber-Emmons, M. T. No Title. *LUMO* Version 1.0.3.
- (21) Valentine, A. M.; Tavares, P.; Pereira, A. S.; Davydov, R.; Krebs, C.; Hoffman, B. M.; Edmondson, D. E.; Boi Hanh Huynh; Lippard, S. J. Generation of a Mixed-Valent Fe(III)Fe(IV) Form of Intermediate Q in the Reaction Cycle of Soluble Methane Monooxygenase, an Analog of Intermediate X in Ribonucleotide Reductase R2 Assembly. *J. Am. Chem. Soc.* **1998**, *120* (9), 2190–2191. <https://doi.org/10.1021/ja974169x>.
- (22) Tong, W.; Burdi, D.; Riggs-Gelasco, P.; Chen, S.; Edmondson, D.; Huynh, B. H.; Stubbe, J.; Han, S.; Arvai, A.; Tainer, J. Characterization of Y122F R2 of *Escherichia Coli* Ribonucleotide Reductase by Time-Resolved Physical Biochemical Methods and X-Ray Crystallography. *Biochemistry* **1998**, *37* (17), 5840–5848. <https://doi.org/10.1021/bi9728811>.
- (23) Ling, J.; Sahlin, M.; Sjöberg, B. M.; Loehr, T. M.; Sanders-Loehr, J. Dioxygen Is the Source of the μ -Oxo Bridge in Iron Ribonucleotide Reductase. *J. Biol. Chem.* **1994**, *269* (8), 5595–5601.
- (24) Brunold, T. C.; Solomon, E. I. Reversible Dioxygen Binding to Hemerythrin. 1. Electronic Structures of Deoxy- and Oxyhemerythrin. *J. Am. Chem. Soc.* **1999**, *121* (36), 8277–8287. <https://doi.org/10.1021/ja990334s>.
- (25) Martin, R. L. Natural Transition Orbitals. *J. Chem. Phys.* **2003**, *118* (11), 4775–4777. <https://doi.org/10.1063/1.1558471>.

- (26) Spaeth, A. D.; Gagnon, N. L.; Dhar, D.; Yee, G. M.; Tolman, W. B. Determination of the Cu(III)-OH Bond Distance by Resonance Raman Spectroscopy Using a Normalized Version of Badger's Rule. *J. Am. Chem. Soc.* **2017**, *139* (12), 4477–4485. <https://doi.org/10.1021/jacs.7b00210>.
- (27) Weitz, A. C.; Hill, E. A.; Oswald, V. F.; Bominaar, E. L.; Borovik, A. S.; Hendrich, M. P.; Guo, Y. Probing Hydrogen Bonding Interactions to Iron-Oxido/Hydroxido Units by ⁵⁷Fe Nuclear Resonance Vibrational Spectroscopy. *Angew. Chemie - Int. Ed.* **2018**, *57* (49), 16010–16014. <https://doi.org/10.1002/anie.201810227>.
- (28) Srinivas, V.; Banerjee, R.; Lebrette, H.; Jones, J. C.; Aurelius, O.; Kim, I. S.; Pham, C. C.; Gul, S.; Sutherlin, K. D.; Bhowmick, A.; John, J.; Bozkurt, E.; Fransson, T.; Aller, P.; Butryn, A.; Bogacz, I.; Simon, P.; Keable, S.; Britz, A.; Tono, K.; Kim, K. S.; Park, S. Y.; Lee, S. J.; Park, J.; Alonso-Mori, R.; Fuller, F. D.; Batyuk, A.; Brewster, A. S.; Bergmann, U.; Sauter, N. K.; Orville, A. M.; Yachandra, V. K.; Yano, J.; Lipscomb, J. D.; Kern, J.; Högbom, M. High-Resolution XFEL Structure of the Soluble Methane Monooxygenase Hydroxylase Complex with Its Regulatory Component at Ambient Temperature in Two Oxidation States. *J. Am. Chem. Soc.* **2020**, *142* (33), 14249–14266. <https://doi.org/10.1021/jacs.0c05613>.
- (29) Römelt, M.; Ye, S.; Neese, F. Calibration of Modern Density Functional Theory Methods for the Prediction Of ⁵⁷Fe Mössbauer Isomer Shifts: Meta-GGA and Double-Hybrid Functionals. *Inorg. Chem.* **2009**, *48* (3), 784–785. <https://doi.org/10.1021/ic801535v>.
- (30) Westre, T. E.; Kennepohl, P.; DeWitt, J. G.; Hedman, B.; Hodgson, K. O.; Solomon, E. I. A Multiplet Analysis of Fe K-Edge 1s → 3d Pre-Edge Features of Iron Complexes. *J. Am. Chem. Soc.* **1997**, *119* (27), 6297–6314. <https://doi.org/10.1021/ja964352a>.
- (31) Dey, A.; Hocking, R. K.; Larsen, P.; Borovik, A. S.; Hodgson, K. O.; Hedman, B.; Solomon, E. I. X-Ray Absorption Spectroscopy and Density Functional Theory Studies of [(H₃buea)Fe^{III}-X]ⁿ⁻ (X = S²⁻, O²⁻, OH⁻): Comparison of Bonding and Hydrogen Bonding in Oxo and Sulfido Complexes. *J. Am. Chem. Soc.* **2006**, *128* (30), 9825–9833. <https://doi.org/10.1021/ja061618x>.
- (32) Lancaster, K. M.; Finkelstein, K. D.; Debeer, S. K β X-Ray Emission Spectroscopy Offers Unique Chemical Bonding Insights: Revisiting the Electronic Structure of Ferrocene. *Inorg. Chem.* **2011**, *50* (14), 6767–6774. <https://doi.org/10.1021/ic200822b>.
- (33) Poater, A.; Ragone, F.; Correa, A.; Cavallo, L. Comparison of Different Ruthenium-Alkylidene Bonds in the Activation Step with N-Heterocyclic Carbene Ru-Catalysts for Olefins Metathesis. *Dalt. Trans.* **2011**, *40* (42), 11066–11069. <https://doi.org/10.1039/c1dt10959f>.
- (34) England, J.; Farquhar, E. R.; Guo, Y.; Cranswick, M. A.; Ray, K.; Münck, E.; Que, L. Characterization of a Tricationic Trigonal Bipyramidal Iron(IV) Cyanide Complex, with a Very High Reduction Potential, and Its Iron(II) and Iron(III) Congeners. *Inorg. Chem.* **2011**, *50* (7), 2885–2896. <https://doi.org/10.1021/ic102094d>.
- (35) Shu, L.; Nesheim, J. C.; Kauffmann, K.; Münck, E.; Lipscomb, J. D.; Que, L. An Fe₂^{IV}O₂

Materials and Methods

Sample preparation

The ^{57}Fe labeled sMMO proteins MMOH and MMOB were purified as previously reported.^{1,2} The rapid-freeze quench (RFQ) powder samples of intermediate Q were prepared according to protocols previously described.³ In order to prepare intermediate MMOH samples at high concentration (0.9 mM active sites after mixing), the chlorite dismutase and sodium chlorite reaction was utilized to generate *in-situ* oxygen ($[\text{O}_2] = 5 \text{ mM}$) for the sMMO reaction.⁴ Anaerobic chlorite dismutase was added to the reduced anaerobic MMOH:MMOB protein solution to a working concentration of 20 μM before loading the protein solution into the RFQ syringe. Sodium chlorite was added to the oxygen-saturated buffer solution to a working concentration of 5 mM; this solution was then loaded into the RFQ and mixed with the protein solution. The vigorous evolution of O_2 in this manner alleviated the problem of low Q yields arising from an inefficient mixing of viscous sMMO protein samples with oxygen saturated buffer. In order to prepare intermediate $^{18}\text{O}_2$ -labeled Q samples, $^{18}\text{O}_2$ -saturated buffer was used and the MMOH protein concentration reduced to 0.5 mM.

The RFQ powder samples of intermediate Q were packed into 10 x 10 x 6 mm Delrin circular NRVS cells sealed with Kapton tape. All the packing materials were kept at liquid nitrogen temperatures to avoid intermediate decay. Samples were packed atop a block of solid copper partially submerged in a liquid nitrogen bath. The Delrin cap of the circular cell was sealed onto the cell by applying the tip of a soldering iron.

Rectangular 11 x 4 x 1.2 mm NRVS cells containing a frozen liquid solution of intermediate Q were prepared by injecting 50 μl of the sMMO reaction directly into the pre-chilled cell from the RFQ instrument through a needle, and subsequently immersed in liquid nitrogen after 2 seconds.

Spectroscopy

The ^{57}Fe Mössbauer spectra were collected using a See Co. W302 resonant gamma ray spectrometer with a 1.85-GBq ^{57}Co source (Rh matrix, Be window). All spectra were collected at 6 K, either with a 73 mT applied parallel magnetic field or no magnetic field. Samples were kept in a SVT-400 cryostat from Janis using liquid helium as a cryogen for all measurements. Isomer shifts are given relative to a metallic foil of $\alpha\text{-Fe}$ at room temperature. Mössbauer spectra were analyzed using WMoss (www.wmoss.org) and the Vinda software package for Microsoft Excel⁵, and integrated intensities were normalized using the Wave Stats function of Igor Pro.

Cryoreduced RFQ samples of Q were kept under liquid nitrogen and exposed to γ -irradiation from a ^{60}Co source with a dose rate of 20 kGy/h for 2 to 4 hours at Advanced Radiation Technology Institute (ARTI) of Korea Atomic Energy Research Institute (KAERI). NRVS data for $^{16}\text{O}_2$ RFQ samples of intermediate Q were collected at BL09XU at SPring-8 (C-mode bunch), and NRVS data for $^{18}\text{O}_2$ frozen solution samples were collected at BL19LXU at

SPRING-8. All samples were maintained at 60-70 K (measured using the relative phonon creation/phonon annihilation intensities) on a copper block glued to a liquid helium cryostat. To prevent sample heating by the beam, the NRVS samples were illuminated upon cooling of the cryostat to ~ 10 K. A $[\text{NEt}_4][\text{FeCl}_4]$ standard⁶ was measured at the beginning and middle of each experiment to calibrate the NRVS energy scale, and to correct for energy drifts during the course of the experiment. The PHOENIX software package⁷ using the spectra.tools web application⁸ was used to sum multiple scans, subtract the elastic peak, and convert the raw data into the partial-vibrational density of states (PVDOS) spectra. The integrated areas of all NRVS spectra were normalized to 3 using the Wave Stats function of Igor Pro.

DFT calculations

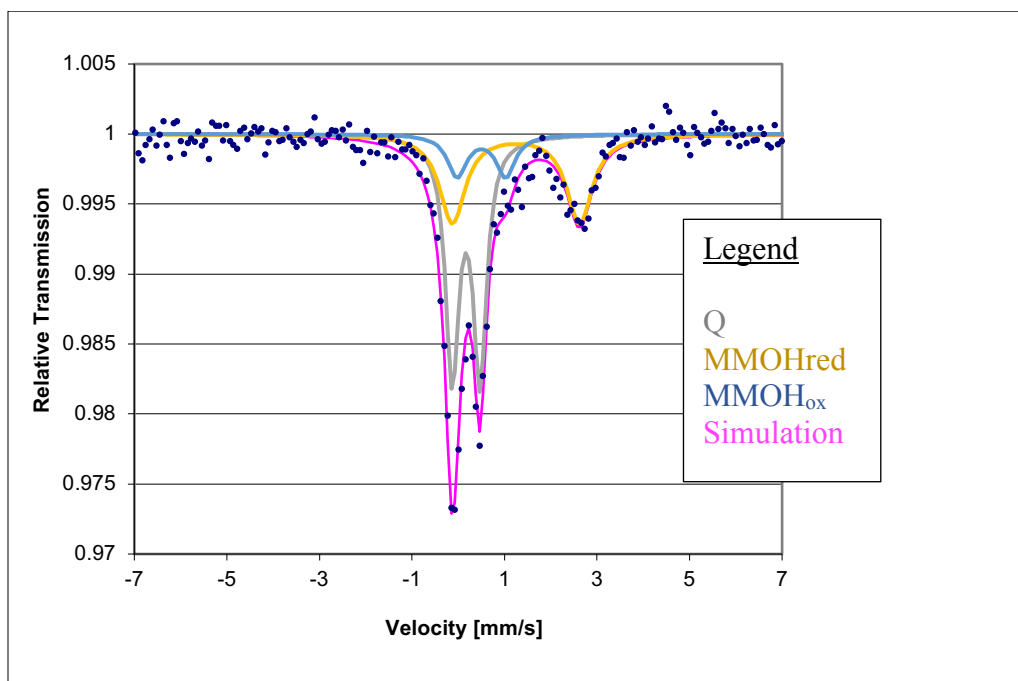
DFT models for intermediate Q were initially constructed from a MMOB-associated MMOH model derived from crystallography.⁹ In this model, all first-sphere residues were included (E243, E144, E114, E209, H246, H147) and their C_α carbon atoms were truncated to methyl groups. Artificial hydrogen atoms introduced by this C_α truncation scheme were frozen during geometry optimizations to model the constraints of the protein backbone. Second- and third-sphere residues involved in hydrogen-bonding interactions with the histidine ligands were additionally included (D242, D143, R146, R245, Y67) and truncated to include only the amino acid functional groups. DFT optimizations for all intermediate Q models were completed using the Gaussian 09 and 16 software packages.^{10,11} The Becke-Perdew86 (BP86) functional¹² was used with 10% HF included using the 6-31g(d) basis set, in accord with previous NRVS studies of high-valent¹³ and peroxo¹⁴ model complexes. The protein cavity of the sMMOH active site was modeled using the polarizable continuum model¹⁵ (PCM) using a dielectric constant of $\epsilon = 15$. For models further considered in cryoreduction calculations, the BP86/10% HF optimized models were initially reoptimized using B3LYP¹⁶ (20% HF) to limit the low HF preference for low- and intermediate spin electronic structures in the Fe(III)Fe(IV) and Fe(III)₂ states. Cryoreduced models with Fe₁(III)Fe₂(IV) and Fe₂(III)Fe₁(IV) electronic structures were optimized by including an additional α spin on Fe₁ or Fe₂ (respectively) of the Fe(IV)₂ Q models, and allowing the structures to reoptimize. Often, Fe₁(III)Fe₂(IV) and Fe₂(III)Fe₁(IV) models were both obtained, and both were considered for cryoreduction modeling unless a large (> 2 kcal mol⁻¹) energy difference in the structures was observed, in which case the higher energy structure was disregarded. Fe(III)₂ models were obtained by introducing an β electron on the remaining Fe(IV) in the mixed-valent model(s) above and reoptimizing. Calculated NRVS spectra were generated from the frequency calculations using the gennrvs script. The mass of hydrogen atoms mimicking the protein backbone were increased to 100 amu to prevent their artificial mixing¹⁷ of vibrations with the active site.

For time dependent DFT (TD-DFT) calculations, the second- and third-sphere residues were removed, and first-sphere residues were truncated to one carbon before the amino acid functional group. For the calculation of linear coupling terms, these TD-DFT models were distorted along the normal modes of interest (see main text). To avoid low energy CT from anionic ligands the TD-DFT spectra and natural transition orbitals (NTO) were calculated using Gaussian 09 with the CAM-B3LYP functional¹⁸ and 6-31g(d) basis set. Molecular orbital compositions from DFT single-point calculations were calculated with QMForge,¹⁹ and the molecular orbital contours were modeled with LUMO.²⁰

TD-DFT calculations at the Fe K-edge were carried out using the ORCA quantum chemistry program, version 4.0.1.2. The CAM-B3LYP functional was used for all calculations, and the polarized triple-zeta basis set def2-TZVPP and auxiliary basis set def2/J were used for all atoms except iron, for which the CP(PPP) basis set was used. A very dense integration grid (grid6), and tight convergence criteria were enforced. Calculated K pre-edge spectra were visualized using the ORCA_MAPSPC module with a Gaussian broadening of 1.0 eV, using the origin independent method (ABSIO)

All reaction coordinate calculations were completed with the B3LYP functional using the 6-31g(d) basis set.

Figure S1 Mössbauer spectrum of high-purity RFQ-Q powder measured in NRVS collected at 6 K. The MMOH_{red} species was fit as a broad doublet for simplicity. Sample measured in a cylindrical 10 x 10 x 6 mm cup.



Fitting parameters for species in Figure S1

Species	δ (mm/s)	ΔE_Q (mm/s)	Area %
Q	0.17	0.60	51
MMOH _{red}	1.25	2.75	37
MMOH _{ox}	0.50	1.05	12

Figure S2 NRVS spectra of one high purity (50% Q, 37% MMOH_{red}, 13% MMOH_{ox}) Q sample over 10-hour intervals. Arrow pointing down indicates decay of Q feature, while arrow pointing up indicates growth of decay features.

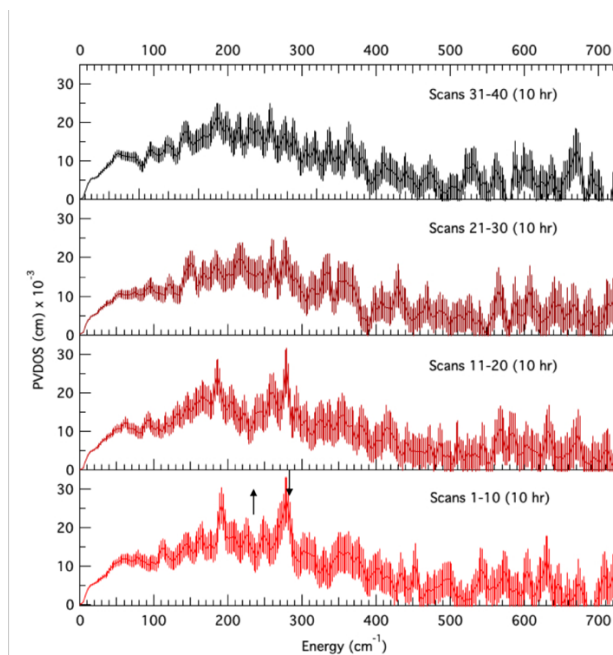


Figure S3 NRVS data from seven samples (60 scans per spectrum) combined and binned into five-hour (1 hr/scan) intervals. Major changes over time highlighted with arrows.

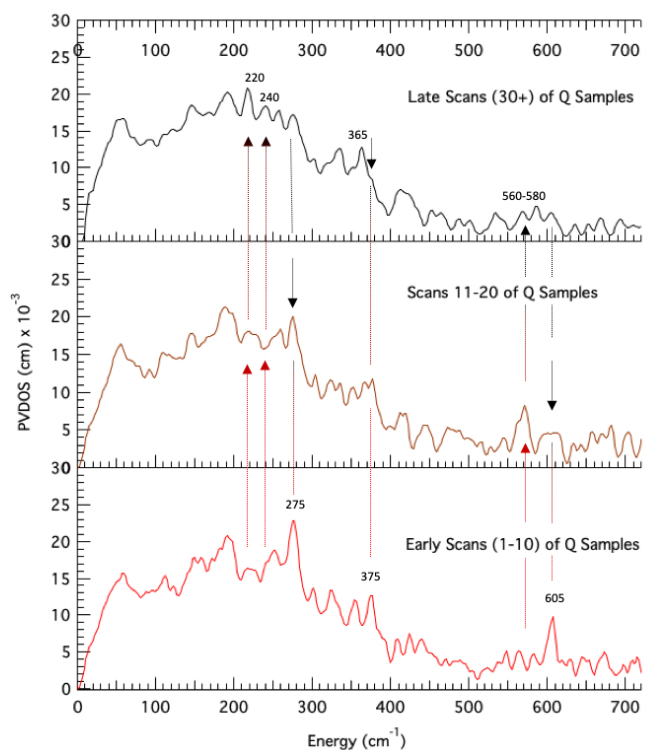


Figure S4 NRVS data from seven samples combined and binned into five-hour (1 hr/scan) intervals. Major changes over time highlighted with arrows.

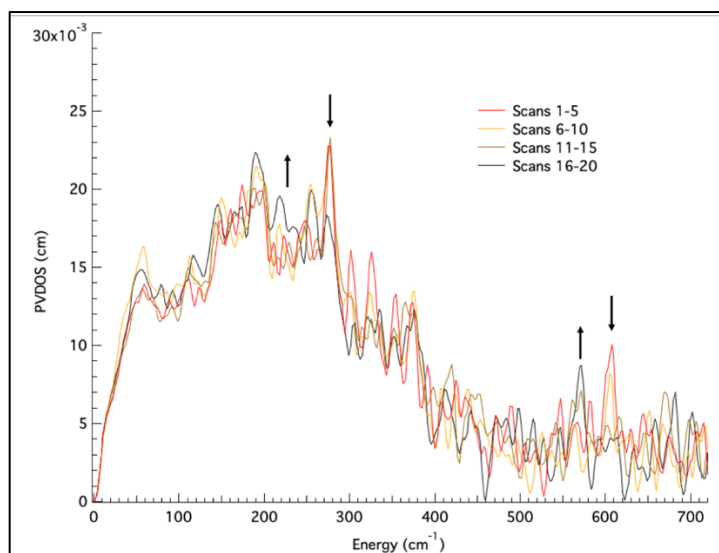


Figure S5 Raw data for the $^{16}\text{O}_2$ and $^{18}\text{O}_2$ Q decay spectra depicted in Figure 1B. (A) The $^{18}\text{O}_2$ decay data has been scaled by 1.1 to normalize its elastic peak relative to the $^{16}\text{O}_2$ decay data (not shown), and a background has been subtracted from both raw spectra. (B) The $^{18}\text{O}_2$ decay data is upshifted on the y-axis for differentiation from $^{16}\text{O}_2$ data.

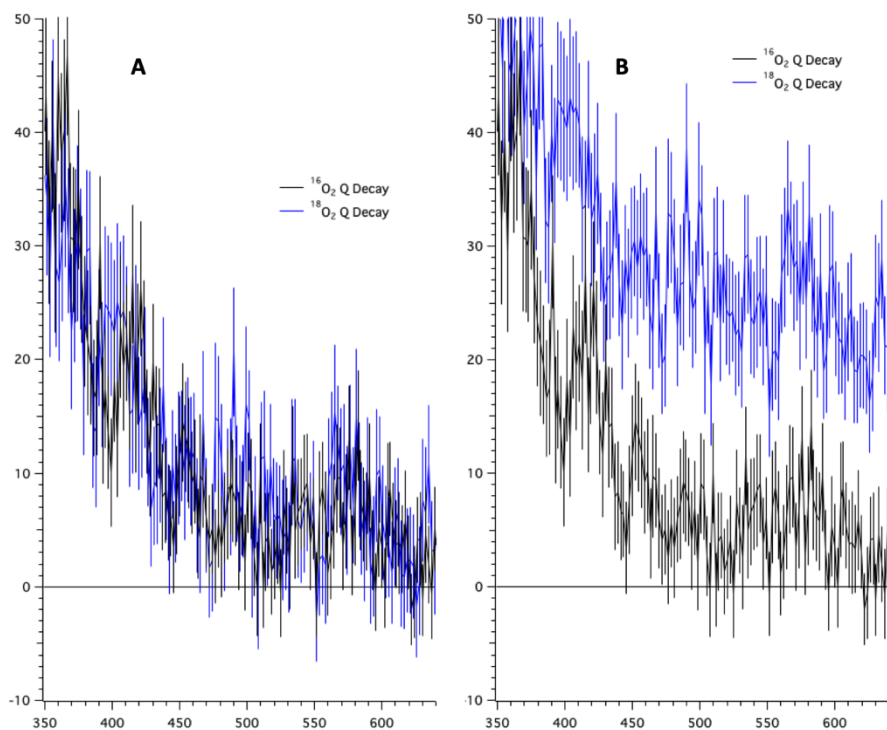
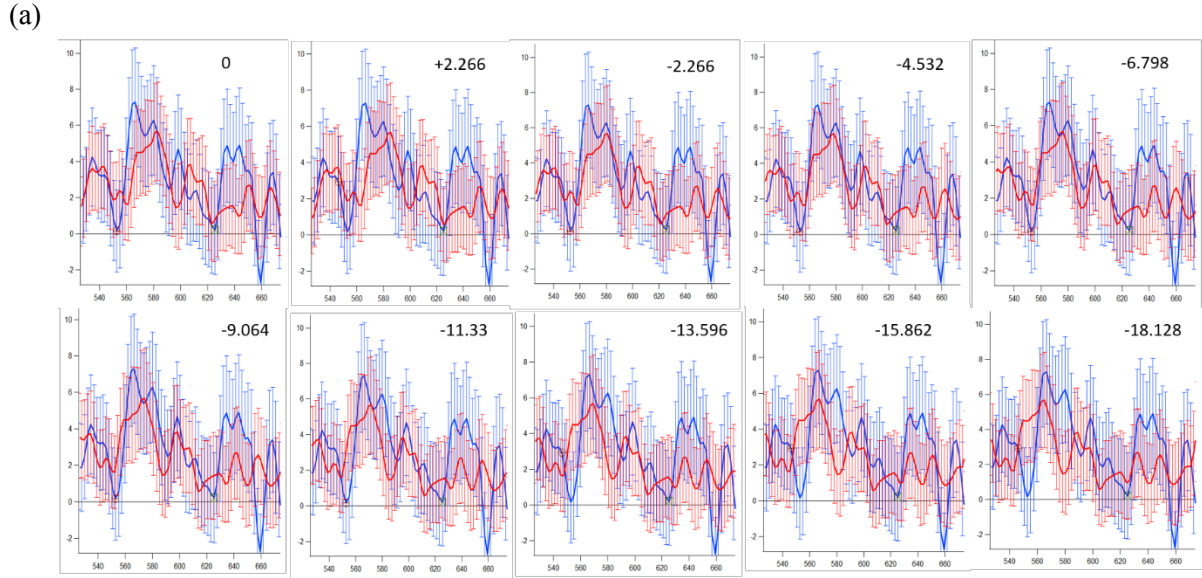


Figure S6. Estimation of isotope shifts in Q decay NRVS spectra obtained with $^{16}\text{O}_2$ (red) and $^{18}\text{O}_2$ (blue). Because of the noise in the intensity, the isotope shifts were assessed by shifting the energy of the ^{16}O spectrum lower stepwise until the sum of the squared differences between the ^{16}O and ^{18}O spectra (s) reached the minimum. Spectral overlays with energy shifts in cm^{-1} and the s values obtained for the energy ranges of 545-624 cm^{-1} and 387-444 cm^{-1} are given in (a & b) and (c & d), respectively. This error analysis shows that the 580 and 420 cm^{-1} features are associated with isotope shifts of 4 to 7 cm^{-1} and 12 to 15 cm^{-1} , respectively. Outside of this range the difference between spectra is outside the error (Δs) in the data.



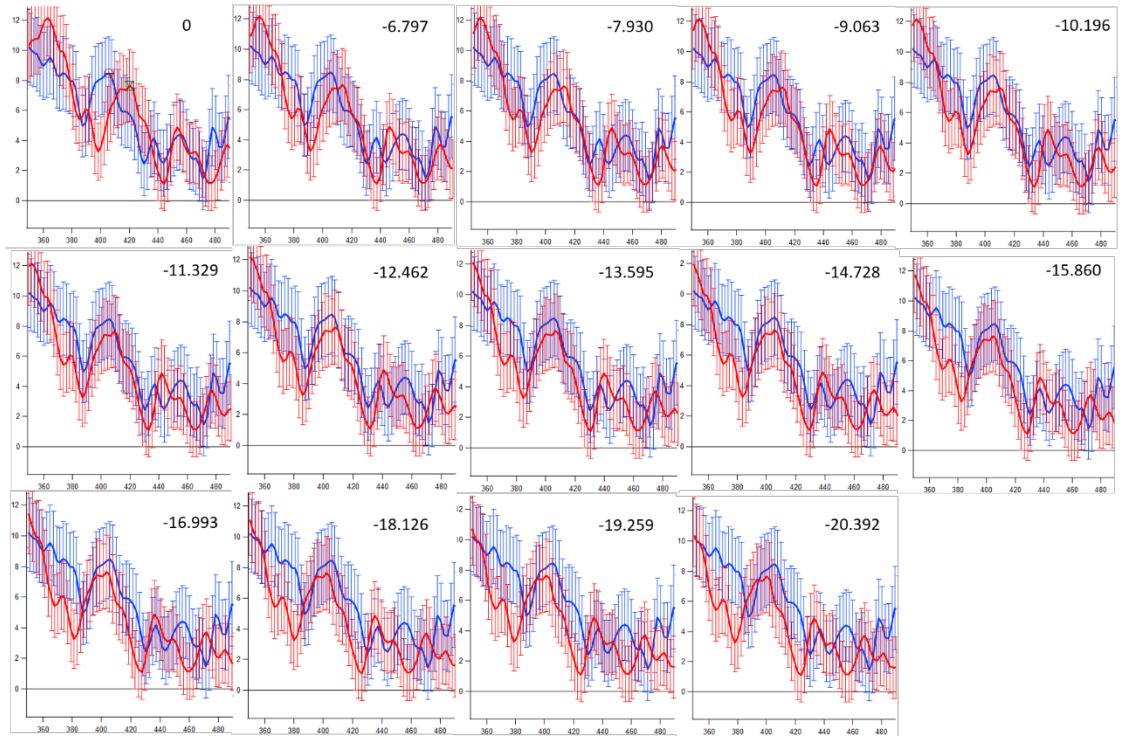
(b)

$$s = \sum (y_{16} - y_{18})^2$$

$$\Delta s = \sqrt{\sum 4(y_{16} - y_{18})^2((\Delta y_{16})^2 + (\Delta y_{18})^2)}$$

Shift of x_{16}	$(s \pm \Delta s)/(10^{-4})$
+2.266	1.4 ± 0.8
0.000	1.0 ± 0.7
-2.266	0.7 ± 0.6
-4.532	0.5 ± 0.5
-6.798	0.5 ± 0.5
-9.064	0.7 ± 0.6
-11.33	1.0 ± 0.7
-13.596	1.3 ± 0.8
-15.862	1.5 ± 0.9
-18.128	1.8 ± 0.9

(c)



(d)

Shift of x_{16}	$(s \pm \Delta s)/(10^{-4})$
0.000	2.6 ± 1.0
-6.797	1.4 ± 0.7
-7.930	1.2 ± 0.7
-9.063	1.1 ± 0.6
-10.196	0.9 ± 0.6
-11.329	0.8 ± 0.5
-12.462	0.7 ± 0.5
-13.595	0.7 ± 0.5
-14.728	0.7 ± 0.5
-15.860	0.9 ± 0.6
-16.993	1.1 ± 0.6
-18.126	1.4 ± 0.7
-19.259	1.7 ± 0.8
-20.392	2.0 ± 0.9

Figure S7 NRVS data of BL19 (red) and 30+ hour time point data of BL09 (black) Q samples. 14 and 60 scans were compiled for BL19 and BL09 late scan data (respectively) to achieve similar S/N.

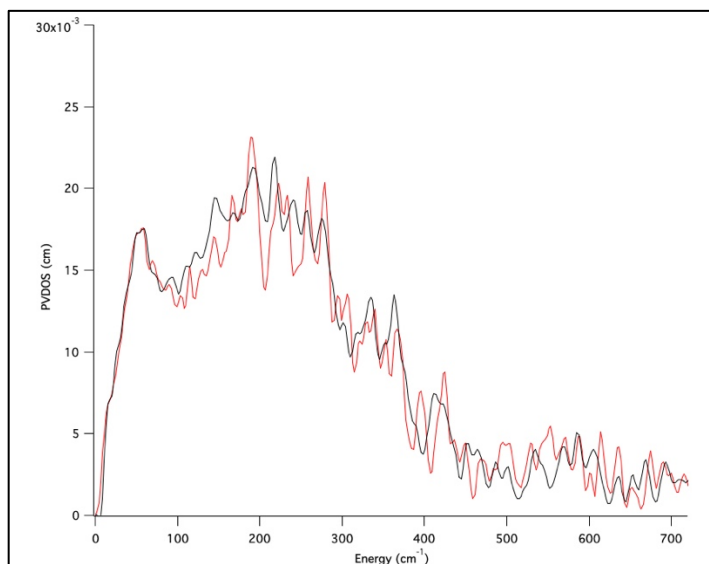


Figure S8 Mössbauer spectrum of 11 x 4 x 1.2 mm BL19 sample before NRVS measurement (bottom, red spectrum equivalent to Figure 2A red spectrum). Fit includes 50% Q (gray), 15% MMOH_{ox} (green), and 35% MMOH_{red} (yellow) scaled accordingly and shown at the top.

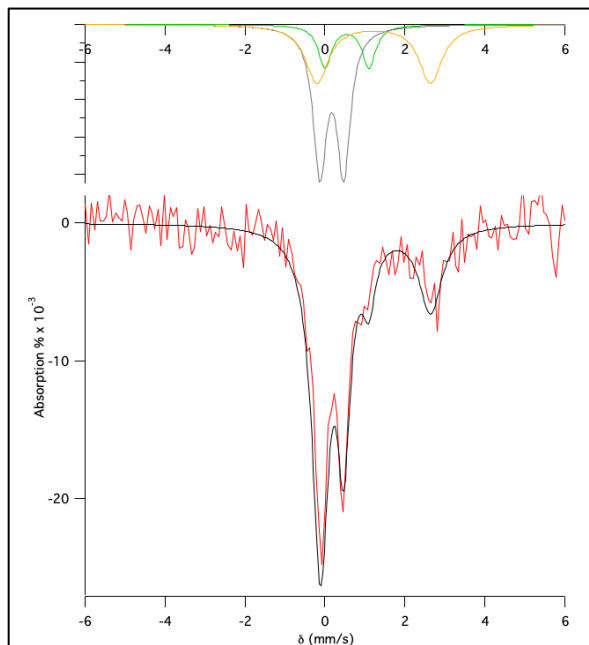


Figure S9 Mössbauer fitting of the cryoreduced Fe(III)₂ species (Q3). The 73 mT parallel magnetic field, 6 Mrad irradiated Q sample Mössbauer spectrum (middle, black, equivalent to the spectrum in Figure 2B bottom) was first fit with Qx (17%) and Q (8%) to their unique features present at $\delta = -3.7$ and 0.5 mm/s, respectively. The spectra for Qx and Q scaled by 17% and 8% are shown in red and black (respectively) in the top plot. The Mössbauer spectrum of the MMOH_{red} species was obtained by measuring MMOH_{red} in a 73 mT parallel field at 6 K, and smoothing the resulting spectrum. MMOH_{red} (50% total iron) was fit assuming the initial oxidized Fe(III)₂ species was cryoreduced to Fe(II)₂ (as observed in the cryoreduction of Q from *Methylococcus capsulata* MMOH²¹); its 50% scaled plot is shown at the top (blue). This combined MMOH_{red}, Qx, and Q 75% spectrum is shown in the middle plot (red), and was subtracted from the experimental 73 mT data to obtain the spectrum for Q3 (bottom, black). It is best fit (bottom, red) as one species with two inequivalent Fe(III) sites, with $\delta_1 = 0.50$, mm/s, $\Delta E_{Q1} = 1.99$ mm/s; and $\delta_2 = 0.63$, mm/s, $\Delta E_{Q2} = 1.33$ mm/s. Thus, its parameters indicate a single biferric species. The lack of field dependence of its signal (compare Figure 2B middle and bottom spectra at 1.45 mm/s) indicates antiferromagnetic coupling in the Fe(III)₂ site.

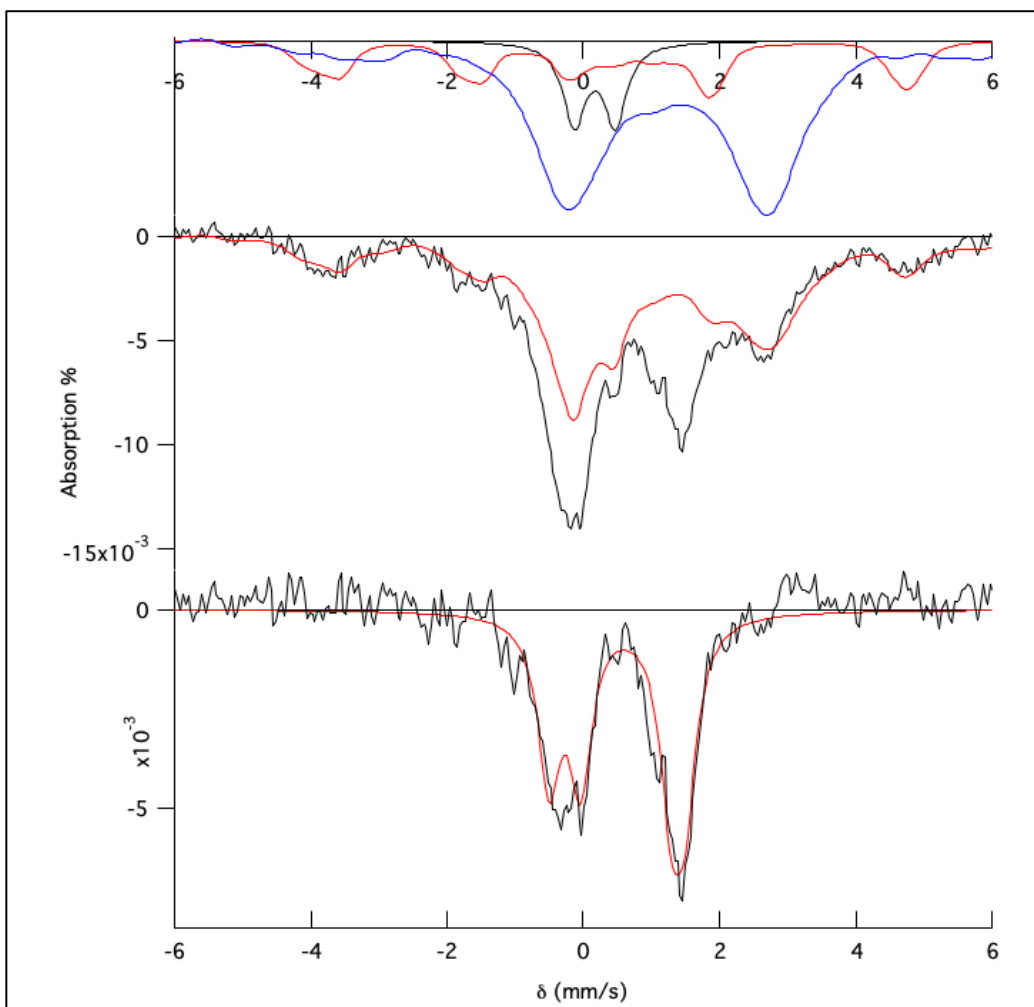


Figure S10 Simulations of Mössbauer spectra of BL19 Q samples pre- and post-NRVS measurements (see Figure 2A for comparison). Pre-NRVS measurement simulation contains 50% Q, 15% MMOH_{ox}, and 35% MMOH_{red} (red). The post-NRVS simulation was constructed by combining 80% of the pre-NRVS simulation with 20% of the decay simulation. This decay simulation includes 0% Q, 20% Q_x, and 30% Q₃, and 50% MMOH_{red}.

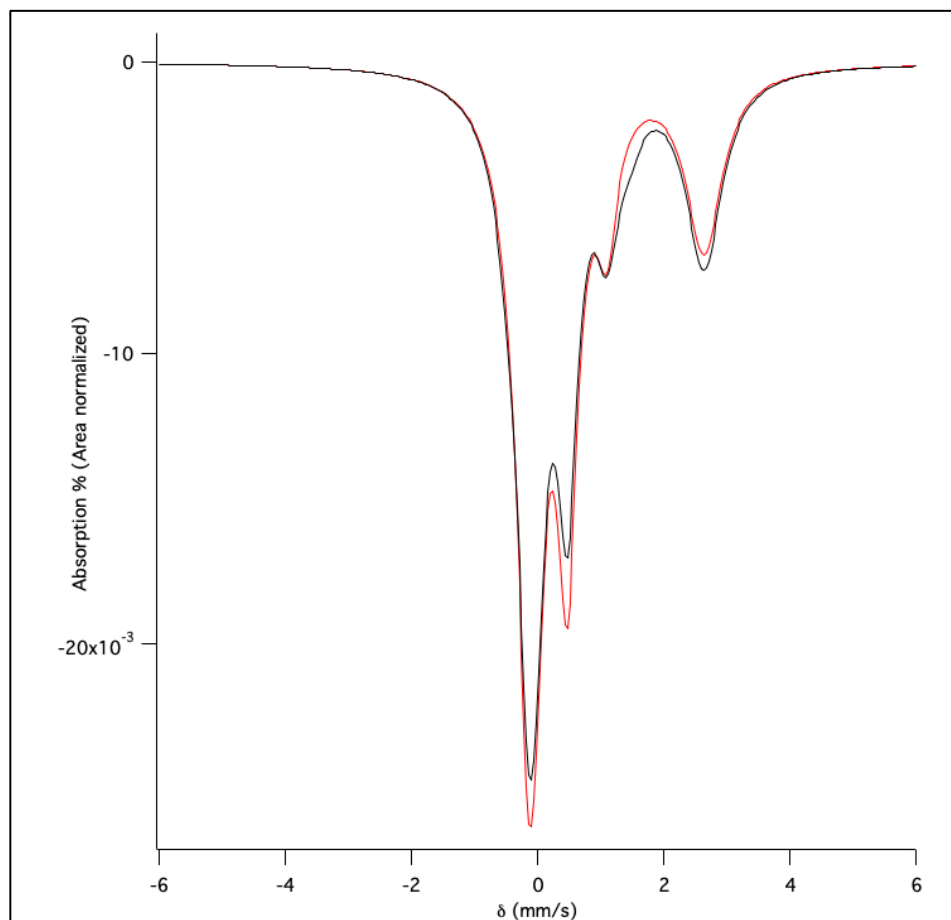
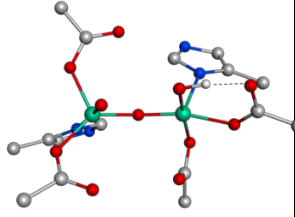
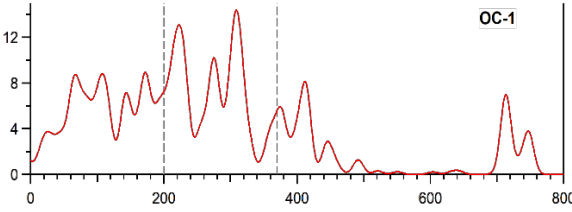
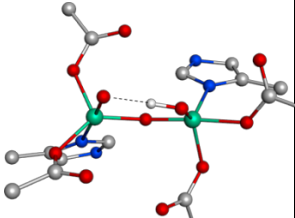
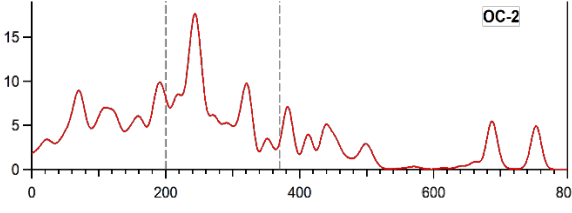
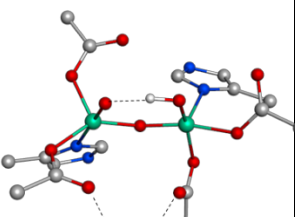
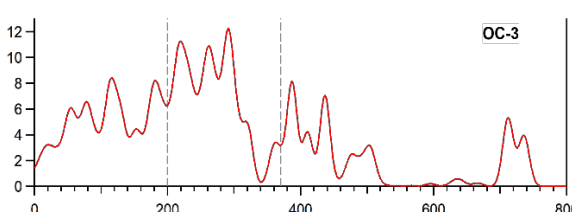
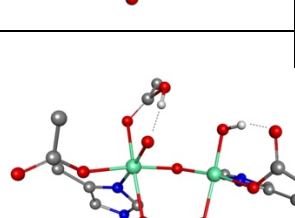
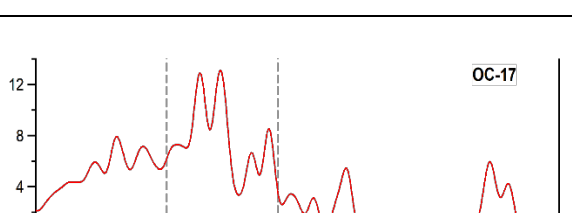
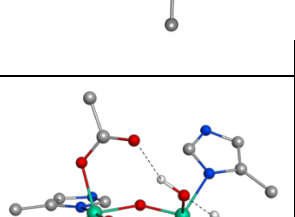
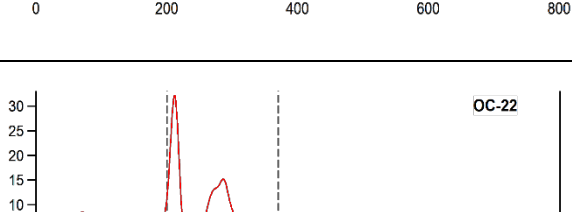
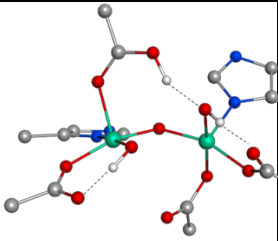
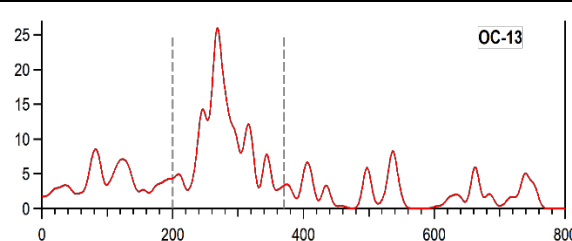
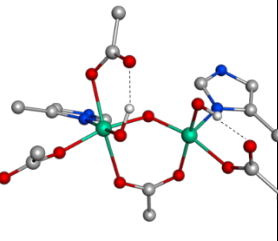
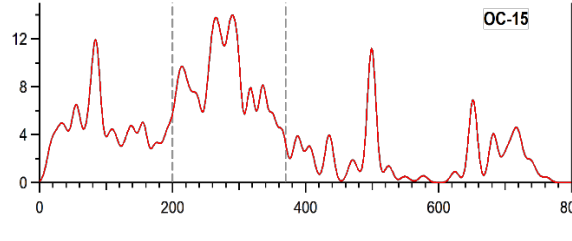
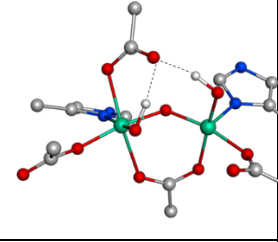
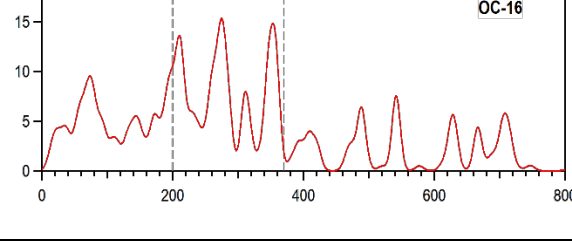
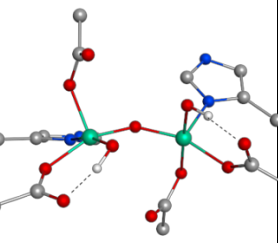
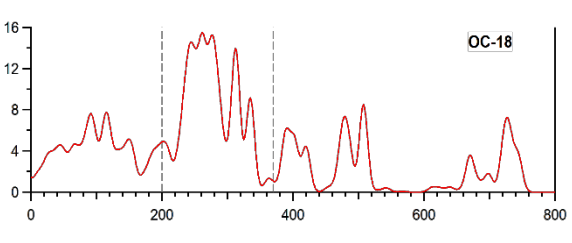
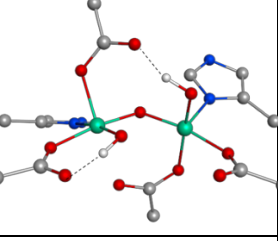
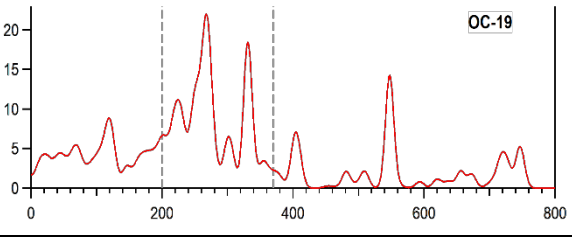
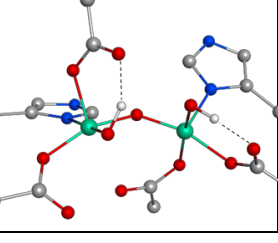
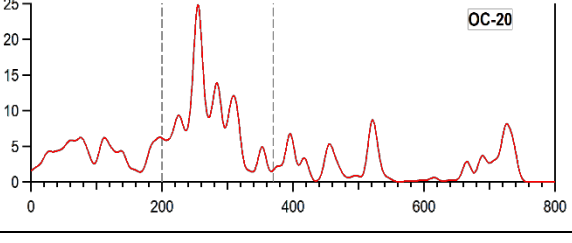
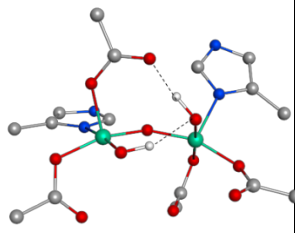
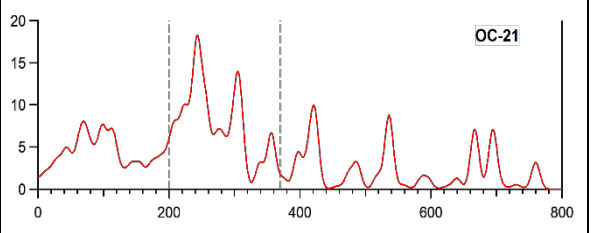
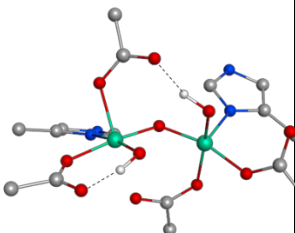
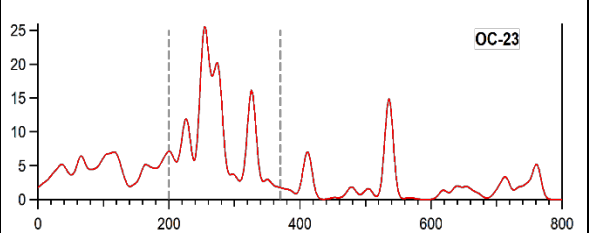
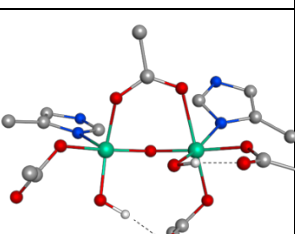
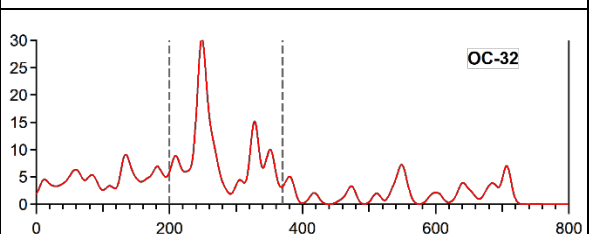
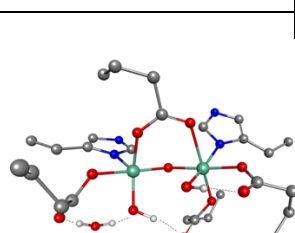
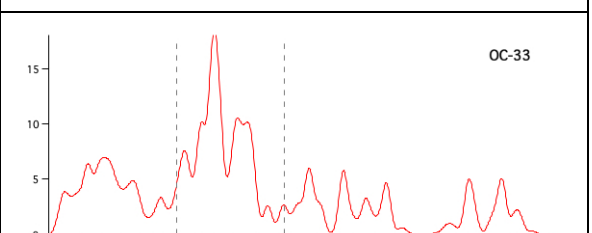
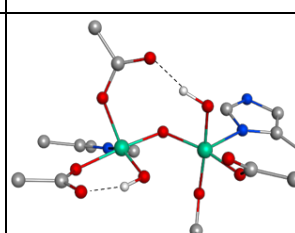
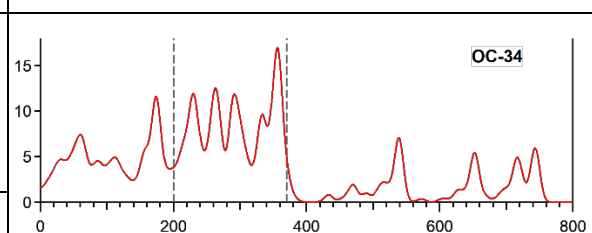
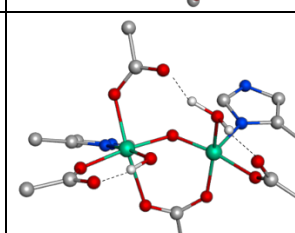
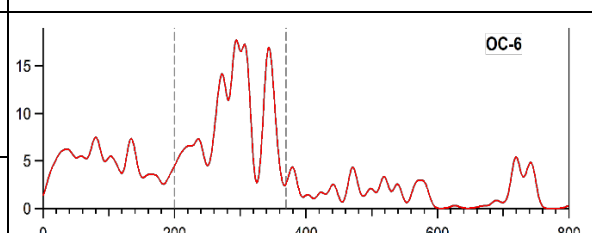


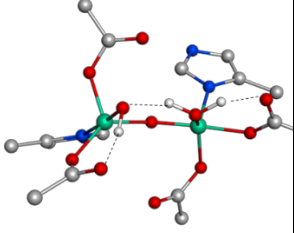
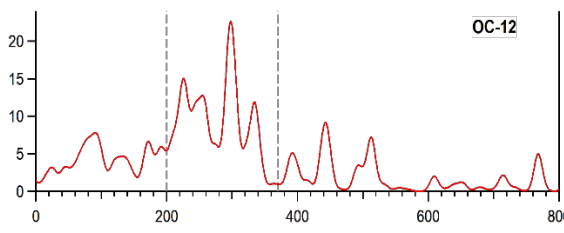
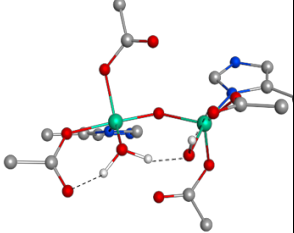
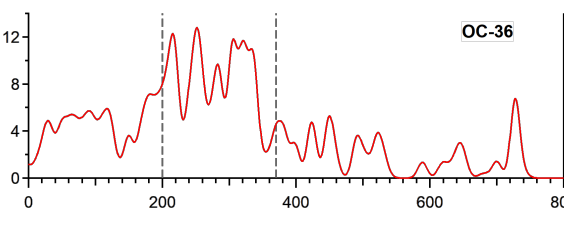
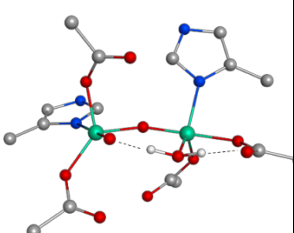
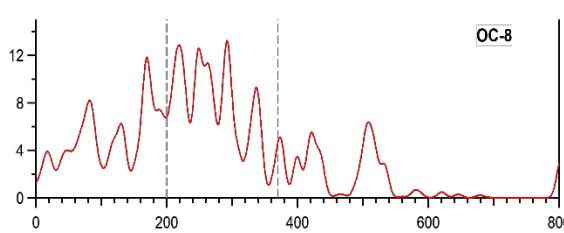
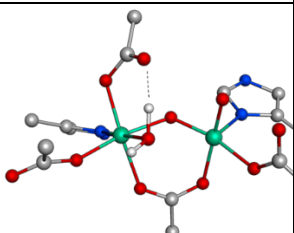
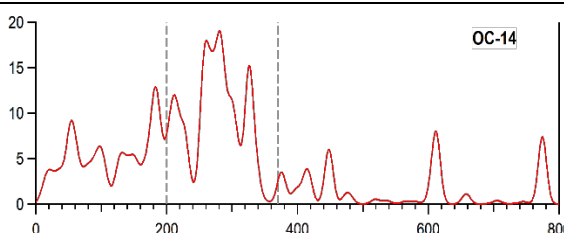
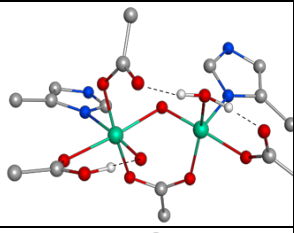
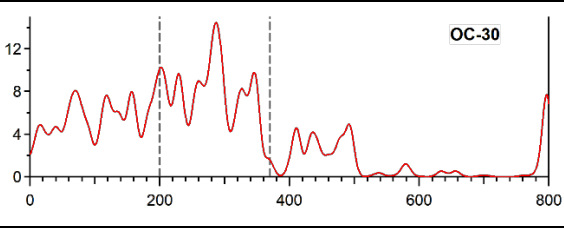
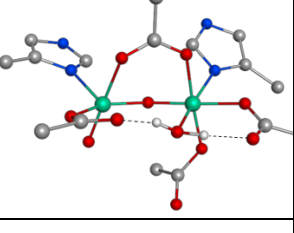
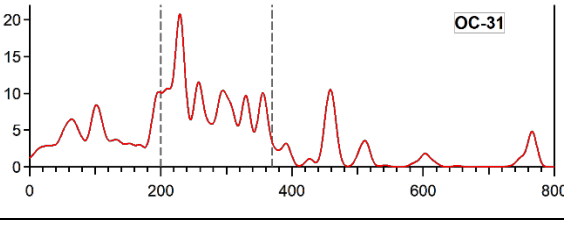
Table S1 DFT optimized structures for all 90 Q models considered in this study, as well as their simulated NRVs spectra calculated in BP86 + 10% HF using the 6-31g(d) basis set. The closest vibration to 690 cm^{-1} is provided, as well as its $^{18}\text{O}_2$, $^{16}\text{O}_2$, and ^2H isotope shifts. Fe-Fe distance for each model included as well.

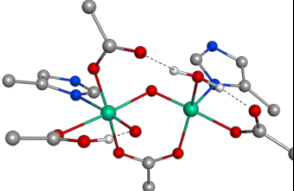
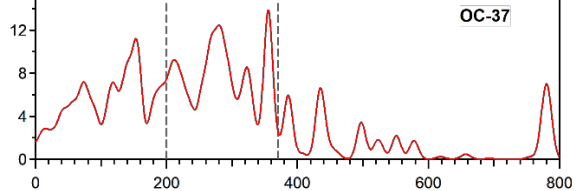
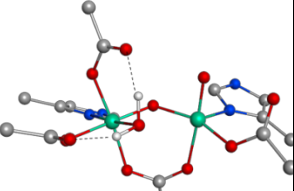
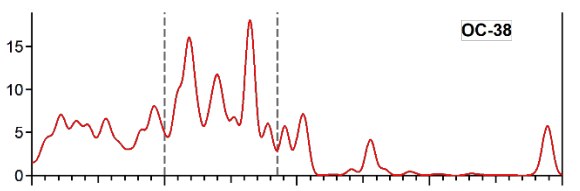
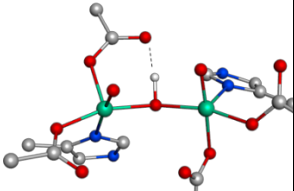
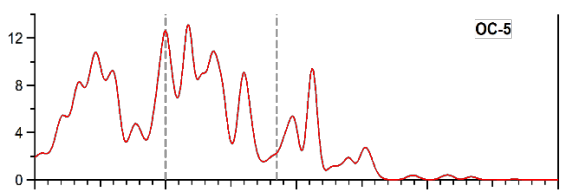
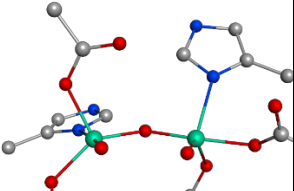
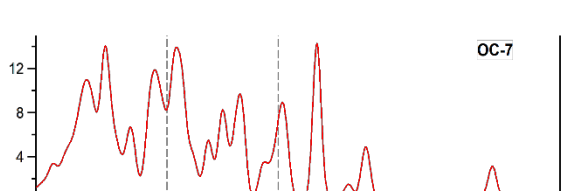
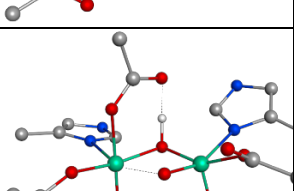
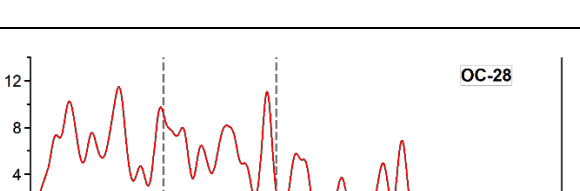
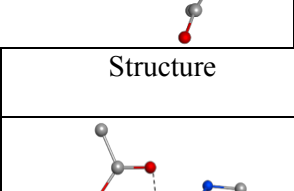
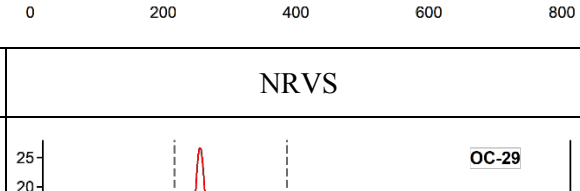
Model Name	Structure	rR/ cm^{-1} ; information relevant to XAS	NRVS
OC1 -OH/=O		$\nu(\text{Fe-OH}) + \nu_{\text{as}}(\text{Fe-O-Fe}) = 747.9$ $\Delta(^{18}\text{O}_2) = -33.3$ $\Delta(^{16}\text{O}^{18}\text{O}) = -24.7$ $\Delta(\text{D}) = -8.1$ <hr/> $r(\text{Fe}\dots\text{Fe}) = 3.39 \text{ \AA}$	
OC2 -OH/=O		$\nu(\text{Fe-OH}) = 686.4$ $\Delta(^{18}\text{O}_2) = -34.4$ $\Delta(^{16}\text{O}^{18}\text{O}) = -33.9$ $\Delta(\text{D}) = -8.2$ <hr/> $r(\text{Fe}\dots\text{Fe}) = 3.37 \text{ \AA}$	
OC3 -OH/=O		$\nu(\text{Fe-OH}) + \nu_{\text{as}}(\text{Fe-O-Fe}) = 727.6$ $\Delta(^{18}\text{O}_2) = -22.3$ $\Delta(^{16}\text{O}^{18}\text{O}) = -5.8$ $\Delta(\text{D}) = +8$ <hr/> $r(\text{Fe}\dots\text{Fe}) = 3.37 \text{ \AA}$	
OC17 -OH/=O		$\nu(\text{Fe-OH}) + \nu_{\text{as}}(\text{Fe-O-Fe}) = 722.4$ $\Delta(^{18}\text{O}_2) = -35.8$ $\Delta(^{16}\text{O}^{18}\text{O}) = -26.5$ $\Delta(\text{D}) = +0.8$ <hr/> $r(\text{Fe}\dots\text{Fe}) = 3.12 \text{ \AA}$	
OC22 -OH/=O		$\nu(\text{Fe-OH}) = 684.4$ $\Delta(^{18}\text{O}_2) = -30.8$ $\Delta(^{16}\text{O}^{18}\text{O}) = -30.7$ $\Delta(\text{D}) = -17.9$ <hr/> $r(\text{Fe}\dots\text{Fe}) = 3.33 \text{ \AA}$	
OC24 -OH/=O		$\nu_{\text{as}}(\text{Fe-O-Fe}) = 740.8$ $\Delta(^{18}\text{O}_2) = -30.2$ $\Delta(^{16}\text{O}^{18}\text{O}) = -29.5$ $\Delta(\text{D}) = -0.5$	

		$r(\text{Fe}\dots\text{Fe}) = 3.07$	
OC25 -OH/=O		$\nu(\text{Fe-OH}) = 692.3$ $\Delta(^{18}\text{O}_2) = -25.8$ $\Delta(^{16}\text{O}^{18}\text{O}) = -25.7$ $\Delta(\text{D}) = -12.7$ $r(\text{Fe}\dots\text{Fe}) = 3.16 \text{ \AA}$	
Model Name	Structure	r/cm^{-1} ; information relevant to XAS	NRVS
OC26 -OH/=O		$\nu(\text{Fe-OH}) + \nu_{\text{as}}(\text{Fe-O-Fe}) = 708.6$ $\Delta(^{18}\text{O}_2) = -44.8$ $\Delta(^{16}\text{O}^{18}\text{O}) = -24.5$ $\Delta(\text{D}) = -1.9$ $r(\text{Fe}\dots\text{Fe}) = 3.35 \text{ \AA}$	
OC9 -OH/-OH		$\nu(\text{Fe-OH}) + \nu(\text{Fe-OH}) = 719.3$ $\Delta(^{18}\text{O}_2) = -34.2$ $\Delta(^{16}\text{O}^{18}\text{O}) = -17.6$ $\Delta(\text{D}) = -21.0$ $r(\text{Fe}\dots\text{Fe}) = 3.36 \text{ \AA}$	
OC10 -OH/-OH		$\nu_{\text{as}}(\text{Fe-O-Fe}) + \nu(\text{Fe-OH}) = 730.4$ $\Delta(^{18}\text{O}_2) = -30.8$ $\Delta(^{16}\text{O}^{18}\text{O}) = -16.9$ $\Delta(\text{D}) = -2.0$ $r(\text{Fe}\dots\text{Fe}) = 3.29 \text{ \AA}$	
OC11 -OH/-OH		$\nu_{\text{as}}(\text{Fe-O-Fe}) + \nu(\text{Fe-OH}) = 699.3$ $\Delta(^{18}\text{O}_2) = -14.16$ $\Delta(^{16}\text{O}^{18}\text{O}) = -8.31$ $\Delta(\text{D}) = -5.4$ $r(\text{Fe}\dots\text{Fe}) = 3.37 \text{ \AA}$	

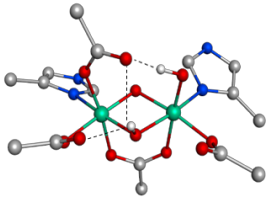
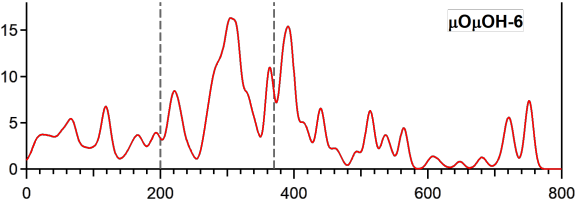
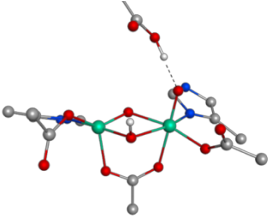
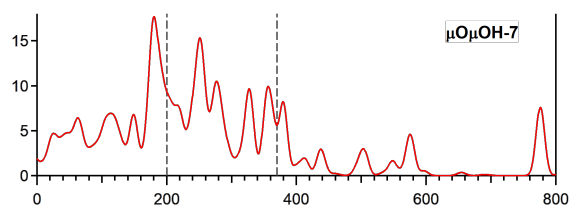
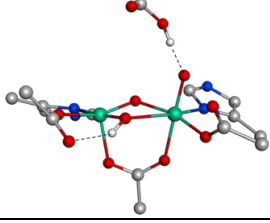
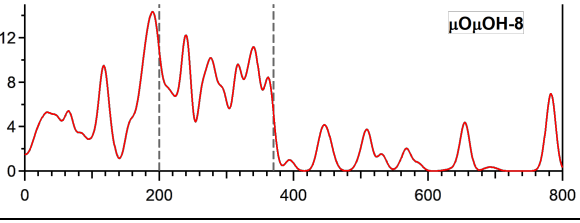
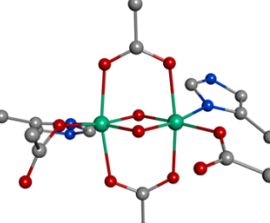
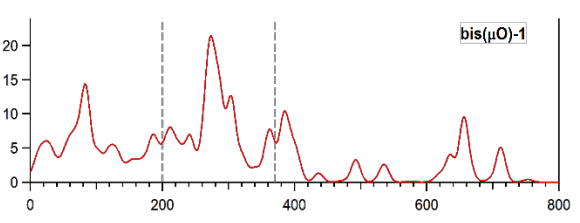
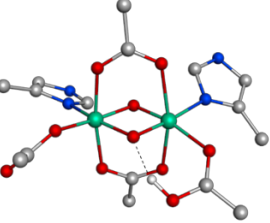
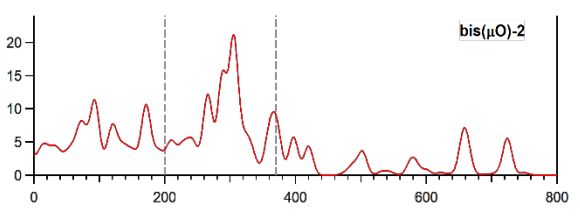
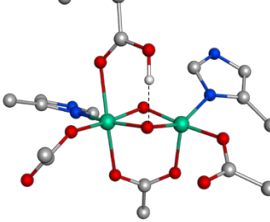
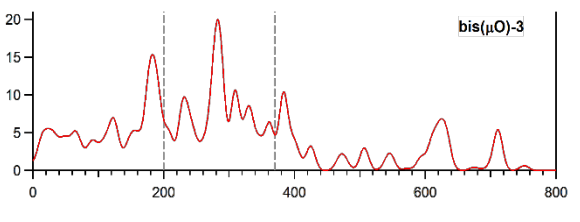
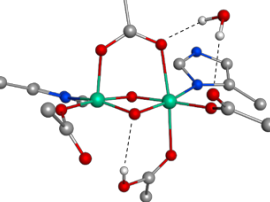
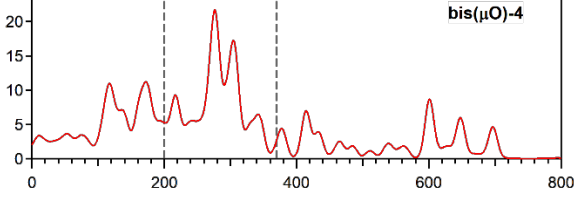
OC13 -OH/ OH		$v_{as}(\text{Fe-O-Fe})+v(\text{Fe-OH}) = 740.7$ $\Delta(^{18}\text{O}_2) = -35.0$ $\Delta(^{16}\text{O}^{18}\text{O}) = -18.7$ $\Delta(\text{D}) = -14.2$ $r(\text{Fe}\dots\text{Fe}) = 3.24 \text{ \AA}$	
OC15 -OH/ OH		$v_{as}(\text{Fe-O-Fe})+v(\text{Fe-OH}) = 715.1$ $\Delta(^{18}\text{O}_2) = -26.2$ $\Delta(^{16}\text{O}^{18}\text{O}) = -14.4$ $\Delta(\text{D}) = -3.8$ $r(\text{Fe}\dots\text{Fe}) = 3.17 \text{ \AA}$	
OC16 -OH/ OH		$v_{as}(\text{Fe-O-Fe})+v(\text{Fe-OH}) = 715.2$ $\Delta(^{18}\text{O}_2) = -37.9$ $\Delta(^{16}\text{O}^{18}\text{O}) = -27.1$ $\Delta(\text{D}) = +0.12$ $r(\text{Fe}\dots\text{Fe}) = 3.2 \text{ \AA}$	
Model Name	Structure	$r\text{R}/\text{cm}^{-1}$; information relevant to XAS	NRVS
OC18 -OH/-OH		$v_{as}(\text{Fe-O-Fe})+v(\text{Fe-OH}) = 744.4$ $\Delta(^{18}\text{O}_2) = -39.4$ $\Delta(^{16}\text{O}^{18}\text{O}) = -13.8$ $\Delta(\text{D}) = -9.15$ $r(\text{Fe}\dots\text{Fe}) = 3.27 \text{ \AA}$	
OC19 -OH/-OH		$v_{as}(\text{Fe-O-Fe})+v(\text{Fe-OH}) = 727.4$ $\Delta(^{18}\text{O}_2) = -41.3$ $\Delta(^{16}\text{O}^{18}\text{O}) = -16.2$ $\Delta(\text{D}) = -14.0$ $r(\text{Fe}\dots\text{Fe}) = 3.14 \text{ \AA}$	
OC20 -OH/-OH		$v_{as}(\text{Fe-O-Fe})+v(\text{Fe-OH}) = 723.9$ $\Delta(^{18}\text{O}_2) = -39.5$ $\Delta(^{16}\text{O}^{18}\text{O}) = -18.8$ $\Delta(\text{D}) = -7.7$ $r(\text{Fe}\dots\text{Fe}) = 3.27 \text{ \AA}$	

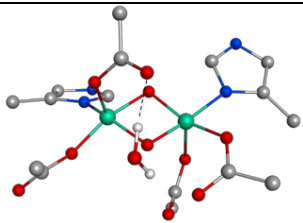
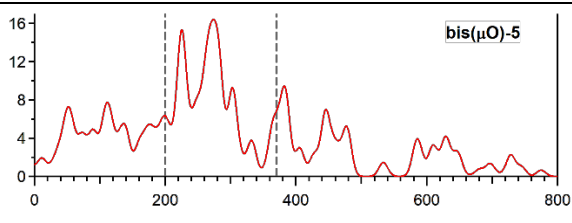
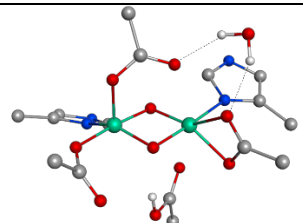
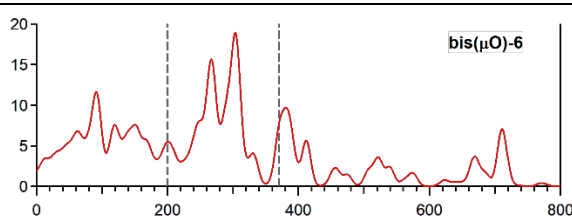
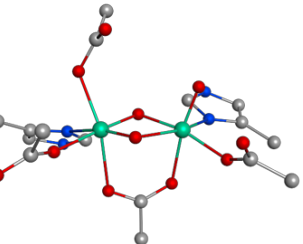
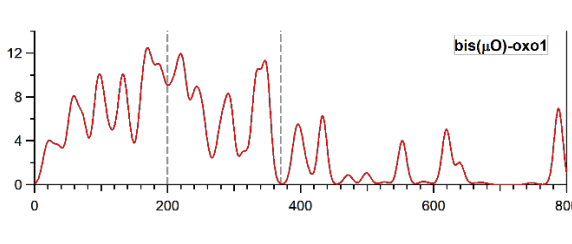
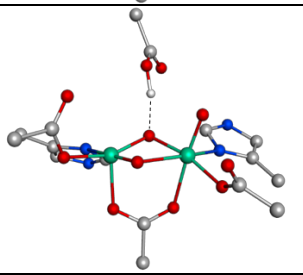
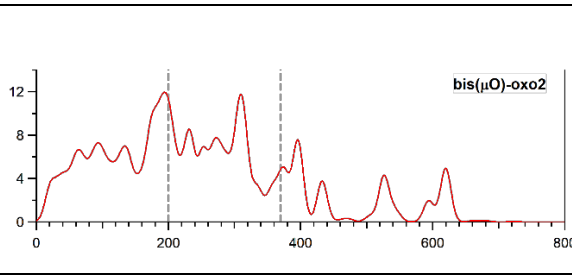
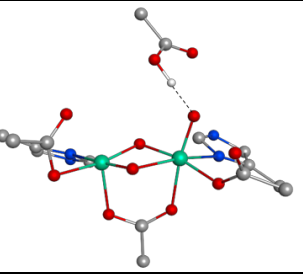
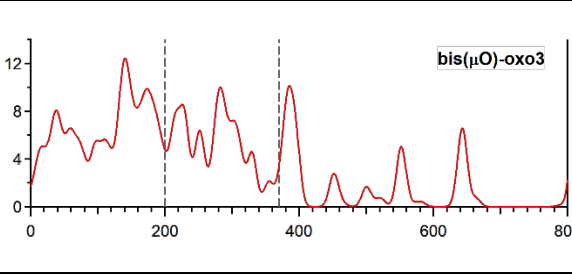
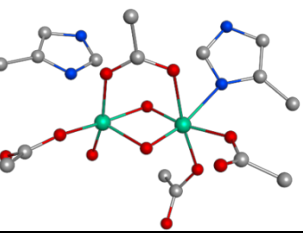
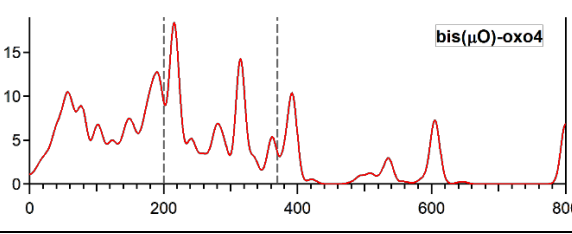
OC21 -OH/-OH		$\nu(\text{Fe-OH}) = 694.3$ $\Delta(^{18}\text{O}_2) = -21.6$ $\Delta(^{16}\text{O}^{18}\text{O}) = -21.4$ $\Delta(\text{D}) = -19.1$	
		$r(\text{Fe}\dots\text{Fe}) = 3.35 \text{ \AA}$	
OC23 -OH/-OH		$\nu_{\text{as}}(\text{Fe-O-Fe}) + \nu(\text{Fe-OH}) = 714.6$ $\Delta(^{18}\text{O}_2) = -33.2$ $\Delta(^{16}\text{O}^{18}\text{O}) = -25.3$ $\Delta(\text{D}) = -9.8$	
		$r(\text{Fe}\dots\text{Fe}) = 3.14 \text{ \AA}$	
OC32 -OH/-OH		$\nu_{\text{as}}(\text{Fe-O-Fe}) + \nu(\text{Fe-OH}) = 688.1$ $\Delta(^{18}\text{O}_2) = -22.5$ $\Delta(^{16}\text{O}^{18}\text{O}) = -5.5$ $\Delta(\text{D}) = -3.4$	
		$r(\text{Fe}\dots\text{Fe}) = 3.16 \text{ \AA}$	
OC33 -OH/-OH		$\nu_{\text{as}}(\text{Fe-O-Fe}) + \nu(\text{Fe-OH}) = 694.9$ $\Delta(^{18}\text{O}_2) = -33.7$ $\Delta(^{16}\text{O}^{18}\text{O}) = -16.0$ $\Delta(\text{D}) = -20.6$	
		$r(\text{Fe}\dots\text{Fe}) = 3.16 \text{ \AA}$	
Model Name	Structure	r/cm^{-1} ; information relevant to XAS	NRVS
OC34 -OH/-OH		$\nu_{\text{as}}(\text{Fe-O-Fe}) + \nu(\text{Fe-OH}) = 716.9$ $\Delta(^{18}\text{O}_2) = -38.2$ $\Delta(^{16}\text{O}^{18}\text{O}) = -20.4$ $\Delta(\text{D}) = -16.1$	
		$r(\text{Fe}\dots\text{Fe}) = 3.13 \text{ \AA}$	
OC6 -OH/-H ₂ O		$\nu(\text{Fe-OH}) = 719.6$ $\Delta(^{18}\text{O}_2) = -28.4$ $\Delta(^{16}\text{O}^{18}\text{O}) = -20.6$ $\Delta(\text{D}) = -4.2$	
		$r(\text{Fe}\dots\text{Fe}) = 3.13 \text{ \AA}$	

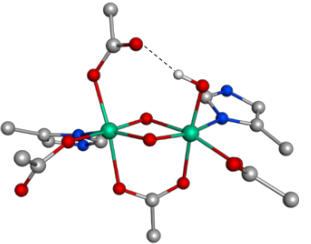
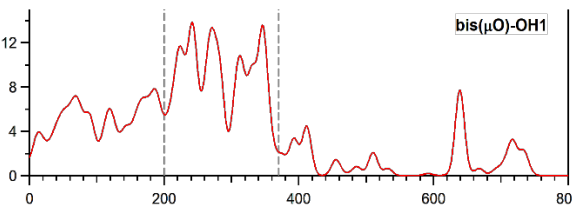
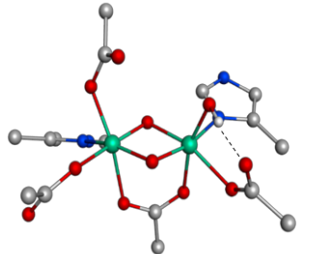
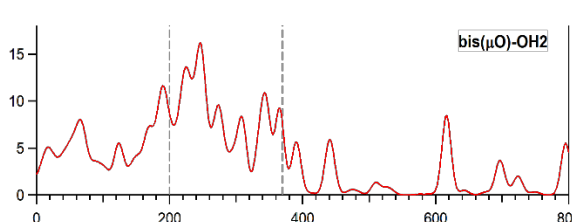
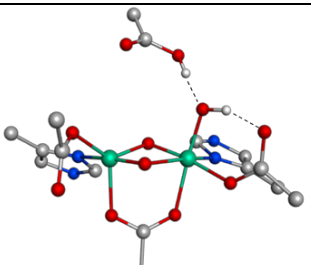
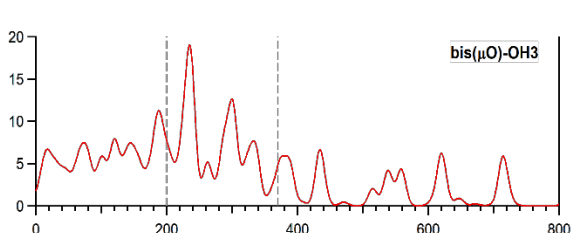
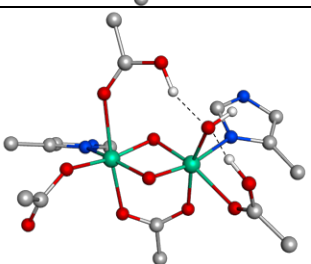
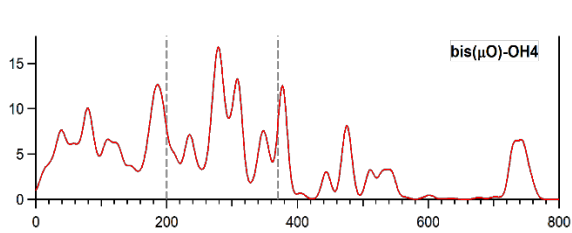
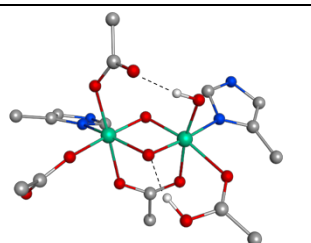
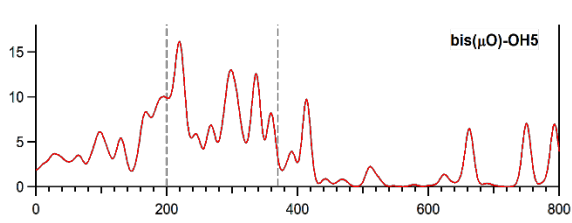
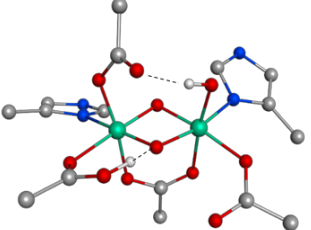
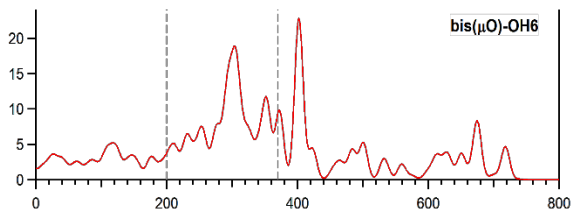
OC12 -OH/-H ₂ O		$\nu(\text{Fe-OH}) = 731.9$ $\Delta(^{18}\text{O}_2) = -30.5$ $\Delta(^{16}\text{O}^{18}\text{O}) = -30.5$ $\Delta(\text{D}) = -28.6$ $r(\text{Fe}\dots\text{Fe}) = 3.39 \text{ \AA}$	
OC36 -OH/-H ₂ O		$\nu_{\text{as}}(\text{Fe-O-Fe}) = 727.5$ $\Delta(^{18}\text{O}_2) = -29.7$ $\Delta(^{16}\text{O}^{18}\text{O}) = -21.1$ $\Delta(\text{D}) = -1.5$ $r(\text{Fe}\dots\text{Fe}) = 3.45 \text{ \AA}$	
OC8 -H ₂ O/=O		$\nu_{\text{as}}(\text{Fe-O-Fe}) = 818.2$ $\Delta(^{18}\text{O}_2) = -43.5$ $\Delta(^{16}\text{O}^{18}\text{O}) = -43.2$ $\Delta(\text{D}) = 4.3$ $r(\text{Fe}\dots\text{Fe}) = 3.38 \text{ \AA}$	
OC14 -H ₂ O/=O		$\nu_{\text{as}}(\text{Fe-O-Fe}) = 611.7$ $\Delta(^{18}\text{O}_2) = -24.2$ $\Delta(^{16}\text{O}^{18}\text{O}) = -17.7$ $\Delta(\text{D}) = 0.1$ $r(\text{Fe}\dots\text{Fe}) = 3.25 \text{ \AA}$	
Model Name	Structure	rR/cm^{-1} ; information relevant to XAS	NRVS
OC30 -H ₂ O/=O		$\nu(\text{Fe=O}) = 796.7$ $\Delta(^{18}\text{O}_2) = -38.5$ $\Delta(^{16}\text{O}^{18}\text{O}) = -38.5$ $\Delta(\text{D}) = 2.8$ $r(\text{Fe}\dots\text{Fe}) = 3.12 \text{ \AA}$	
OC31 -H ₂ O/=O		$\nu(\text{Fe=O}) = 766.4$ $\Delta(^{18}\text{O}_2) = -41.2$ $\Delta(^{16}\text{O}^{18}\text{O}) = -41.1$ $\Delta(\text{D}) = -0.6$ $r(\text{Fe}\dots\text{Fe}) = 3.22 \text{ \AA}$	
OC37 -H ₂ O/=O		$\nu(\text{Fe=O}) = 783.6$ $\Delta(^{18}\text{O}_2) = -37.6$ $\Delta(^{16}\text{O}^{18}\text{O}) = -37.6$ $\Delta(\text{D}) = -10.0$	

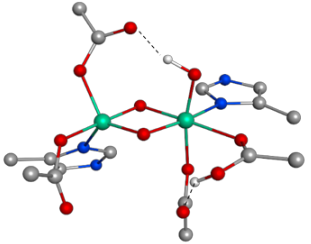
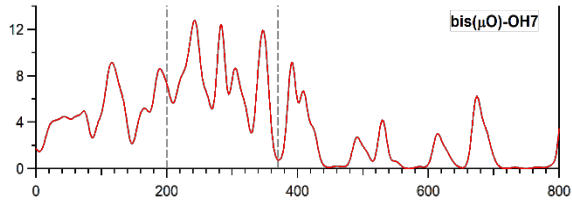
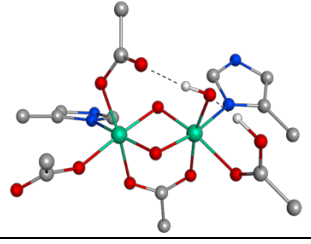
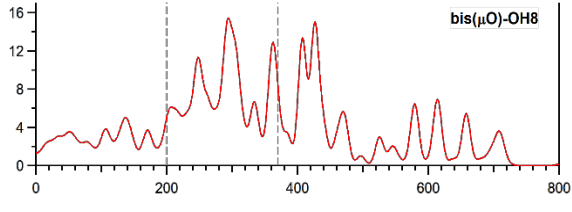
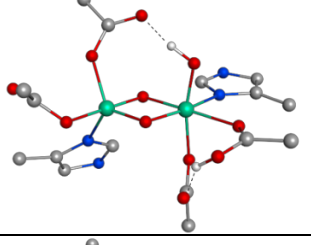
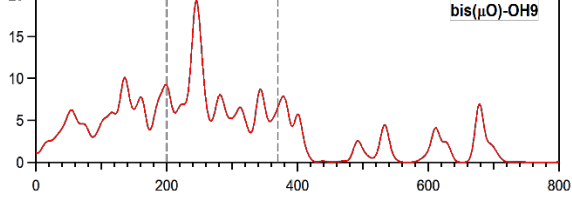
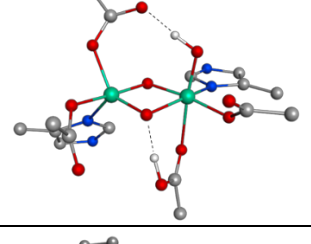
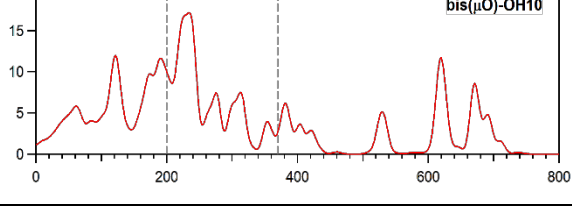
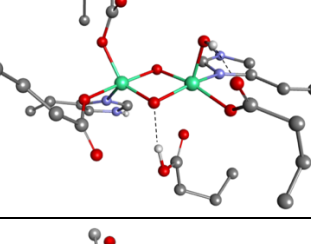
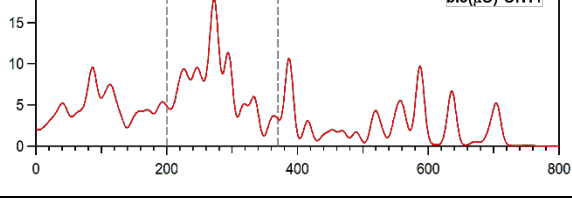
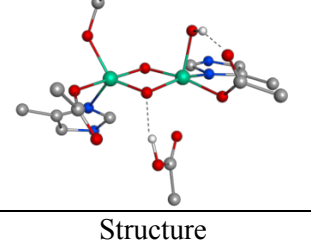
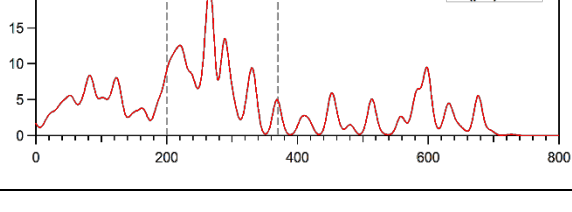
		$r(\text{Fe}\dots\text{Fe}) = 3.10 \text{ \AA}$	
OC38 -H ₂ O/=O		$\nu(\text{Fe}=\text{O}) = 775.9$ $\Delta(^{18}\text{O}_2) = -31.0$ $\Delta(^{16}\text{O}^{18}\text{O}) = -31.0$ $\Delta(\text{D}) = 9.5$ $r(\text{Fe}\dots\text{Fe}) = 3.18 \text{ \AA}$	
OC5 =O/=O		$\nu(\text{Fe}=\text{O}) = 927.1$ $\Delta(^{18}\text{O}_2) = -35.8$ $\Delta(^{16}\text{O}^{18}\text{O}) = 0.2$ $\Delta(\text{D}) = -4.9$ $r(\text{Fe}\dots\text{Fe}) = 3.67 \text{ \AA}$	
OC7 =O/=O		$\nu(\text{Fe}=\text{O}) = 900.9$ $\Delta(^{18}\text{O}_2) = -39.1$ $\Delta(^{16}\text{O}^{18}\text{O}) = -38.9$ $\Delta(\text{D}) = \text{N/A}$ $r(\text{Fe}\dots\text{Fe}) = 3.34 \text{ \AA}$	
OC28 =O/=O		$\nu(\text{Fe}=\text{O}) = 855.6$ $\Delta(^{18}\text{O}_2) = -41.7$ $\Delta(^{16}\text{O}^{18}\text{O}) = -41.6$ $\Delta(\text{D}) = -1.4$ $r(\text{Fe}\dots\text{Fe}) = 2.99 \text{ \AA}$	
Model Name	Structure	rR/cm^{-1} ; information relevant to XAS	NRVS
OC29 =O/=O		$\nu(\text{Fe}=\text{O}) = 939.8$ $\Delta(^{18}\text{O}_2) = -40.2$ $\Delta(^{16}\text{O}^{18}\text{O}) = -38.4$ $\Delta(\text{D}) = -0.0$ $r(\text{Fe}\dots\text{Fe}) = 3.62 \text{ \AA}$	
OC4 =O		$\nu(\text{Fe}=\text{O}) = 898.9$ $\Delta(^{18}\text{O}_2) = -69.0$ $\Delta(^{16}\text{O}^{18}\text{O}) = -9.53$ $\Delta(\text{D}) = -24.5$	

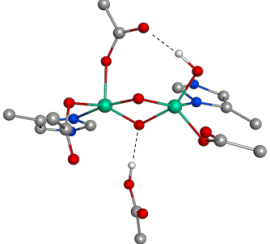
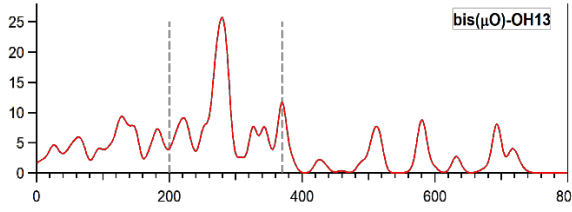
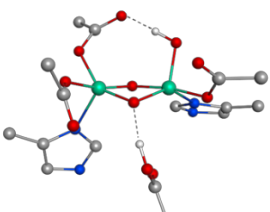
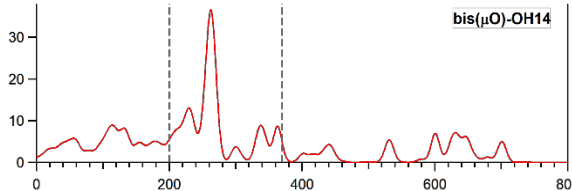
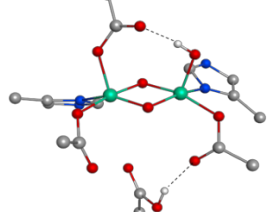
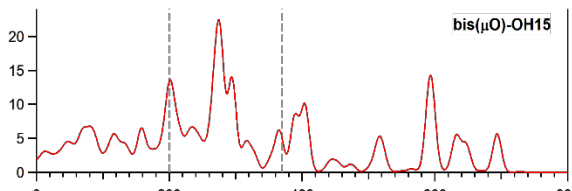
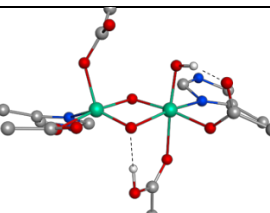
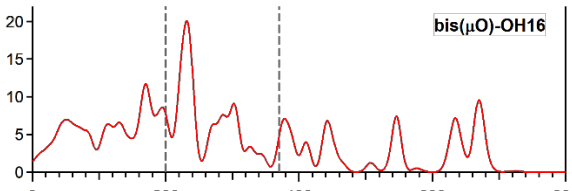
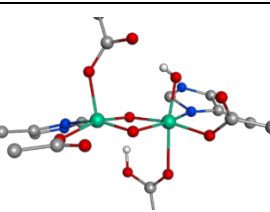
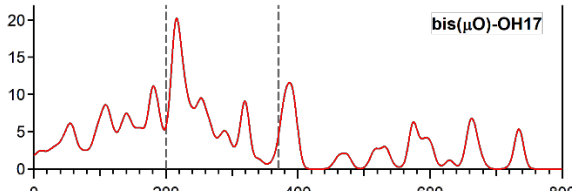
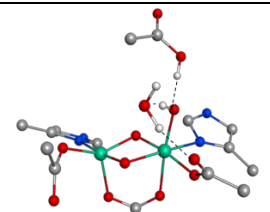
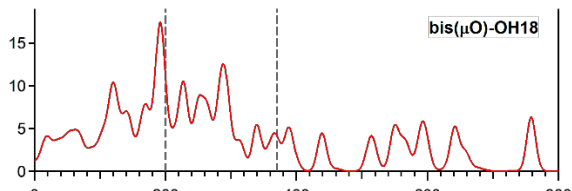
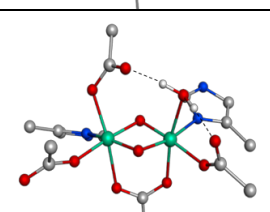
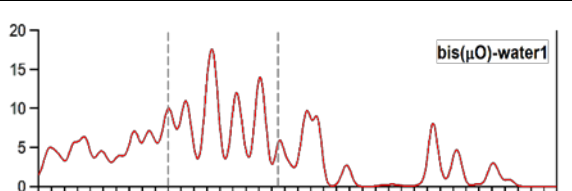
		$r(\text{Fe}\dots\text{Fe}) = 3.14 \text{ \AA}$	
OC27 -OH		$v_{\text{as}}(\text{Fe-O-Fe}) + v(\text{Fe-OH}) = 750.7$ $\Delta(^{18}\text{O}_2) = -34.4$ $\Delta(^{16}\text{O}^{18}\text{O}) = -25.8$ $\Delta(\text{D}) = -21$ $r(\text{Fe}\dots\text{Fe}) = 3.24 \text{ \AA}$	
Model Name	Structure	rR/cm^{-1} ; information relevant to XAS	NRVS
$\mu\text{O}\mu\text{OH-1}$		$v_{\text{as}}(\text{Fe-O-Fe}) = 786.9$ $\Delta(^{18}\text{O}_2) = -26.4$ $\Delta(^{16}\text{O}^{18}\text{O}) = -26.4$ $\Delta(\text{D}) = 1.9$ $r(\text{Fe}\dots\text{Fe}) = 2.92 \text{ \AA}$	
$\mu\text{O}\mu\text{OH-2}$		$v(\text{Fe-OH}) = 740.83$ $\Delta(^{18}\text{O}_2) = -30.2$ $\Delta(^{16}\text{O}^{18}\text{O}) = -30.2$ $\Delta(\text{D}) = -4.6$ $r(\text{Fe}\dots\text{Fe}) = 3.02 \text{ \AA}$	
$\mu\text{O}\mu\text{OH-3}$		$v(\text{Fe-OH}) = 583.3$ $\Delta(^{18}\text{O}_2) = -19.6$ $\Delta(^{16}\text{O}^{18}\text{O}) = -18.7$ $\Delta(\text{D}) = -6.2$ $r(\text{Fe}\dots\text{Fe}) = 2.93 \text{ \AA}$	
$\mu\text{O}\mu\text{OH-4}$		$v(\text{Fe-OH}) = 712.7$ $\Delta(^{18}\text{O}_2) = -15.3$ $\Delta(^{16}\text{O}^{18}\text{O}) = -15.2$ $\Delta(\text{D}) = -0.27$ $r(\text{Fe}\dots\text{Fe}) = 2.97 \text{ \AA}$	
$\mu\text{O}\mu\text{OH-5}$		$v(\text{Fe=O}) = 804.8$ $\Delta(^{18}\text{O}_2) = -40.9$ $\Delta(^{16}\text{O}^{18}\text{O}) = -40.9$ $\Delta(\text{D}) = 0.1$ $r(\text{Fe}\dots\text{Fe}) = 3.01 \text{ \AA}$	

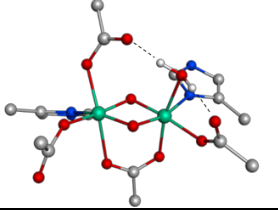
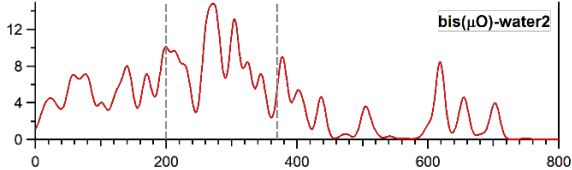
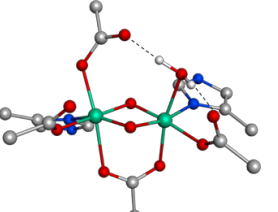
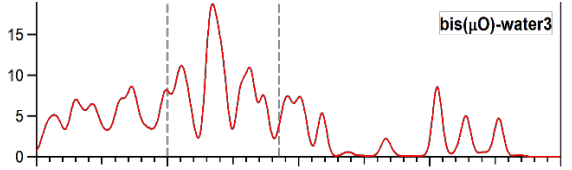
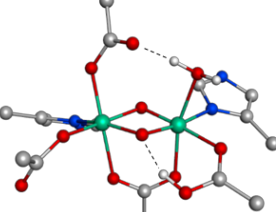
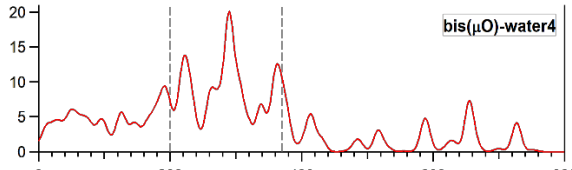
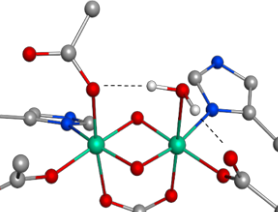
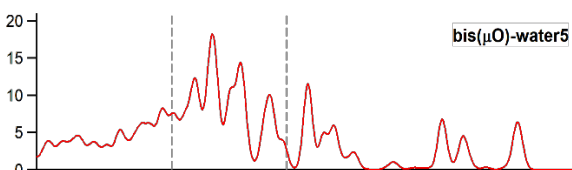
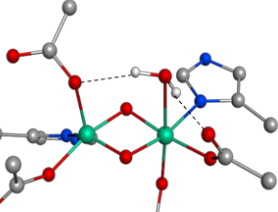
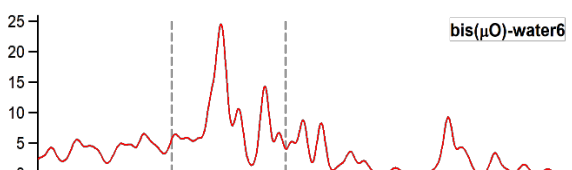
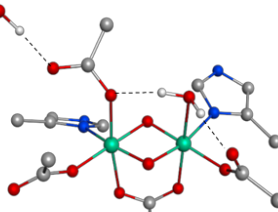
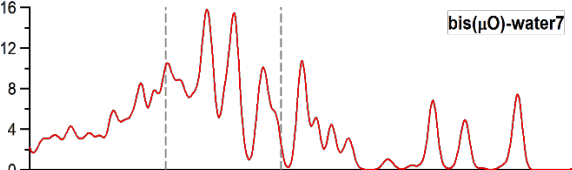
$\mu\text{O}\mu\text{OH-6}$		$v_{\text{as}}(\text{Fe-O-Fe}) = 719.6$ $\Delta(^{18}\text{O}_2) = -29.3$ $\Delta(^{16}\text{O}^{18}\text{O}) = -29.0$ $\Delta(\text{D}) = 0.5$ $r(\text{Fe}\dots\text{Fe}) = 2.86 \text{ \AA}$	
$\mu\text{O}\mu\text{OH-7}$		$v_{\text{as}}(\text{Fe-O-Fe}) = 775.3$ $\Delta(^{18}\text{O}_2) = -32.7$ $\Delta(^{16}\text{O}^{18}\text{O}) = -31.2$ $\Delta(\text{D}) = 1.3$ $r(\text{Fe}\dots\text{Fe}) = 2.98 \text{ \AA}$	
$\mu\text{O}\mu\text{OH-8}$		$v_{\text{as}}(\text{Fe-O-Fe}) = 783.3$ $\Delta(^{18}\text{O}_2) = -36.5$ $\Delta(^{16}\text{O}^{18}\text{O}) = -35.8$ $\Delta(\text{D}) = 17.8$ $r(\text{Fe}\dots\text{Fe}) = 3.00 \text{ \AA}$	
Model Name	Structure	r/cm^{-1} ; information relevant to XAS	NRVS
$\text{bis}(\mu\text{O})-1$		$v(\text{breathing}) = 712.1$ $\Delta(^{18}\text{O}_2) = -32.3$ $\Delta(^{16}\text{O}^{18}\text{O}) = -12.5$ $\Delta(\text{D}) = 0$ $r(\text{Fe}\dots\text{Fe}) = 2.65 \text{ \AA}$	
$\text{bis}(\mu\text{O})-2$		$v(\text{breathing}) = 724.1$ $\Delta(^{18}\text{O}_2) = -41.2$ $\Delta(^{16}\text{O}^{18}\text{O}) = -23.5$ $\Delta(\text{D}) = 0.0$ $r(\text{Fe}\dots\text{Fe}) = 2.68 \text{ \AA}$	
$\text{bis}(\mu\text{O})-3$		$v(\text{breathing}) = 711.6$ $\Delta(^{18}\text{O}_2) = -31.7$ $\Delta(^{16}\text{O}^{18}\text{O}) = -23.0$ $\Delta(\text{D}) = -0.1$ $r(\text{Fe}\dots\text{Fe}) = 2.73 \text{ \AA}$	
$\text{bis}(\mu\text{O})-4$		$v(\text{breathing}) = 696.9$ $\Delta(^{18}\text{O}_2) = -33.0$ $\Delta(^{16}\text{O}^{18}\text{O}) = -17.6$ $\Delta(\text{D}) = 0.8$ $r(\text{Fe}\dots\text{Fe}) = 2.73 \text{ \AA}$	

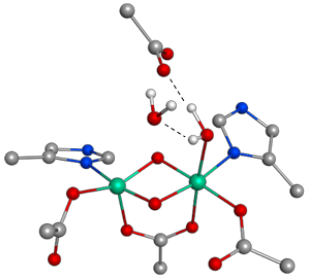
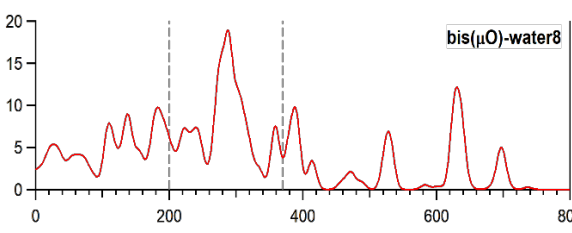
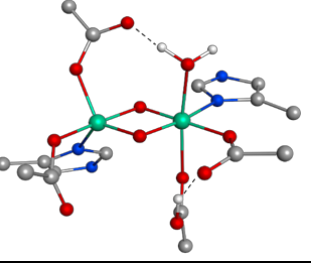
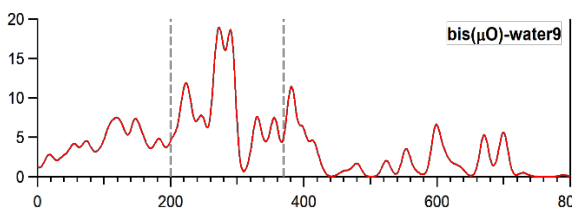
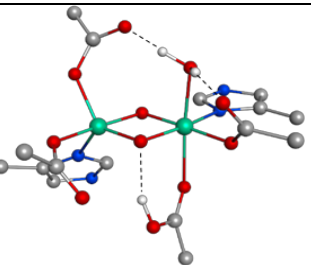
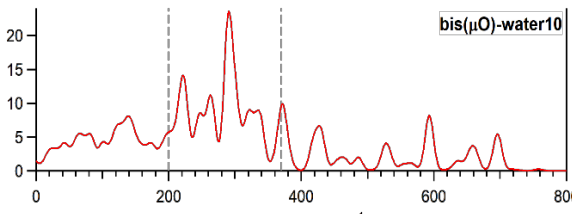
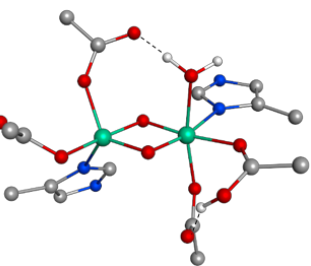
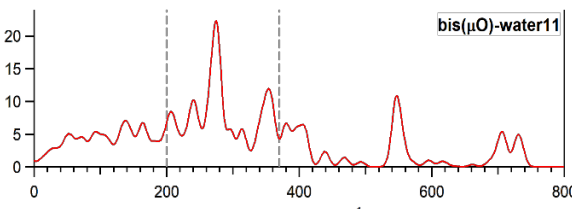
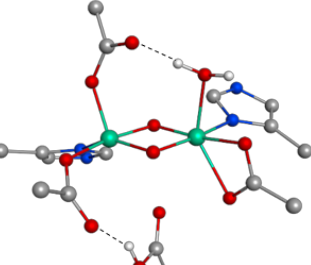
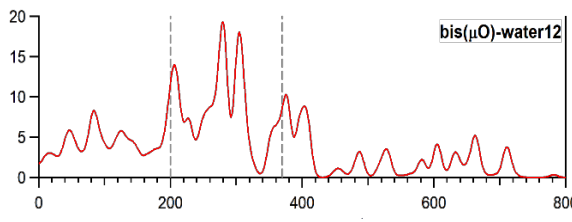
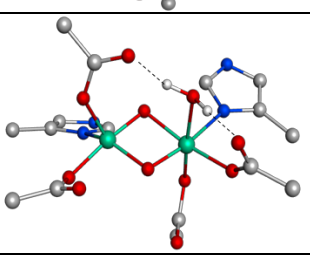
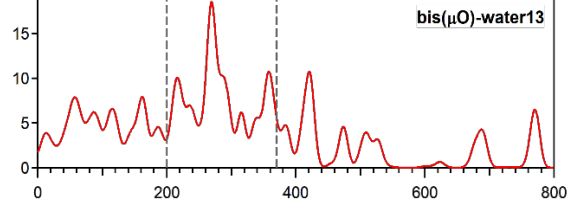
bis(μ O)-5		$\nu(\text{breathing}) = 728.2$ $\Delta(^{18}\text{O}_2) = -40.3$ $\Delta(^{16}\text{O}^{18}\text{O}) = -33.5$ $\Delta(\text{D}) = -3.9$ $r(\text{Fe}\dots\text{Fe}) = 2.76 \text{ \AA}$	
bis(μ O)-6		$\nu(\text{breathing}) = 710.2$ $\Delta(^{18}\text{O}_2) = -25.5$ $\Delta(^{16}\text{O}^{18}\text{O}) = -21.5$ $\Delta(\text{D}) = 4.1$ $r(\text{Fe}\dots\text{Fe}) = 2.73 \text{ \AA}$	
Model Name	Structure	$r\text{R}/\text{cm}^{-1}$; information relevant to XAS	NRVS
bis(μ O)-oxo1		$\nu(\text{Fe}=\text{O}) = 787.7$ $\Delta(^{18}\text{O}_2) = -35.1$ $\Delta(^{16}\text{O}^{18}\text{O}) = -31.1$ $\Delta(\text{D}) = 0.0$ $r(\text{Fe}\dots\text{Fe}) = 2.82 \text{ \AA}$	
bis(μ O)-oxo2		$\nu_{\text{as}}(\text{Fe}-\text{O}-\text{Fe}) = 620.2$ $\Delta(^{18}\text{O}_2) = -43.5$ $\Delta(^{16}\text{O}^{18}\text{O}) = -43.1$ $\Delta(\text{D}) = -0.4$ $r(\text{Fe}\dots\text{Fe}) = 2.84 \text{ \AA}$	
bis(μ O)-oxo3		$\nu(\text{Fe}=\text{O}) = 810.3$ $\Delta(^{18}\text{O}_2) = -36.2$ $\Delta(^{16}\text{O}^{18}\text{O}) = -35.4$ $\Delta(\text{D}) = 0.1$ $r(\text{Fe}\dots\text{Fe}) = 2.77 \text{ \AA}$	
bis(μ O)-oxo4		$\nu(\text{Fe}=\text{O}) = 799.0$ $\Delta(^{18}\text{O}_2) = -35.1$ $\Delta(^{16}\text{O}^{18}\text{O}) = -34.5$ $r(\text{Fe}\dots\text{Fe}) = 2.79 \text{ \AA}$	
bis(μ O)-OH1		$\nu_{\text{as}}(\text{Fe}-\text{O}-\text{Fe}) = 733.9$ $\Delta(^{18}\text{O}_2) = -47.3$ $\Delta(^{16}\text{O}^{18}\text{O}) = -47.0$ $\Delta(\text{D}) = -13.1$	

		$r(\text{Fe}\dots\text{Fe}) = 2.82 \text{ \AA}$	 bis(μO)-OH1
bis(μO)-OH2		$\nu_{\text{as}}(\text{Fe-O-Fe}) = 696.5$ $\Delta(^{18}\text{O}_2) = -25.8$ $\Delta(^{16}\text{O}^{18}\text{O}) = -23.3$ $\Delta(\text{D}) = 4.9$	 bis(μO)-OH2
		$r(\text{Fe}\dots\text{Fe}) = 2.79 \text{ \AA}$	
bis(μO)-OH3		$\nu_{\text{as}}(\text{Fe-O-Fe}) = 713.8$ $\Delta(^{18}\text{O}_2) = -29.4$ $\Delta(^{16}\text{O}^{18}\text{O}) = -29.1$ $\Delta(\text{D}) = -4.7$	 bis(μO)-OH3
		$r(\text{Fe}\dots\text{Fe}) = 2.76 \text{ \AA}$	
bis(μO)-OH4		$\nu_{\text{as}}(\text{Fe-O-Fe}) = 729.8$ $\Delta(^{18}\text{O}_2) = -38.6$ $\Delta(^{16}\text{O}^{18}\text{O}) = -37.8$ $\Delta(\text{D}) = 10.7$	 bis(μO)-OH4
		$r(\text{Fe}\dots\text{Fe}) = 2.72 \text{ \AA}$	
Model Name	Structure	rR/cm^{-1} ; information relevant to XAS	NRVS
bis(μO)-OH5		$\nu(\text{Fe-OH}) = 662.9$ $\Delta(^{18}\text{O}_2) = -49.2$ $\Delta(^{16}\text{O}^{18}\text{O}) = -49.0$ $\Delta(\text{D}) = -20.5$	 bis(μO)-OH5
		$r(\text{Fe}\dots\text{Fe}) = 2.81 \text{ \AA}$	
bis(μO)-OH6		$\nu(\text{breathing}) = 718.0$ $\Delta(^{18}\text{O}_2) = -33.4$ $\Delta(^{16}\text{O}^{18}\text{O}) = -27.6$ $\Delta(\text{D}) = -2.2$	 bis(μO)-OH6
		$r(\text{Fe}\dots\text{Fe}) = 2.71 \text{ \AA}$	

bis(μ O)-OH7		$v_{as}(\text{Fe-O-Fe}) = 673.9$ $\Delta(^{18}\text{O}_2) = -27.0$ $\Delta(^{16}\text{O}^{18}\text{O}) = -7.1$ $\Delta(\text{D}) = 2.0$	
		$r(\text{Fe}\dots\text{Fe}) = 2.80 \text{ \AA}$	
bis(μ O)-OH8		$v(\text{breathing}) = 710.3$ $\Delta(^{18}\text{O}_2) = -41.0$ $\Delta(^{16}\text{O}^{18}\text{O}) = -23.6$ $\Delta(\text{D}) = -1.9$	
		$r(\text{Fe}\dots\text{Fe}) = 2.69 \text{ \AA}$	
bis(μ O)-OH9		$v(\text{Fe-OH}) = 678.1$ $\Delta(^{18}\text{O}_2) = -26.4$ $\Delta(^{16}\text{O}^{18}\text{O}) = -22.6$ $\Delta(\text{D}) = 1.8$	
		$r(\text{Fe}\dots\text{Fe}) = 2.80 \text{ \AA}$	
bis(μ O)-OH10		$v(\text{breathing}) = 691.1$ $\Delta(^{18}\text{O}_2) = -34.5$ $\Delta(^{16}\text{O}^{18}\text{O}) = -23.2$ $\Delta(\text{D}) = 2.4$	
		$r(\text{Fe}\dots\text{Fe}) = 2.80 \text{ \AA}$	
bis(μ O)-OH11		$v(\text{breathing}) = 704.5$ $\Delta(^{18}\text{O}_2) = -28.1$ $\Delta(^{16}\text{O}^{18}\text{O}) = -20.9$ $\Delta(\text{D}) = -2.3$	
		$r(\text{Fe}\dots\text{Fe}) = 2.74 \text{ \AA}$	
bis(μ O)-OH12		$v(\text{breathing}) = 676.4$ $\Delta(^{18}\text{O}_2) = -41.3$ $\Delta(^{16}\text{O}^{18}\text{O}) = -9.4$ $\Delta(\text{D}) = 0.2$	
		$r(\text{Fe}\dots\text{Fe}) = 2.76 \text{ \AA}$	
Model Name	Structure	rR/cm^{-1} ; information relevant to XAS	NRVS
bis(μ O)-OH13		$v(\text{breathing}) = 724.6$ $\Delta(^{18}\text{O}_2) = -48.4$ $\Delta(^{16}\text{O}^{18}\text{O}) = -25.3$ $\Delta(\text{D}) = -7.9$	

		$r(\text{Fe}\dots\text{Fe}) = 2.73 \text{ \AA}$	
bis(μO)-OH14		$\nu(\text{breathing}) = 700.4$ $\Delta(^{18}\text{O}_2) = -37.5$ $\Delta(^{16}\text{O}^{18}\text{O}) = -10.3$ $\Delta(\text{D}) = -1.4$ $r(\text{Fe}\dots\text{Fe}) = 2.73 \text{ \AA}$	
bis(μO)-OH15		$\nu(\text{breathing}) = 693.8$ $\Delta(^{18}\text{O}_2) = -26.6$ $\Delta(^{16}\text{O}^{18}\text{O}) = -17.1$ $\Delta(\text{D}) = 1.2$ $r(\text{Fe}\dots\text{Fe}) = 2.75 \text{ \AA}$	
bis(μO)-OH16		$\nu(\text{breathing}) = 674.9$ $\Delta(^{18}\text{O}_2) = -24.6$ $\Delta(^{16}\text{O}^{18}\text{O}) = -19.7$ $\Delta(\text{D}) = -1.3$ $r(\text{Fe}\dots\text{Fe}) = 2.82 \text{ \AA}$	
bis(μO)-OH17		$\nu(\text{breathing}) = 734.0$ $\Delta(^{18}\text{O}_2) = -32.7$ $\Delta(^{16}\text{O}^{18}\text{O}) = -29.9$ $\Delta(\text{D}) = 4.5$ $r(\text{Fe}\dots\text{Fe}) = 2.83 \text{ \AA}$	
bis(μO)-OH18		$\nu(\text{Fe}=\text{O}) = 758.2$ $\Delta(^{18}\text{O}_2) = -36.5$ $\Delta(^{16}\text{O}^{18}\text{O}) = -35.0$ $\Delta(\text{D}) = 1.1$ $r(\text{Fe}\dots\text{Fe}) = 2.74 \text{ \AA}$	
bis(μO)-H ₂ O1		$\nu(\text{breathing}) = 702.3$ $\Delta(^{18}\text{O}_2) = -35.8$ $\Delta(^{16}\text{O}^{18}\text{O}) = -17.1$ $\Delta(\text{D}) = -0.3$ $r(\text{Fe}\dots\text{Fe}) = 2.72 \text{ \AA}$	

Model Name	Structure	rR/cm^{-1} ; information relevant to XAS	NRVS
bis(μ O)-H ₂ O ₂		$\nu(\text{breathing}) = 702.9$ $\Delta(^{18}\text{O}_2) = -34.9$ $\Delta(^{16}\text{O}^{18}\text{O}) = -20.9$ $\Delta(D) = 0.1$ $r(\text{Fe}\dots\text{Fe}) = 2.72 \text{ \AA}$	
bis(μ O)-H ₂ O ₃		$\nu(\text{breathing}) = 705.9$ $\Delta(^{18}\text{O}_2) = -33.3$ $\Delta(^{16}\text{O}^{18}\text{O}) = -22.7$ $\Delta(D) = 0.5$ $r(\text{Fe}\dots\text{Fe}) = 2.71 \text{ \AA}$	
bis(μ O)-H ₂ O ₄		$\nu(\text{breathing}) = 726.9$ $\Delta(^{18}\text{O}_2) = -40.3$ $\Delta(^{16}\text{O}^{18}\text{O}) = -31.4$ $\Delta(D) = 0.0$ $r(\text{Fe}\dots\text{Fe}) = 2.74 \text{ \AA}$	
bis(μ O)-H ₂ O ₅		$\nu_{\text{as}}(\text{Fe-O-Fe}) = 709.6$ $\Delta(^{18}\text{O}_2) = -29.1$ $\Delta(^{16}\text{O}^{18}\text{O}) = -25.9$ $\Delta(D) = 1.5$ $r(\text{Fe}\dots\text{Fe}) = 2.69 \text{ \AA}$	
bis(μ O)-H ₂ O ₆		$\nu(\text{breathing}) = 682.1$ $\Delta(^{18}\text{O}_2) = -27.4$ $\Delta(^{16}\text{O}^{18}\text{O}) = -16.0$ $\Delta(D) = 1.5$ $r(\text{Fe}\dots\text{Fe}) = 2.70 \text{ \AA}$	
bis(μ O)-H ₂ O ₇		$\nu_{\text{as}}(\text{Fe-O-Fe}) = 718.6$ $\Delta(^{18}\text{O}_2) = -31.8$ $\Delta(^{16}\text{O}^{18}\text{O}) = -29.3$ $\Delta(D) = 2.7$ $r(\text{Fe}\dots\text{Fe}) = 2.69 \text{ \AA}$	
bis(μ O)-H ₂ O ₈		$\nu(\text{breathing}) = 695.7$ $\Delta(^{18}\text{O}_2) = -32.0$ $\Delta(^{16}\text{O}^{18}\text{O}) = -17.6$ $\Delta(D) = -0.7$	

		$r(\text{Fe}\dots\text{Fe}) = 2.69 \text{ \AA}$	
bis(μO)- H_2O_9		$\nu(\text{breathing}) = 700.2$ $\Delta(^{18}\text{O}_2) = -19.6$ $\Delta(^{16}\text{O}^{18}\text{O}) = -5.4$ $\Delta(\text{D}) = -8.4$ $r(\text{Fe}\dots\text{Fe}) = 2.74 \text{ \AA}$	
Model Name	Structure	$r\text{R}/\text{cm}^{-1}$; information relevant to XAS	NRVS
bis(μO)- H_2O_{10}		$\nu(\text{breathing}) = 696.5$ $\Delta(^{18}\text{O}_2) = -20.5$ $\Delta(^{16}\text{O}^{18}\text{O}) = -17.9$ $\Delta(\text{D}) = -0.4$ $r(\text{Fe}\dots\text{Fe}) = 2.75 \text{ \AA}$	
bis(μO)- H_2O_{11}		$\nu(\text{breathing}) = 733.8$ $\Delta(^{18}\text{O}_2) = -28.7$ $\Delta(^{16}\text{O}^{18}\text{O}) = -13.4$ $\Delta(\text{D}) = 0.6$ $r(\text{Fe}\dots\text{Fe}) = 2.74 \text{ \AA}$	
bis(μO)- H_2O_{12}		$\nu(\text{breathing}) = 710.6$ $\Delta(^{18}\text{O}_2) = -30.2$ $\Delta(^{16}\text{O}^{18}\text{O}) = -18.4$ $\Delta(\text{D}) = -0.2$ $r(\text{Fe}\dots\text{Fe}) = 2.76 \text{ \AA}$	
bis(μO)- H_2O_{13}		$\nu_{\text{as}}(\text{Fe-O-Fe}) = 689.9$ $\Delta(^{18}\text{O}_2) = -37.1$ $\Delta(^{16}\text{O}^{18}\text{O}) = -36.4$ $\Delta(\text{D}) = -0.0$ $r(\text{Fe}\dots\text{Fe}) = 2.80 \text{ \AA}$	

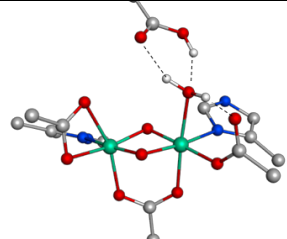
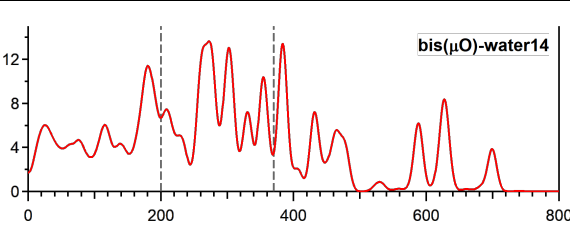
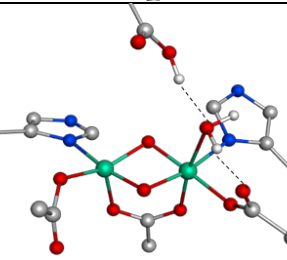
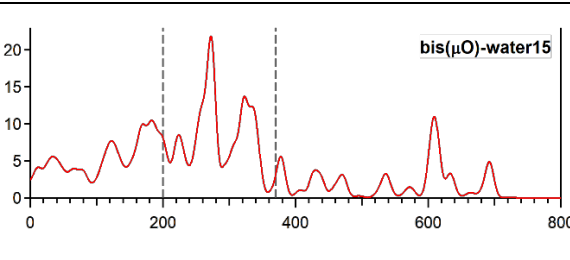
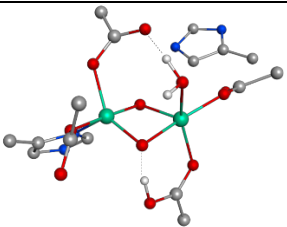
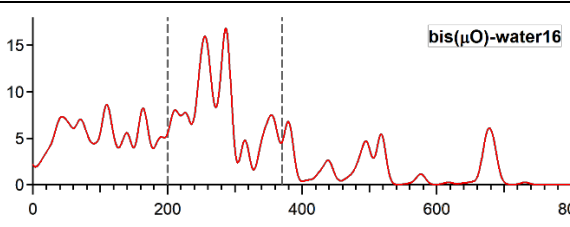
bis(μ O)- H ₂ O14		$\nu(\text{breathing}) = 699.4$ $\Delta(^{18}\text{O}_2) = -35.0$ $\Delta(^{16}\text{O}^{18}\text{O}) = -24.6$ $\Delta(\text{D}) = -0.1$ <hr/> $r(\text{Fe}\dots\text{Fe}) = 2.70 \text{ \AA}$	
bis(μ O)- H ₂ O15		$\nu(\text{breathing}) = 692.4$ $\Delta(^{18}\text{O}_2) = -39.8$ $\Delta(^{16}\text{O}^{18}\text{O}) = -9.8$ $\Delta(\text{D}) = -0.8$ <hr/> $r(\text{Fe}\dots\text{Fe}) = 2.71 \text{ \AA}$	
bis(μ O)- H ₂ O16		$\nu_{\text{as}}(\text{Fe-O-Fe}) = 683.6$ $\Delta(^{18}\text{O}_2) = -25.4$ $\Delta(^{16}\text{O}^{18}\text{O}) = -25.1$ $\Delta(\text{D}) = -1.7$ <hr/> $r(\text{Fe}\dots\text{Fe}) = 2.73 \text{ \AA}$	

Figure S11. DFT calibration for NRVS simulation. (a) Experimental and (b~e) DFT-simulated NRVS spectra of oxidized MMOH (unpublished results). From (b) to (e), the size of DFT models decreased. The model for (b) included up to the 3rd coordination sphere residues, while the others contained only the 1st coordination sphere residues. Truncation schemes used for each model are described in insets. Circles atoms were constrained during geometry optimizations. With the 1st coordination sphere models (c) to (e), the effects of the truncation schemes were tested. The smallest model used for (e) was prepared by following the conventional alpha carbon constraint (C_α) scheme, where the C_α 's of the side chains were replaced with hydrogen atoms that were placed at a distance of 1.1 Å from the neighboring carbon atoms. To constrain angles between the backbone and the side chains, in model (d), the backbone atoms adjacent to C_α 's were capped with hydrogen atoms. This angle constraint improved the NRVS simulation compared to (e). In (c), the model was further extended by including up to two adjacent backbone carbonyl groups. This additional extension only showed a minor improvement in the NRVS simulation compared to (d). Thus, the truncation scheme of (d) was used to save computational time. Finally, in (b), additional side chains that are H-bonded to the 1st coordination sphere were added, resulting in the best reproduction of the NRVS data among the models tested. Therefore, all the Q models described in this study were prepared using the model in (b).

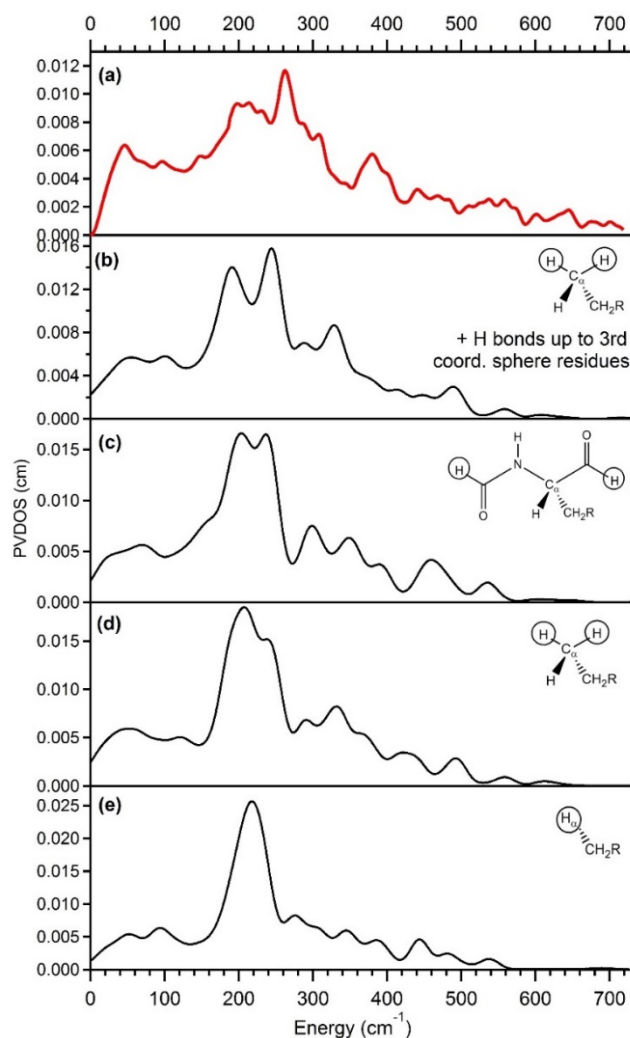


Figure S12 Selective labeling of the OH- and μ -O ligands in OC -OH/=O Q models. Three modes are present between 600 and 900 cm^{-1} : ν_1 , ν_2 , and ν_3 of Figure 4, bottom. In the $^{16}\text{O}_2$ isotopomer (figure below, top red spectrum), these vibrations are in descending order at 841 (ν_1), 722 (ν_2) and 691 (ν_3). Labeling of the terminal oxo and μ -O results with $^{18}\text{O}_2$ results in a downshift of ν_1 from 722 to 695 cm^{-1} (figure below, middle left blue spectrum). Labeling with $^{16}\text{O}^{18}\text{O}$ could result in ^{18}O incorporation into the OH-, terminal oxo, or μ -O ligands (figure below, bottom green spectra). For (μ - ^{18}O) and terminal ^{18}O , ν_2 is observed at 695 and 722 cm^{-1} (figure below, bottom left and bottom middle green spectra) which would not provide a mixed isotope signal relative to the middle left plot. Furthermore, the ^{18}OH isotopomer (figure below, bottom right green spectrum) results in a downshift of $\nu(\text{Fe-OH})$ and uncoupling of $\nu(\text{Fe-OH}) + \nu_{\text{as}}(\text{Fe-O-Fe})$; the resulting 720 cm^{-1} pure $\nu_{\text{as}}(\text{Fe-O-Fe})$ would not appear in the rR spectrum. Therefore, $^{18}\text{O}_2$ labeling must occur on the OH- and μ -O ligands (figure below, middle right blue spectrum), resulting in ν_2 at 686 cm^{-1} . This pairs well with the $^{16}\text{O}^{18}\text{O}$ (μ - ^{18}O) loaded isotopomer ν_2 (695 cm^{-1}).

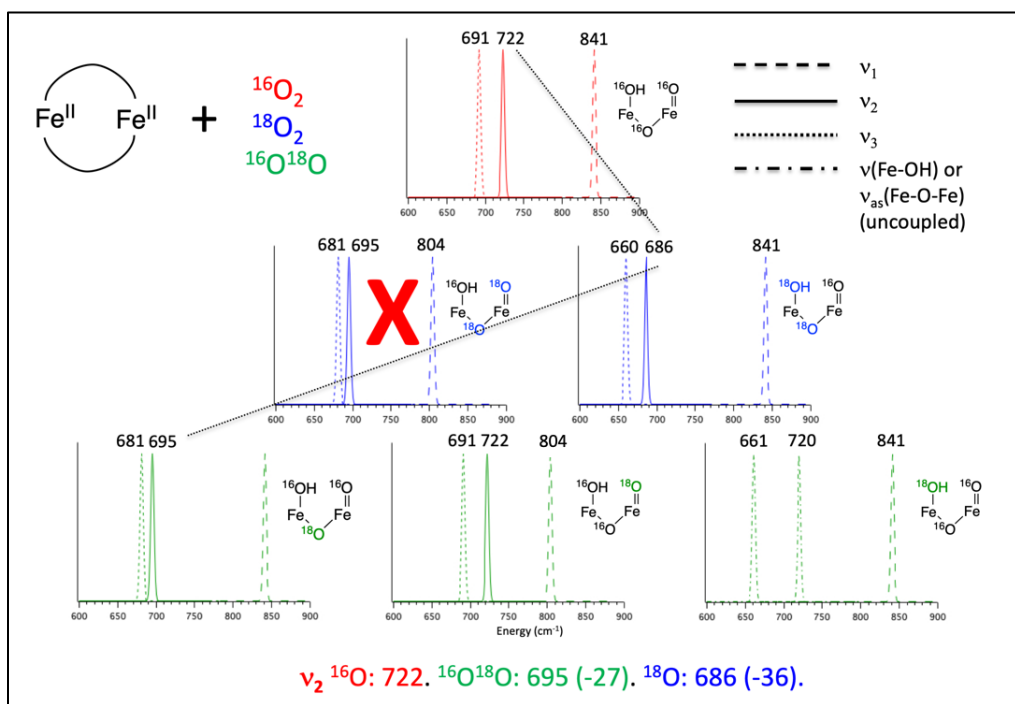
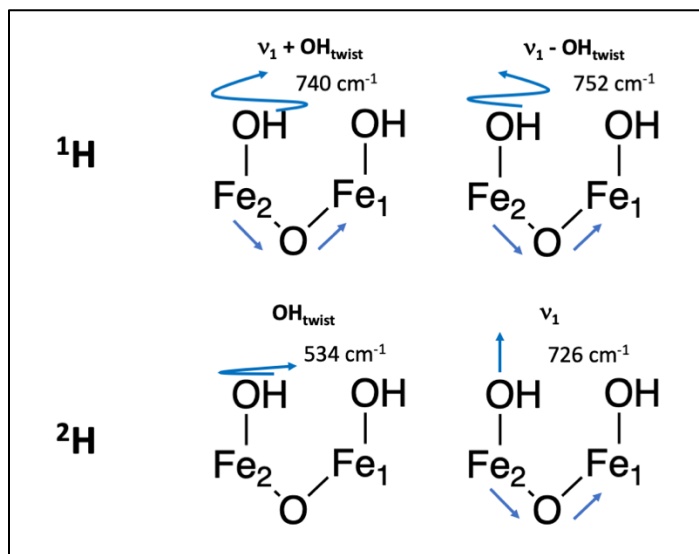


Figure S13 Effect of the OH torsional twist (OH_{twist}) on the in-plane $\nu(\text{Fe}_2\text{-OH}) + \nu_{\text{as}}(\text{Fe-O-Fe})$ mode (ν_1 Figure 4 middle), using **OC13** vibrations as an example. Mixing of OH_{twist} with ν_1 results in $\nu_1 + \text{OH}_{\text{twist}}$ and $\nu_1 - \text{OH}_{\text{twist}}$ modes, which contain significant $\text{Fe}_2\text{-OH}$ rotation (top row). Upon deuterium labeling (bottom row), the OH_{twist} mode no longer mixes and appears isolated at lower energy, resulting in a ν_1 mode at 726 cm^{-1} that is 14 cm^{-1} lower in energy than $\nu_1 + \text{OH}_{\text{twist}}$.



UV-vis TD-DFT Supplementary: Calibration and Analysis

The TD-DFT methodology was calibrated using the absorption spectrum (Figure S14 top) of the oxo-bridged biferric form of a ribonucleotide reductase (RnR) mutant (Y122F) that has been structurally defined by crystallography,²² with the O(H)_x ligands given by NRVS (manuscript in preparation; see Figure S15 for structure). The experimental absorption and rR spectra of Y122F RnR (identical to the wildtype enzyme)^{22,23} possess a broad absorption maximum at 28,000 cm⁻¹, and exhibits a resonance enhanced $\nu_s(\text{Fe-O-Fe})$ mode at 500 cm⁻¹ (with excitation at 24,200 cm⁻¹ (413 nm)) that increases in resonance enhanced intensity with laser excitation from 20491 cm⁻¹ (488 nm) to 28,089 cm⁻¹ (356 nm), assigning the transitions in this intense high energy region as μ -oxo to iron LMCT.²⁴ The Y122F RnR absorption spectrum was thus calculated with TD-DFT (Figure S14 bottom) using the structure in Figure S15, and the μ -oxo π to iron $d\pi^*$ LMCTs were identified and compared to the experimental assignment. To assign transitions in the TD-DFT spectrum, natural transition orbitals²⁵ (NTOs) were calculated for all prominent transitions predicted between 26,000 and 34,000 cm⁻¹, which minimized the number of transition components in each transition and simplified their general assignment. The NTOs show that the transitions calculated to be between 30,500 and 31,000 cm⁻¹ are μ -oxo π to $d\pi^*$ LMCT in character (Figure S14 and Tables S2 and S3), and are calculated to be higher in energy by 3,000 cm⁻¹ relative to experiment. Therefore, all further TD-DFT calculated spectra have been shifted down in energy by 3,000 cm⁻¹ to account for this calibration (Figure S14 bottom, blue arrow).

The TD-DFT calculated Q absorption spectrum of the **bis(μ O)-H₂O-6** model which is representative for the bis(μ O), bis(μ O)-OH, and bis(μ O)-H₂O subclasses is shown in Figure 5B (see Figure S16 for TD-DFT calculated spectra of additional models). The calculated absorption spectrum can be divided into three regions: first, a region of weak intensity ($\epsilon \sim 1,000 \text{ M}^{-1}\text{cm}^{-1}$) between 7,800 and 16,000 cm⁻¹ (inset in Figure 5B); second, a region of increased intensity between 16,000 and 23,000 cm⁻¹ with an $\epsilon_{\text{max}} \sim 5,000 \text{ M}^{-1}\text{cm}^{-1}$; and a region between 23,000 and 30,000 cm⁻¹ with high intensity ($\epsilon_{\text{max}} \sim 15,000 \text{ M}^{-1}\text{cm}^{-1}$). The NTOs of the most prominent transitions (sticks in Figure 5B) in these three regions give their general assignments. The region from 7,800 to 16,000 cm⁻¹ is composed of Fe(IV)₂ d-d transitions (inset Figure 5B). In the antiferromagnetically coupled high-spin Fe(IV)₂ site, each iron contains either four α (Fe_{1 α} , left iron Figure S17) or β (Fe_{2 β}) electrons with an α or β dx^2-y^2 LUMO orbital, respectively (Figure S17 for the unoccupied d -orbital manifold for **bis(μ O)-H₂O-6**). Thus, the two lowest energy transitions near 10,000 cm⁻¹ are found to be the Jahn-Teller α and β dz^2 to dx^2-y^2 excitations and would correspond to the 12,500 cm⁻¹ feature in the experimental absorption spectrum (Figure 5A inset). The region between 16,000 and 23,000 cm⁻¹ consists of the lowest energy μ -O LMCT transitions, which are calculated to be μ -O $d\pi \rightarrow dx^2-y^2$ LUMO excitations on both Fe(IV)₂. The relatively low energy of these LMCTs are due to exchange stabilization of the dx^2-y^2 LUMO orbitals in the high-spin Fe(IV)₂ $3d$ manifolds, which lowers the energy of the unoccupied Fe_{1 α} and Fe_{2 β} dx^2-y^2 LUMO orbitals and associated LMCTs. This region would correspond to the rising intensity in the experimental data starting at 15,000 cm⁻¹ and peaking at 22,000 cm⁻¹ in Figure 5A.

The calculated region between 23,000 and 30,000 cm⁻¹ in the model **bis(μ O)-H₂O-6** corresponds to the region probed experimentally by rR spectroscopy and is thus of particular interest. The transitions in this region are calculated to be primarily μ -O $\pi \rightarrow d\pi^*$ LMCTs. The

NTOs of several transitions in this region were calculated. The NTOS of three of these transitions (labeled 1-3 in Figure 5B) are tabulated in Tables S4-S6, respectively. As an example, the NTOs for transition 2 highlighted in Figure 5B are described using Table S5. In the **bis(μ O)-H₂O-6** model, Fe_{2 β} and Fe_{1 α} possess an empty α and β d -orbital manifold, respectively. The calculated NTOs for transition 2 show four major components: two β μ -O $\pi \rightarrow$ Fe_{1 α} $d\pi^*$ components (1st and 4th NTOs, 36% total contribution), as well as two α μ -O $\pi \rightarrow$ Fe_{2 β} $d\pi^*$ components (2nd and 3rd NTOs, 40% total contribution). Note that these contributions involve a ligand donor of one spin to the unoccupied $3d$ orbitals of the same spin on an iron atom possessing valence orbital electrons with the *opposite* spin. Hence, transition 2 is composed of an approximately equal mixture of β and α μ -O π donation to Fe_{1 α} and Fe_{2 β} respectively, and is best described as a μ -O LMCT to both Fe(IV) atoms (transitions 1 and 3 in Figure 5B have equivalent NTO assignments). In principle, LMCT from both (μ -O)₂ to $d\pi^*$ orbitals on both iron atoms would result in an excited state distortion involving elongation along all four Fe-O bonds of the Fe₂O₂ core, and thus propagate along the ν_1 mode (Figure 4 top) leading to its resonance enhancement in the Raman measurement at 351 nm.

In order to determine if the excited state predicted by the NTOs in Table S5 for transition 2 in Figure 5B would result in the resonance enhancement of the ν_1 mode, the linear coupling term (LCT) for this excited state was calculated along the ν_1 (totally symmetric A_g) mode, as well as modes ν_2 and ν_3 (non-symmetric vibrations, Figure 4) as references. For the dominant A-term resonance enhancement of a Raman vibration, the excited state must be distorted along the normal mode of vibration, which from group theory must be totally symmetric. The force leading to this distortion is given by the linear coupling term (LCT) which is the change in total energy (E) of the excited state relative to the ground state with distortion along the normal mode q ; i.e., $\frac{dE}{dq}$. Therefore, the normal mode q enhanced by a particular transition can be determined using TD-DFT by calculating $\frac{dE}{dq}$ for an excited state using small plus minus distortions of the molecular geometry along a set of normal modes q_i ($i = 1, 2, \dots, 3N - 6$), and finding the normal mode for which is $\frac{dE}{dq}$ large. For **bis(μ O)-H₂O-6**, the NTOs for transition 2 suggest resonance enhancement of a normal mode involving Fe-O motions along all four bonds, which would correspond to ν_1 (see Figure 4 top). Modes ν_2 and ν_3 are non-totally symmetric and are therefore expected to exhibit small LCT slopes. Small (< 0.005 Å) distortions (Δq) along the ν_1 , ν_2 , and ν_3 modes were introduced and the energy change of transition 2 was calculated using TD-DFT (Figure 5B right). Only the ν_1 mode exhibits a large negative LCT for transition 2 (red line labeled 2 in Figure 5B right) corresponding to ν_1 (A_g) Fe₂-O₂ elongation (i.e., a decrease in the excited state energy), whereas ν_2 and ν_3 (blue and orange lines in Figure 5B right plot, respectively) show much smaller LCTs ($< 25\%$ of ν_1). The same results are found for transitions 1 and 3 in Figure 5B (Figure S18). Therefore, the totally symmetric breathing mode ν_1 in the bis(μ O)-H₂O (as well as bis(μ O) and bis(μ O)-OH) subclasses is predicted to be resonance-enhanced by a transition involving μ -O $\pi \rightarrow d\pi^*$ on both iron atoms, and would be assigned to the 690 cm⁻¹ peak observed in the rR spectrum.

While the results of the analysis above for the bis(μ O)-L subclasses had been anticipated by earlier studies, a similar TD-DFT analysis is now applied to the novel subclasses of open core Q models. The calculated TD-DFT spectrum for a representative OC -OH/-OH open core model (**OC10**) is provided in Figure 5C (see Figure S19 for TD-DFT calculated spectra of additional

models). Similar to the **bis(μ O)-H₂O-6** TD-DFT spectrum, the **OC10** spectrum divides into three regions. The first region from 9,000 to 16,000 cm⁻¹ (Figure 5C, inset) has several weak transitions ($\epsilon_{\text{max}} \sim 500 \text{ M}^{-1}\text{cm}^{-1}$) and would correspond to the 12,500 cm⁻¹ peak in the experimental data (Figure 5A, inset). The second region has increasing intensity between 16,000 to 24,000 cm⁻¹ ($\epsilon_{\text{max}} \sim 5,000 \text{ M}^{-1}\text{cm}^{-1}$) and would correlate to the local maximum in the experimental data at 23,000 cm⁻¹ (Figure 5A). The third region possesses high intensity between 24,000 and 32,000 cm⁻¹ with a local maximum at 27,000 cm⁻¹ ($\epsilon_{\text{max}} \sim 9,000 \text{ M}^{-1}\text{cm}^{-1}$), which would correlate to the region probed by rR in the experimental data taken at 28,500 cm⁻¹. These regions were again assigned by calculating the NTOs of several dominant transitions in each region and correlating the NTOs to the electronic structure of **OC10** (Figure S20). This model (as well as other OC -OH/-OH models) possesses two high-spin, antiferromagnetically coupled Fe(IV) with four α ($\text{Fe}_{1\alpha}$; right iron in Figure S20) and β ($\text{Fe}_{2\beta}$) valence electrons, with an α and β dx^2-y^2 LUMO, respectively (note that in this model, Fe_2 and Fe_1 contain the in-plane (Fe-O-Fe plane) and out-of-plane Fe-OH bonds, respectively).

The first region from 9,000 to 16,000 cm⁻¹ in the **OC10** TD-DFT calculated spectrum (correlating to the experimental 12,500 cm⁻¹ peak) again contains $d-d$ transitions; the Jahn-Teller α and β $dz^2 \rightarrow dx^2-y^2$ LUMO transitions are highlighted with arrows (Figure 5C, inset). The second region between 16,000 to 24,000 cm⁻¹ (correlating to the experimental maximum at 23,000 cm⁻¹) contains the lowest energy LMCTs. These are composed of OH⁻ and μ -O π LMCT to the dx^2-y^2 LUMO orbitals on each Fe(IV). The third region from 24,000 to 32,000 cm⁻¹ (correlating to the 28,500 cm⁻¹ rR excitation) is comprised of OH⁻ and μ -O π LMCTs to primarily the in-plane Fe_2 -OH iron $d\pi^*$ orbitals, which show greater intensity than the analogous LMCT to Fe_1 due to enhanced delocalization of the Fe_2 $d\pi^*$ orbitals onto the μ -O ligand (23% μ -O character in Fe_2 $d\pi^*$ orbitals, vs. 7% in Fe_1 ; Table S7. Note that the OH⁻ character is roughly the same in both Fe $d\pi^*$ manifolds). The NTOs of two representative intense transitions (labeled 1 and 2 in Figure 5C) are shown in Tables S8 and S9, respectively. NTOs for the most prominent transition (1) contain two dominant contributions. The first NTO (40% contribution) contains a donor orbital comprised of α OH⁻ and μ -O π character, paired with an acceptor $\text{Fe}_{2\beta}$ dyz orbital (coordinate of each Fe(IV) in Figure S20) strongly antibonding with its OH⁻ π orbital. The second NTO (20% contribution) possesses some α OH⁻ and μ -O π donor character (mixed with carboxylate), with an acceptor $\text{Fe}_{2\beta}$ dxy orbital antibonding with the μ -O π donor. Thus, this transition mostly involves a OH⁻ and μ -O $\pi \rightarrow \text{Fe}_2$ $d\pi^*$ excitation, with larger contributions from the OH⁻ donor than μ -O due to the 40% (and majority) NTO possessing a $\text{Fe}_{2\beta}$ dyz orbital strongly antibonding with the OH⁻ π donor. (Transition 2 in Table S9 has a similar NTO assignment, but includes some $d\sigma^*$ contribution). An excitation with strong OH⁻ π (and weaker μ -O π) character, involving the in-plane OH⁻ ligand to its coordinated Fe_2 (IV) site, would result in an excited state distortion involving elongation of the Fe_2 -OH and Fe_2 -(μ -O) bonds and would provide a symmetric distortion about Fe_2 .

In comparison to the normal modes of OC -OH-OH models defined in Section 3.2, the transition 1 excited state (as well as 2) involves an elongation of both the Fe_2 -OH and Fe_2 -(μ -O) bonds and would propagate along the ν_1 mode, which is the in-phase combination of the $\nu(\text{Fe}_2\text{-OH})$ and $\nu_{\text{as}}(\text{Fe-O-Fe})$ modes (Figure 4, middle) found near 690 cm⁻¹, which could lead to its resonance enhancement in the Raman measurement. Two other modes involve Fe-O distortions about Fe_2 : ν_2 , which is the out of phase combination of the $\nu(\text{Fe}_2\text{-OH})$ and $\nu_{\text{as}}(\text{Fe-O-Fe})$ modes; and ν_4 , which is $\nu_{\text{s}}(\text{Fe-O-Fe})$. To determine the normal mode(s) of vibration that would give the

excited state distortion and thus rR enhancement for transition 1, the LCT slopes were calculated for transition 1 along modes ν_1 , ν_2 , and ν_4 (as described above). The TD-DFT energy of transition 1 was calculated using plus/minus distortions structures along these modes, and referenced to the ground state energy. Only the ν_1 mode results in a large and negative LCT slope (red line, Figure 5C right), inducing elongation of both the Fe₂-OH and Fe₂-(μ -O) (antisymmetric μ -O) bonds; the LCT slopes for the ν_2 (blue line, Figure 5C right) and ν_4 (orange line, Figure 5C right) modes are negligibly small (1% of the ν_1 LCT slope). Similar results were found for transition 2 (Figure S21). Though one might anticipate that the symmetric ν_4 ($\nu_s(\text{Fe-O-Fe})$) mode would result in a negative LCT slope for transition 1, the *localized* nature of the Fe₂ $d\pi^*$ acceptor orbital that is antibonding to OH⁻ results in a preferential excited state elongation of both the Fe₂-OH and Fe₂-(μ -O) bonds which projects dominantly on ν_1 . Thus, for OC -OH/-OH models, the transitions in the region between 24,000 and 32,000 cm⁻¹ correspond to OH⁻ and μ -O $\pi \rightarrow \text{Fe}_2 d\pi^*$ excitations localized on the in-plane Fe₂-OH moiety, which results in resonance enhancement of the ν_1 Raman mode (at ~ 700 cm⁻¹) with 351 nm excitation.

The calculated TD-DFT spectrum for OC -OH/=O models also exhibits three regions of intensity, and a representative spectrum using model **OC26** is shown in Figure 5D (see Figure S22 for TD-DFT calculated spectra of additional models). These three regions include weak features ($\epsilon_{\text{max}} = 500 \text{ M}^{-1}\text{cm}^{-1}$) between 9,000 and 15,000 cm⁻¹ (inset Figure 5D), moderately intense features ($\epsilon_{\text{max}} = 4,700 \text{ M}^{-1}\text{cm}^{-1}$) between 16,000 and 24,000 cm⁻¹ with rising intensity, and intense features between 24,800 and 29,000 cm⁻¹ with a local maximum at 27,000 cm⁻¹ ($\epsilon_{\text{max}} = 10,000 \text{ M}^{-1}\text{cm}^{-1}$). These three regions were again assigned based on the NTOs for several representative intense transitions in each region (molecular orbital diagram of **OC26** given in Figure S23). **OC26** possesses a high-spin, antiferromagnetically coupled Fe(IV)₂ site; Fe₂ (with the OH⁻ ligand in Figure S23) possesses four β electrons with a βdx^2-y^2 LUMO (Fe_{2 β}), and Fe₁ (with the terminal oxo) possesses four α electrons with an αdx^2-y^2 LUMO (Fe_{1 α}). The first region in the TD-DFT calculated spectrum for OC26 from 9,000 to 15,000 cm⁻¹ contains the α and $\beta d-d$ transitions on Fe_{1 α} and Fe_{2 β} , respectively; the Jahn-Teller dz^2 to dx^2-y^2 LUMO transitions are highlighted with arrows in Figure 5D inset. This region would again correspond to the 800 nm peak in the Q experimental absorption spectrum (Figure 5A inset). The second region from 16,000 to 24,000 cm⁻¹ contains the lowest energy LMCTs, consisting of OH⁻ π and μ -O π excitation into the Fe_{2 β} dx^2-y^2 LUMO as well as μ -O π donation into the Fe_{1 α} dx^2-y^2 LUMO. (Transitions involving terminal oxo π donation into the Fe_{1 α} dx^2-y^2 LUMO were also predicted in this region, albeit with small intensity.) The shoulder in this region at 23,500 cm⁻¹ would correspond to the local maximum in the experimental spectrum at 23,000 cm⁻¹ (Figure 5A).

The third region from 24,800 to 29,000 cm⁻¹ contains four prominent transitions: transitions labeled 1-3, as well as a carboxylate to Fe₂ $d\pi^*$ (Figure 5D labeled COO⁻) transition. Transitions 1-3 possess similar NTO contributions (Tables S10-S12, respectively) and are equivalently assigned. Transition 1 contains two major NTO components. The first component (56% contribution) contains a mixture of μ -O and OH⁻ π donor character into the Fe_{2 β} $dxy \pi^*$ acceptor orbital that is antibonding with both the μ -O and OH⁻ π orbitals. The second component (30% contribution) has a similar donor character, with a CT acceptor Fe_{2 β} dxz orbital that is antibonding with the OH⁻ π donor orbital. Hence, transition 1 (and 2 & 3) involves a OH⁻ and μ -O $\pi \rightarrow \text{Fe}_2 d\pi^*$ excitation, similar to the results found for the OC -OH/-OH class, *vide supra*. (Terminal oxo $\pi \rightarrow \text{Fe}_1 d\pi^*$ transitions are calculated to be at energies above 31,000 cm⁻¹ and

are thus excluded from further analysis). Note that transitions 1-3 involve the Fe₂ which has the OH⁻ ligand and also a short Fe₂-(μ-O) bond, that results from a weaker Fe₁-(μ-O) bonding interaction due to the terminal oxo ligand on Fe₁. Thus, the OH⁻ and μ-O π → Fe₂ dπ* transition would result in an excited state with elongations localized along the Fe₂-OH and Fe₂-(μ-O) bonds, and hence result in a symmetric distortion about Fe₂.

For transitions 1-3 in the OC -OH/=O models, this excited state distortion of localized elongations of the Fe₂-OH and Fe₂-(μ-O) bonds would propagate along normal mode ν₂ (Figure 4, bottom). However, the ν₃ (out of phase version of ν₂) mode also contains motion along the Fe₂-OH and Fe₂-(μ-O) bonds and could potentially show rR enhancement. To confirm the normal mode(s) along which the excited state distorts in transitions 1-3, their LCT slopes (transition 1 Figure 5D right, transitions 2-3 Figure S24) were calculated along normal modes ν₂, ν₃, as well as ν₄ (from Figure 4 bottom, the ν_s(Fe-O-Fe) mode, that contains mostly Fe₁-(μ-O) motion and is therefore included as a reference). All three transitions only show a large and negative LCT slope for distortion along the ν₂ mode leading to both Fe₂-OH and Fe₂-(μ-O) elongations, that decrease the energy of the excited state relative to its energy in the ground state geometry. Thus, for the OC -OH/=O subclass, the OH⁻ and μ-O π → Fe₂ dπ* LMCT near 28,500 cm⁻¹ results in a local distortion of the Fe₂-(μ-O) (and Fe₂-OH) bonds, which involves the ν₂ mode at ~ 700 cm⁻¹ leading to its enhancement in the rR experiment.

In summary, these TD-DFT calculations predict three regions of absorption intensity in both open and closed core Q models. The low energy region (~ 9,000 cm⁻¹ to ~ 15,000 cm⁻¹) in all models is predicted to exhibit *d-d* transitions of the high-spin Fe(IV) centers, corresponding to the experimental Q absorption peak at 12,500 cm⁻¹. All models predict rising intensity between ~ 15,000 and ~ 24,000 cm⁻¹ corresponding to the lowest energy OH⁻ (open cores) and μ-O (open and closed cores) LMCT involving Fe(IV) dx²-y² LUMO acceptor orbitals (Fe₂ for the open cores), which would correlate to the 23,000 cm⁻¹ peak in the absorption spectrum. These LMCTs reflect the exchange stabilization of the dx²-y² LUMO orbitals, which lowers their energies and thus those of the corresponding LMCT transitions. The third region between ~ 24,000 and ~ 32,000 cm⁻¹ contains OH⁻ (for open cores) and μ-O LMCT into the Fe(IV) dπ* manifold (Fe₂ for open cores). Both open and closed core Q models are predicted to exhibit a 690 cm⁻¹ mode in the Raman spectrum which would be resonance-enhanced by excitation at 28,500 cm⁻¹. For bis(μO)-L closed core subclasses, TD-DFT calculations predict a (μ-O)₂ π to dπ* LMCT to both Fe(IV) atoms at 351 nm, which would result in the resonance enhancement of the totally symmetric ν₁ mode (Figure 4 top). In the OC -OH/-OH subclass, OH⁻ & μ-O π → Fe₂ dπ* transitions involving acceptor orbitals strongly antibonding to the in-plane OH⁻ are predicted to enhance the ν₁ mode localized on the in-plane Fe₂-OH unit (the symmetric combination of the ν(Fe₂-OH) and ν_{as}(Fe-O-Fe) in Figure 4 middle). Finally, in the OC -OH/=O subclass, the OH⁻ & μ-O π → Fe dπ* transitions on the Fe₂-OH iron would result in the resonance enhancement of the ν₂ mode (Figure 4 bottom). This mode contains the symmetric combination of the ν(Fe₂-OH) and ν_{as}(Fe-O-Fe) vibrations which localize on Fe₂ due to the short Fe₂-(μ-O) bond and is also predicted to contribute at ~ 700 cm⁻¹.

Figure S14 Calibration of TD-DFT methodology. Top: absorption spectrum of Y122F RnR, with a dotted line indicating the ϵ_{\max} for the $\mu\text{-O}$ to $d\pi$ transition based on rR. Bottom: TD-DFT calculated absorption spectrum for Y122F using the CAM-B3LYP functional. NTOs for the $\mu\text{-O}$ to $d\pi$ transitions 1 and 2 are given in Tables S2 and S3, respectively. Blue arrow indicates an energy difference of $3,000\text{ cm}^{-1}$ in the calculated spectrum relative to experiment.

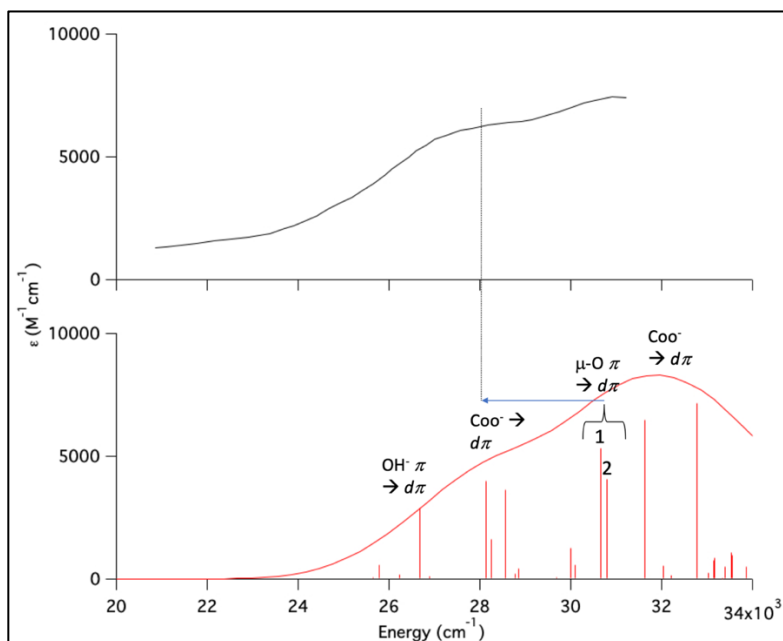


Figure S15 Y122F RnR model used for TD-DFT calibration (based on crystallography and NRVS to define the OH_x ligands). For the TD-DFT calculations, H-bonding residues to the two histidine ligands were removed, and all first-sphere residues were truncated to a single methyl group off the side chain.

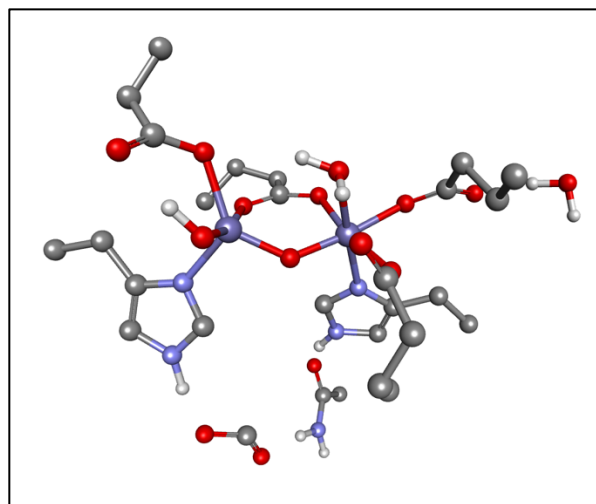


Table S2 NTOs for transition 1 in Y122F RnR in Figure S14.

Transition and contribution %	Donor NTO	Acceptor NTO
$\mu\text{-O } \pi \rightarrow \text{Fe } d\pi^*$ 54%		
$\text{OH}^- \pi \rightarrow \text{Fe } d\pi^*$ 20%		
$\mu\text{-O } \pi \rightarrow \text{Fe } d\pi^*$ 12%		
$\mu\text{-O } \pi \rightarrow \text{Fe } d\pi^*$ 7%		

Table S3 NTOs for transition 2 in Y122F RnR in Figure S14.

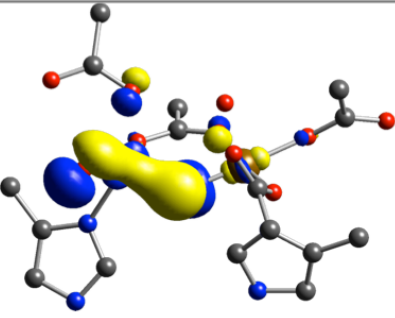
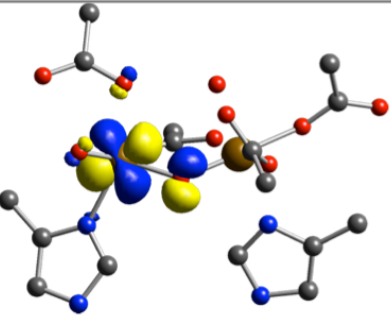
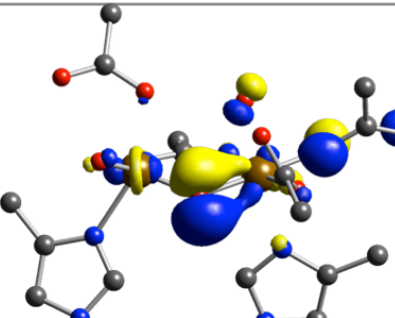
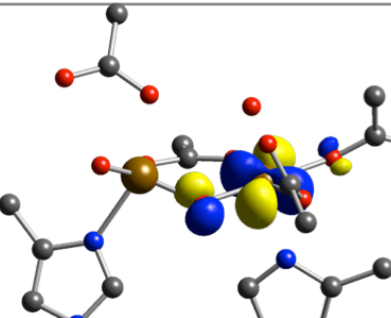
Transition and contribution %	Donor NTO	Acceptor NTO
$\mu\text{-O}\pi \rightarrow \text{Fe}d\pi^*$ 60%		
$\mu\text{-O}\pi \rightarrow \text{Fe}d\pi^*$ 22%		

Figure S16 TD-DFT calculated absorption spectra for select bis(μ O), bis(μ O)-OH, and bis(μ O)-H₂O models.

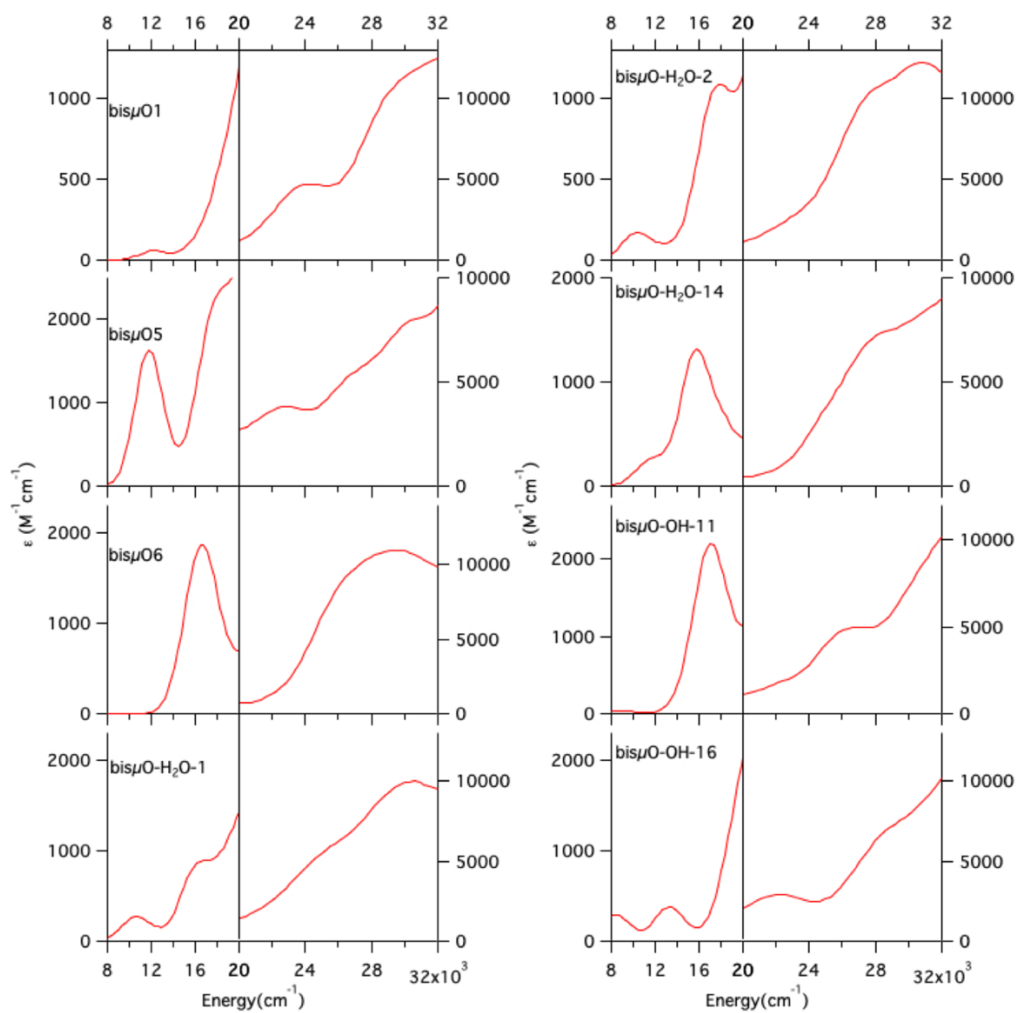


Figure S17 Molecular orbital energy level diagram for the unoccupied d-orbital manifold of **bis(μ O)-H2O-6** calculated with the CAM-B3LYP functional. Fe₂ on left has four β electrons and Fe₁ on right has four α electrons. Coordinate system for each iron atom provided in the structure at the top.

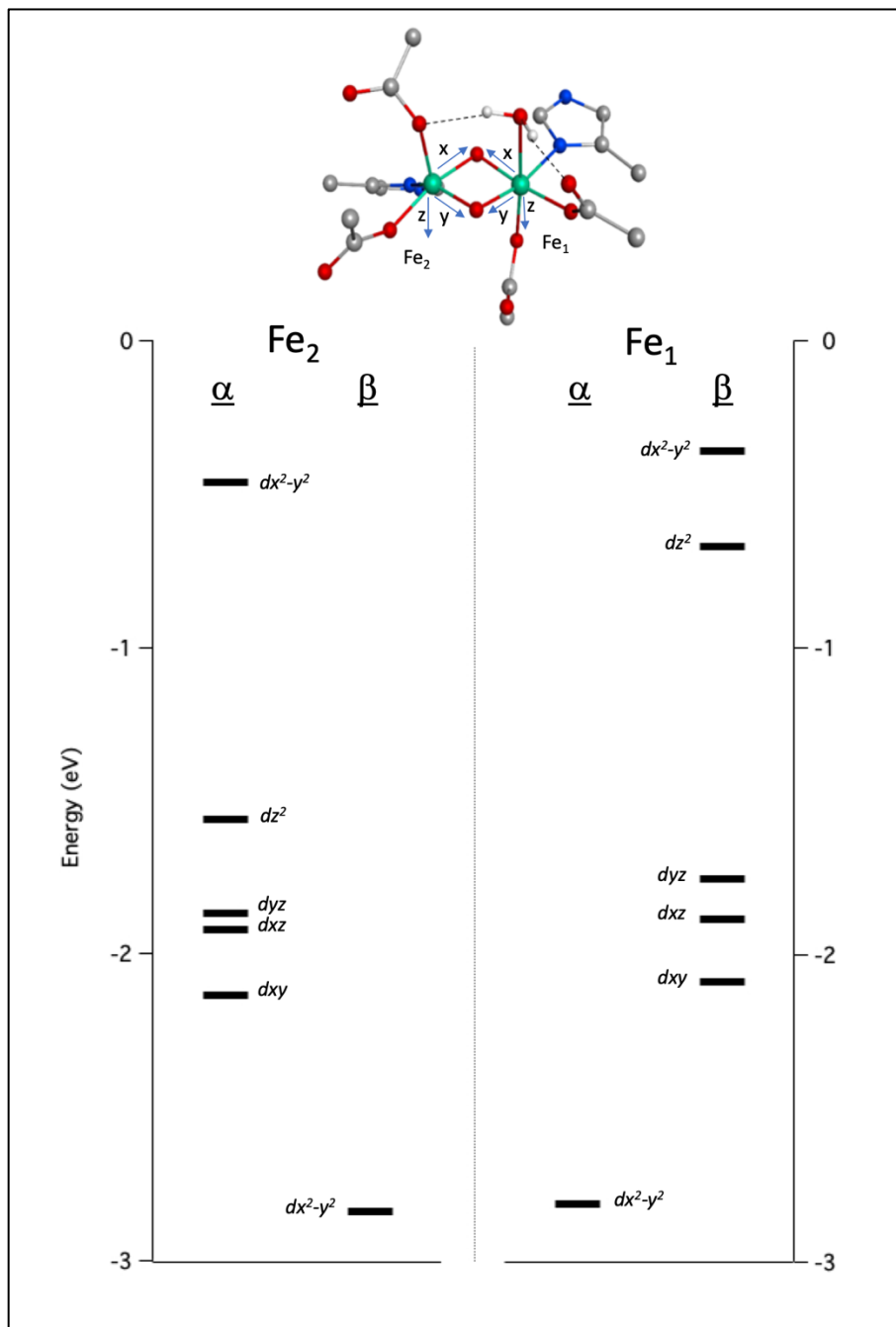


Table S4 NTOs for transition 1 in **bis(μ O)-H2O-6** indicated in Figure 5B. Note that these diagrams have been rotated 120° relative to the structure provided in Figure 5B.

Transition and contribution %	Donor NTO	Acceptor NTO
α $\mu\text{-O}\pi \rightarrow \text{Fe}_2 d\pi^*$ 40%		
β $\mu\text{-O}\pi \rightarrow \text{Fe}_1 d\pi^*$ 24%		
α $\text{Coo}^- \rightarrow \text{Fe}_2 d\pi^*$ 18%		

Table S5 NTOs for transition 2 in **bis(μ O)-H2O-6** indicated in Figure 5B. Note that these diagrams have been rotated 120° relative to the structure provided in Figure 5B.

Transition and contribution %	Donor NTO	Acceptor NTO
$\beta \mu\text{-O}\pi \rightarrow \text{Fe}_1 d\pi^*$ 26%		
$\alpha \mu\text{-O}\pi \rightarrow \text{Fe}_2 d\pi^*$ 20%		
$\alpha \mu\text{-O}\pi \rightarrow \text{Fe}_2 d\pi^*$ 20%		
$\beta \mu\text{-O}\pi \rightarrow \text{Fe}_1 d\pi^*$ 10%		

Table S6 NTOs for transition 3 in **bis(μ O)-H2O-6** indicated in Figure 5B. Note that these diagrams have been rotated 120° relative to the structure provided in Figure 5B.

Transition and contribution %	Donor NTO	Acceptor NTO
$\alpha \mu\text{-O}\pi \rightarrow \text{Fe}_2 d\pi^*$ 40%		
$\alpha \mu\text{-O}\pi \rightarrow \text{Fe}_2 d\sigma^*$ 20%		
$\beta \mu\text{-O}\pi \rightarrow \text{Fe}_1 d\pi^*$ 12%		
$\beta \mu\text{-O}\pi \rightarrow \text{Fe}_1 d\sigma^*$ 12%		
$\beta \mu\text{-O}\pi \rightarrow \text{Fe}_1 d\pi^*$ 9%		

Figure S18 Linear coupling terms for transitions 1 (left) and 3 (right) in **bis(μ O)-H₂O-6** in Figure 5B, calculated using modes v_1 , v_2 , and v_3 from Figure 4 (top).

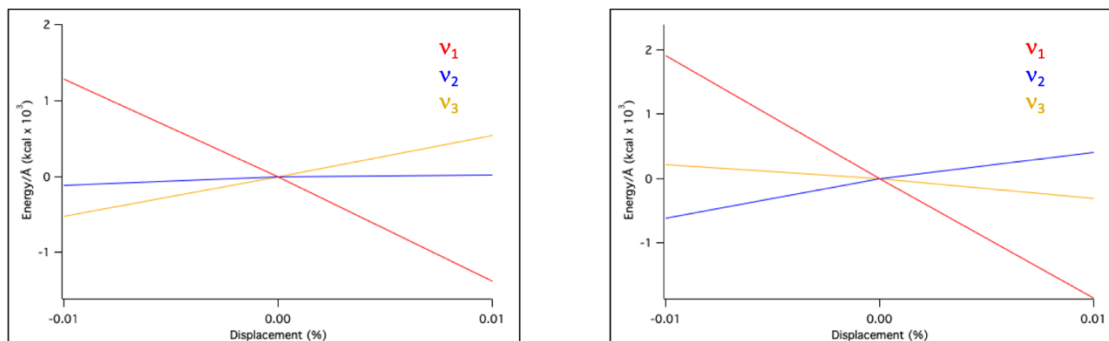


Figure S19 TD-DFT calculated absorption spectra for select OC -OH/-OH models possessing a $\nu(\text{Fe}_2\text{-OH}) + \nu_{\text{as}}(\text{Fe-O-Fe})$ (ν_1 Figure 4 middle) mode near 690 cm^{-1} with an appropriate $^{16}\text{O}^{18}\text{O}$ mixed isotope shift.

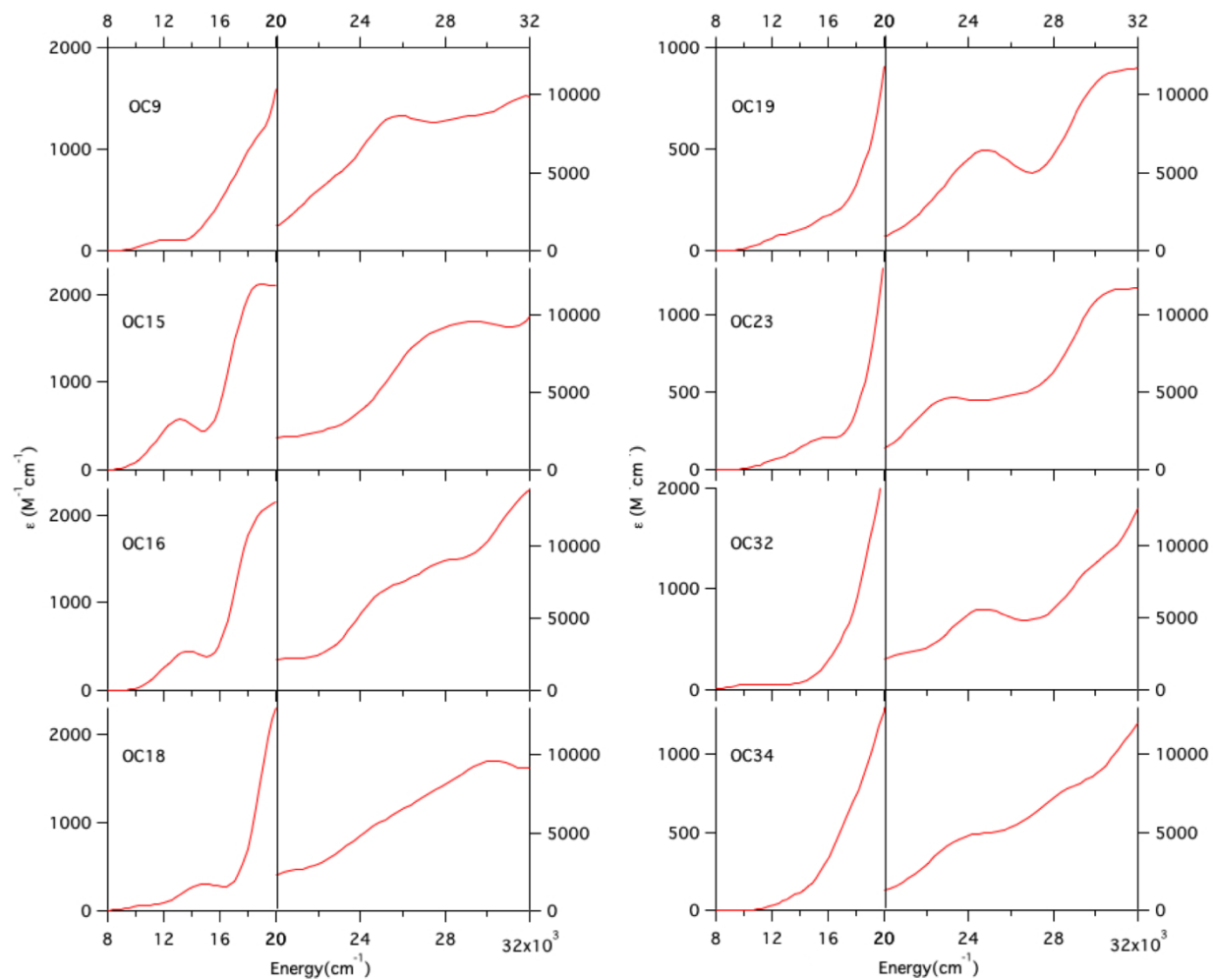


Figure S20 Molecular orbital diagram for the unoccupied d-orbital manifold of **OC10** calculated with the CAM-B3LYP functional. Fe₂ on left has four β electrons and Fe₁ on right has four α electrons. Coordinate system for each iron atom provided in the structure at the top.

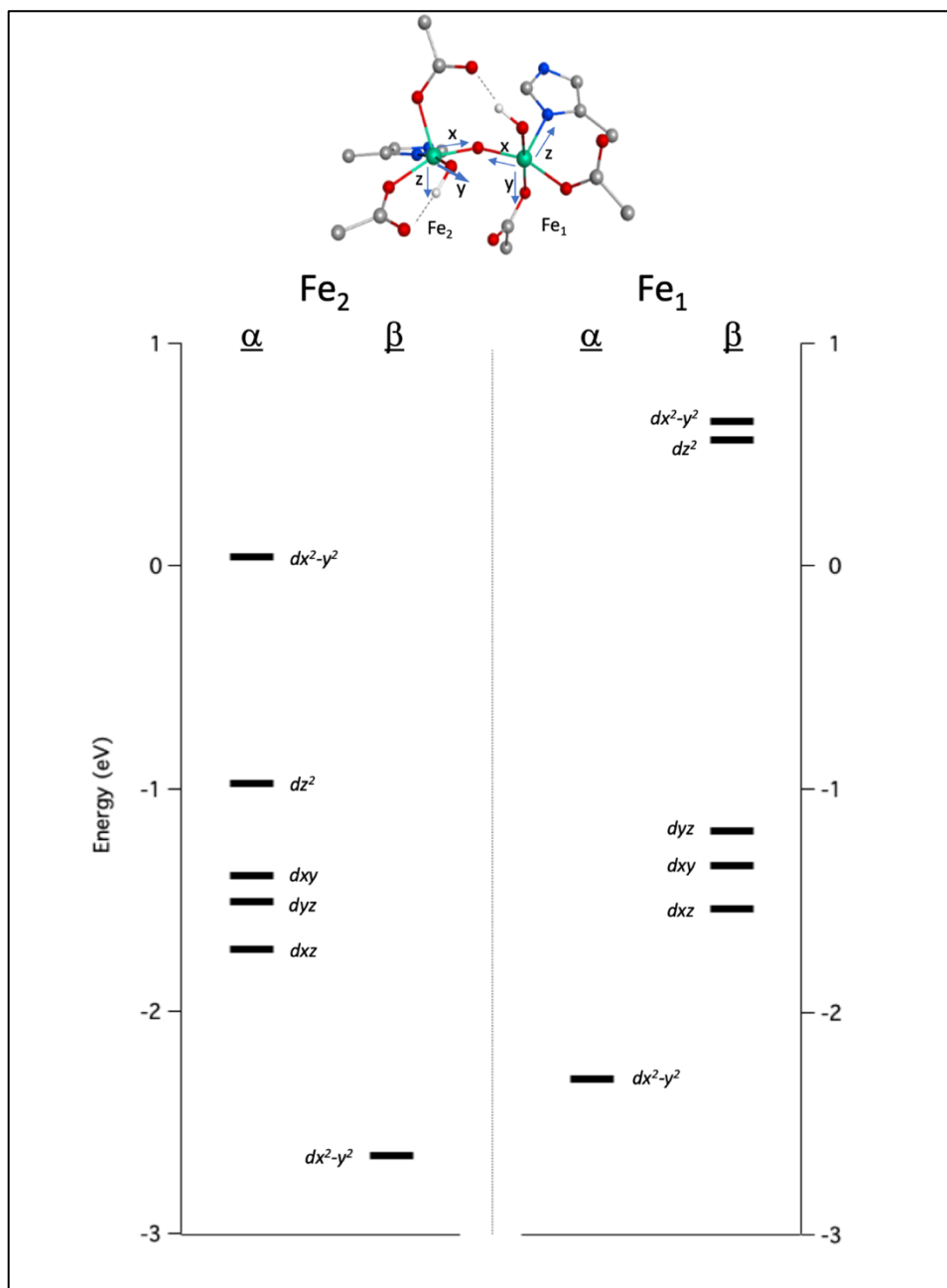


Table S7 OH⁻ and μ-O contributions to the Fe₂ and Fe₁ dπ* manifolds in **OC10**. OH_{IP} and OH_{OOP} indicate in-plane and out-of-plane OH⁻ ligands, respectively. Note that though Fe₁ dπ* orbitals contain slightly larger OH⁻ character (~ 28% vs. 23%), they contain much less μ-oxo character (~ 7% vs. 23%) than the Fe₂ dπ* orbitals.

Fe ₂ Orbital	OH _{IP} character (%)	μ-Oxo character (%)	Fe ₁ Orbital	OH _{OOP} character (%)	μ-Oxo character (%)
Fe ₂ <i>dxy</i>	3.43	13.64	Fe ₁ <i>dxy</i>	2.68	3.34
Fe ₂ <i>dxz</i>	0.51	9.12	Fe ₁ <i>dxz</i>	25.02	0.77
Fe ₂ <i>dyz</i>	20.11	0.26	Fe ₁ <i>dyz</i>	0.81	3.98

Table S8 NTOs for transition 1 in **OC10** indicated in Figure 5C. Note that these diagrams have been rotated 120° relative to the structure provided in Figure 5C.

Transition and contribution %	Donor NTO	Acceptor NTO
α OH ⁻ π → Fe ₂ dπ* 40%		
α OH ⁻ π, μ-O π & Coo ⁻ → Fe ₂ dπ* 20%		
β His → Fe ₁ dπ* 12%		

Table S9 NTOs for transition 2 in **OC10** indicated in Figure 5C. Note that the bottom NTO contribution contains the Fe₂ $d\sigma^*$ (non-LUMO) orbital, which overlaps well with the strong OH⁻ donor orbital. These diagrams have been rotated 120° relative to the structure provided in Figure 5C.

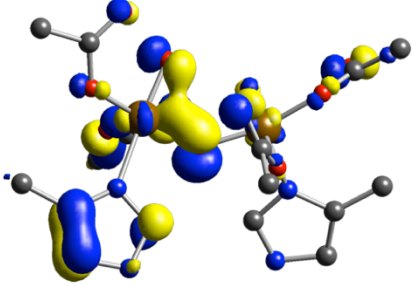
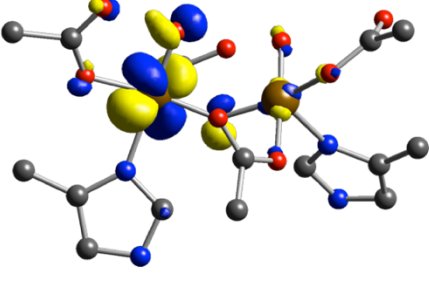
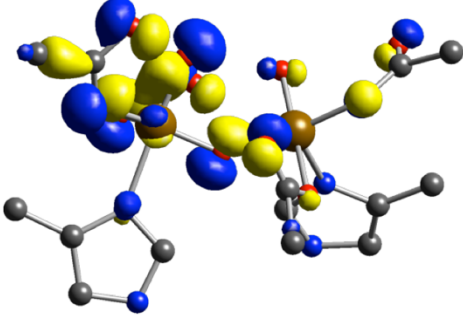
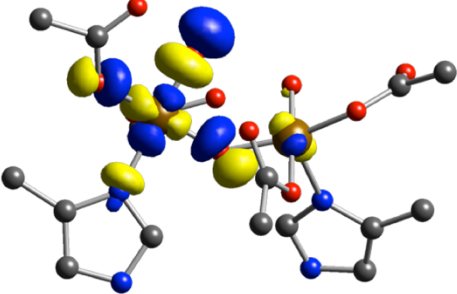
Transition and contribution %	Donor NTO	Acceptor NTO
α OH ⁻ & μ -O $\pi \rightarrow \text{Fe}_2 d\pi^*$ 44%		
α OH ⁻ & μ -O $\pi \rightarrow \text{Fe}_2 d\sigma^*$ 20%		

Figure S21 Linear coupling terms for transition 2 in **OC10** in Figure 5B, calculated using modes v_1 , v_2 , and v_4 from Figure 4 (middle).

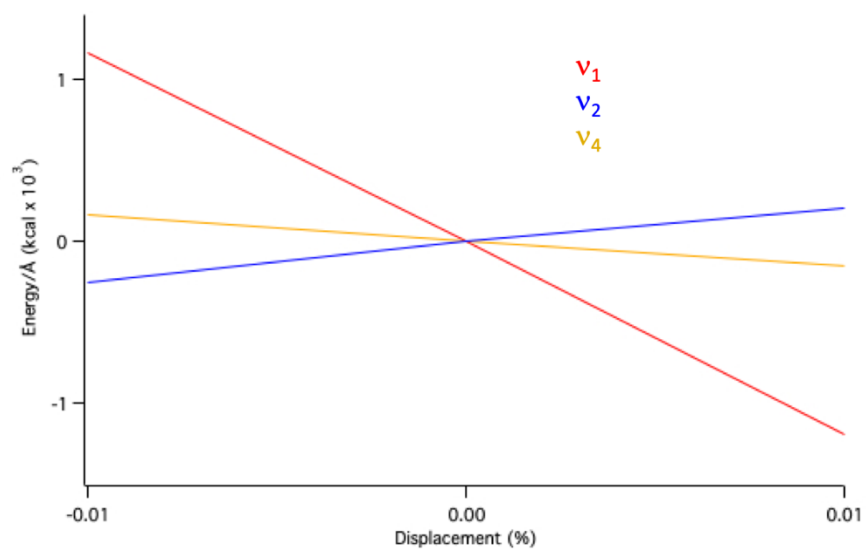


Figure S22 TD-DFT calculated absorption spectra for select OC -OH/=O models possessing a $\nu(\text{Fe}_2\text{-OH}) + \nu_{\text{as}}(\text{Fe-O-Fe})$ (ν_2 Figure 4 bottom) mode near 690 cm^{-1} with an appropriate $^{16}\text{O}^{18}\text{O}$ mixed isotope shift.

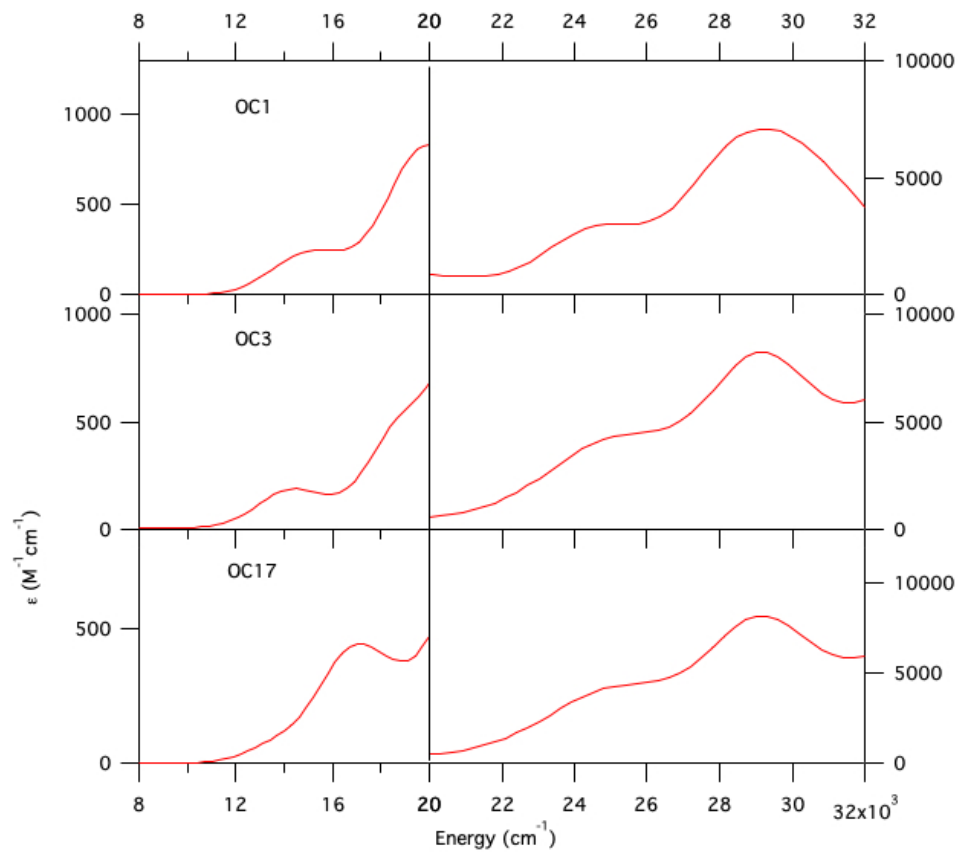


Figure S23 Molecular orbital diagram for the unoccupied d-orbital manifold of **OC26** calculated with the CAM-B3LYP functional. Fe₂ on left has four β electrons and Fe₁ on right has four α electrons. Coordinate system for each iron atom provided in the structure at the top.

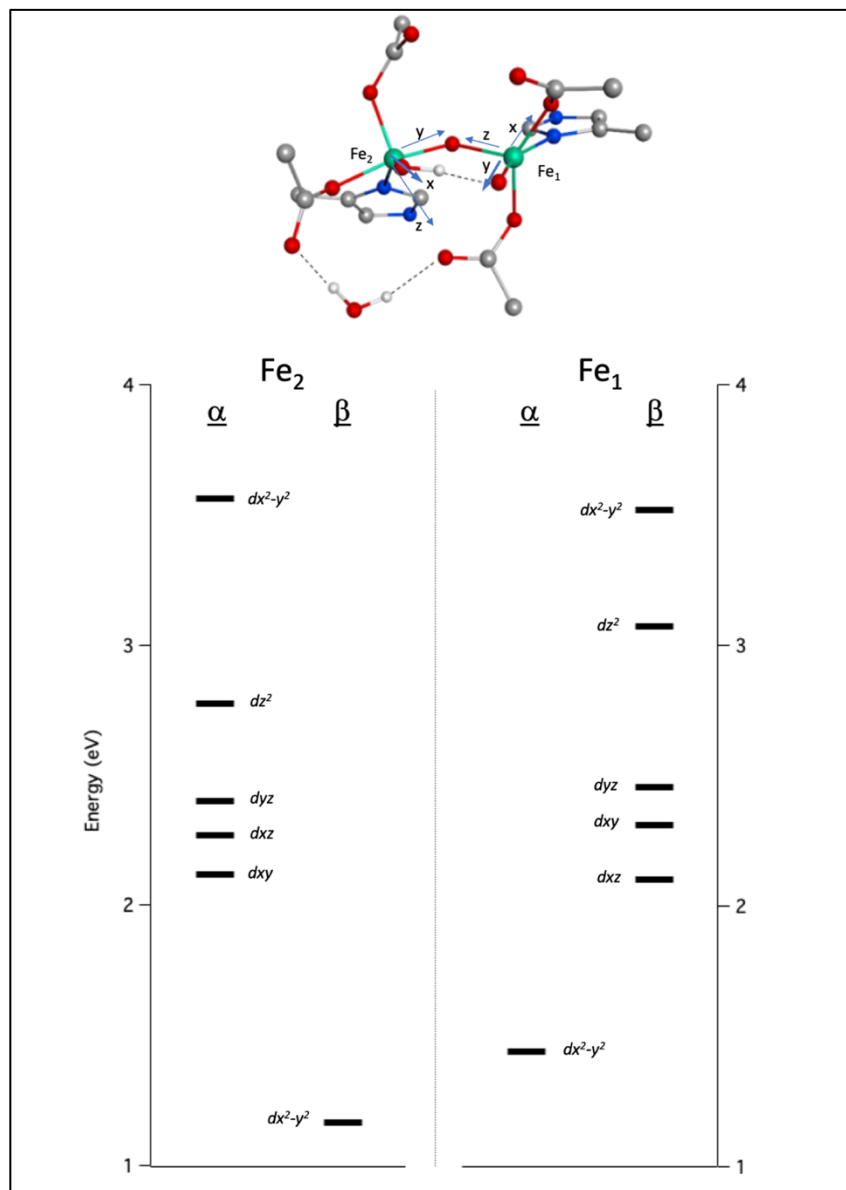


Table S10 NTOs for transition 1 in **OC26** indicated in Figure 5D. Note that these diagrams have been rotated 120° relative to the structure provided in Figure 5D.

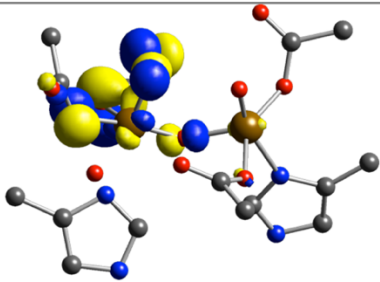
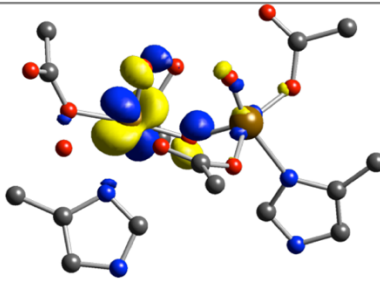
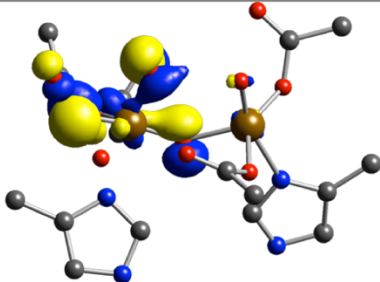
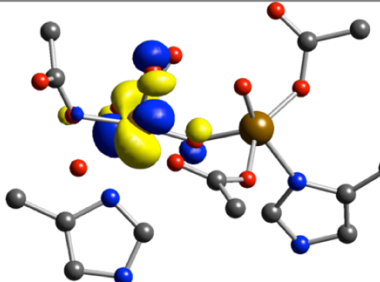
Transition and contribution %	Donor NTO	Acceptor NTO
α OH ⁻ & μ -O $\pi \rightarrow \text{Fe}_2 d\pi^*$ 56%		
α OH ⁻ & μ -O $\pi \rightarrow \text{Fe}_2 d\pi^*$ 30%		

Table S11 NTOs for transition 2 in **OC26** indicated in Figure 5D. Note that these diagrams have been rotated 120° relative to the structure provided in Figure 5D.

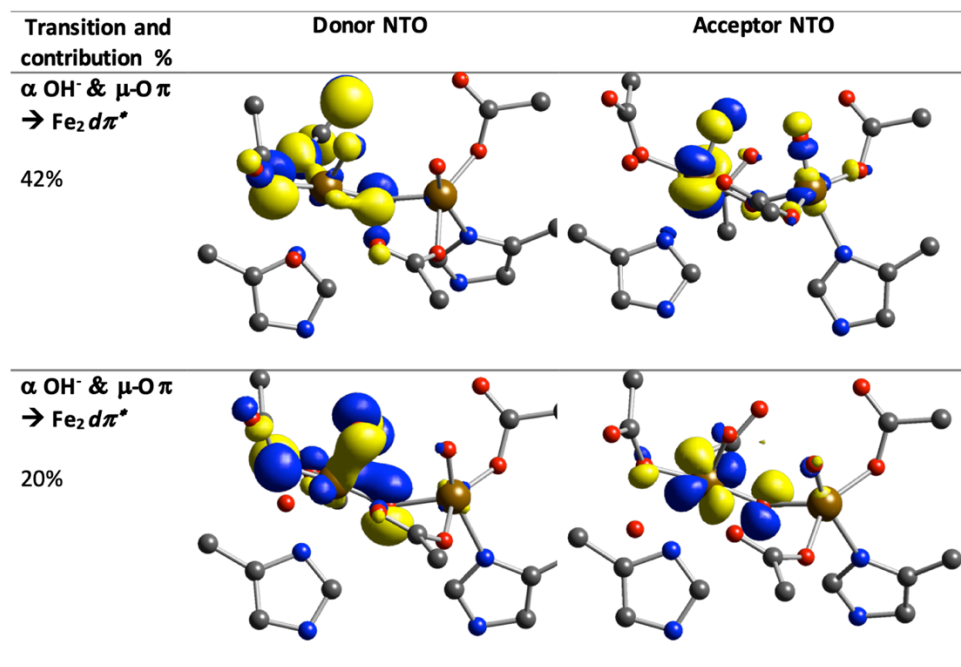


Table S12 NTOs for transition 3 in **OC26** indicated in Figure 5D. Note that these diagrams have been rotated 120° relative to the structure provided in Figure 5D.

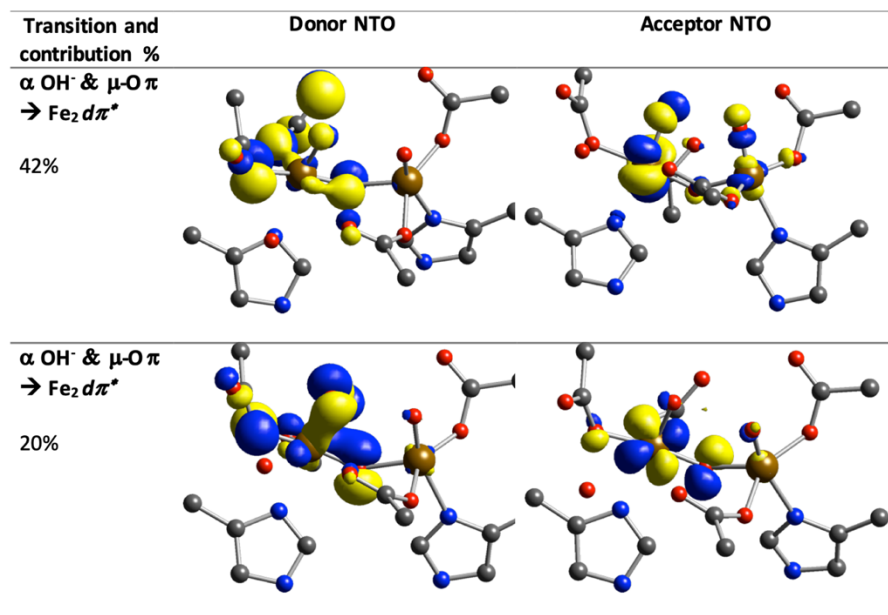


Figure S24 Linear coupling terms for transitions 2 (left) and 3 (right) in **OC26** in Figure 5D, calculated using modes v_2 , v_3 , and v_4 from Figure 4 (bottom).

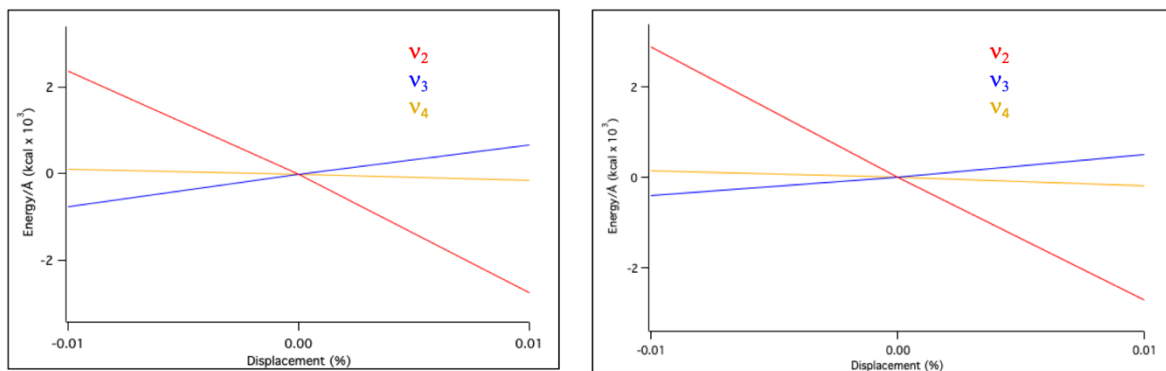


Figure S25 NRVS spectra for selected open core (left) and closed core (right) models simulated using BP86 + 10% HF (red) and B3LYP (black) functionals, using the 6-31g(d) basis set

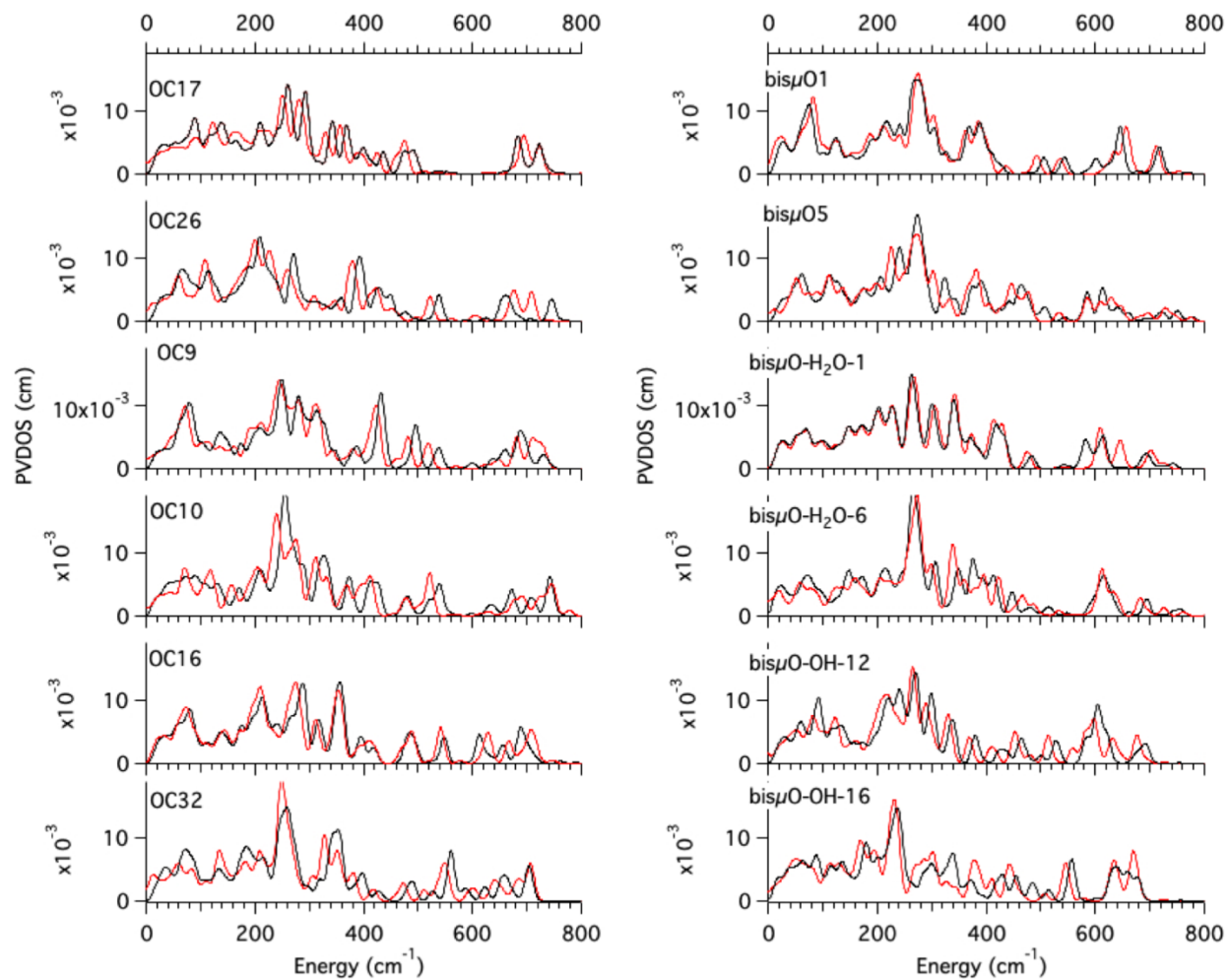


Figure S26 DFT-calculated cryoreduced NRVS spectra of **OC16**. Arrows indicate major changes between spectra. (A) Top: Experimental Early Q – MMOH_{red} (red spectrum) and Late Q-MMOH_{red} (black spectrum) NRVS data. Middle: NRVS spectra for the B3LYP optimized **OC16** model (red) and its Fe₂(III)Fe₁(IV) optimized congener (black). Bottom: NRVS spectra for the B3LYP optimized **OC16** model (red) and its Fe(III)₂ optimized congener (black). (B) Top: Late Q-MMOH_{red} NRVS spectrum. Middle: NRVS spectra of **OC16** Fe₂(III)Fe₁(IV) (black) and its ¹⁸O₂ isotopomer (blue). Bottom: NRVS spectra of **OC16** Fe₂(III)Fe₁(III) (black) and its ¹⁸O₂ isotopomer (blue). (C) Optimized structures of cryoreduced **OC16** Fe₂(III)Fe₁(IV) (left) and **OC16** Fe₂(III)Fe₁(III) (right).

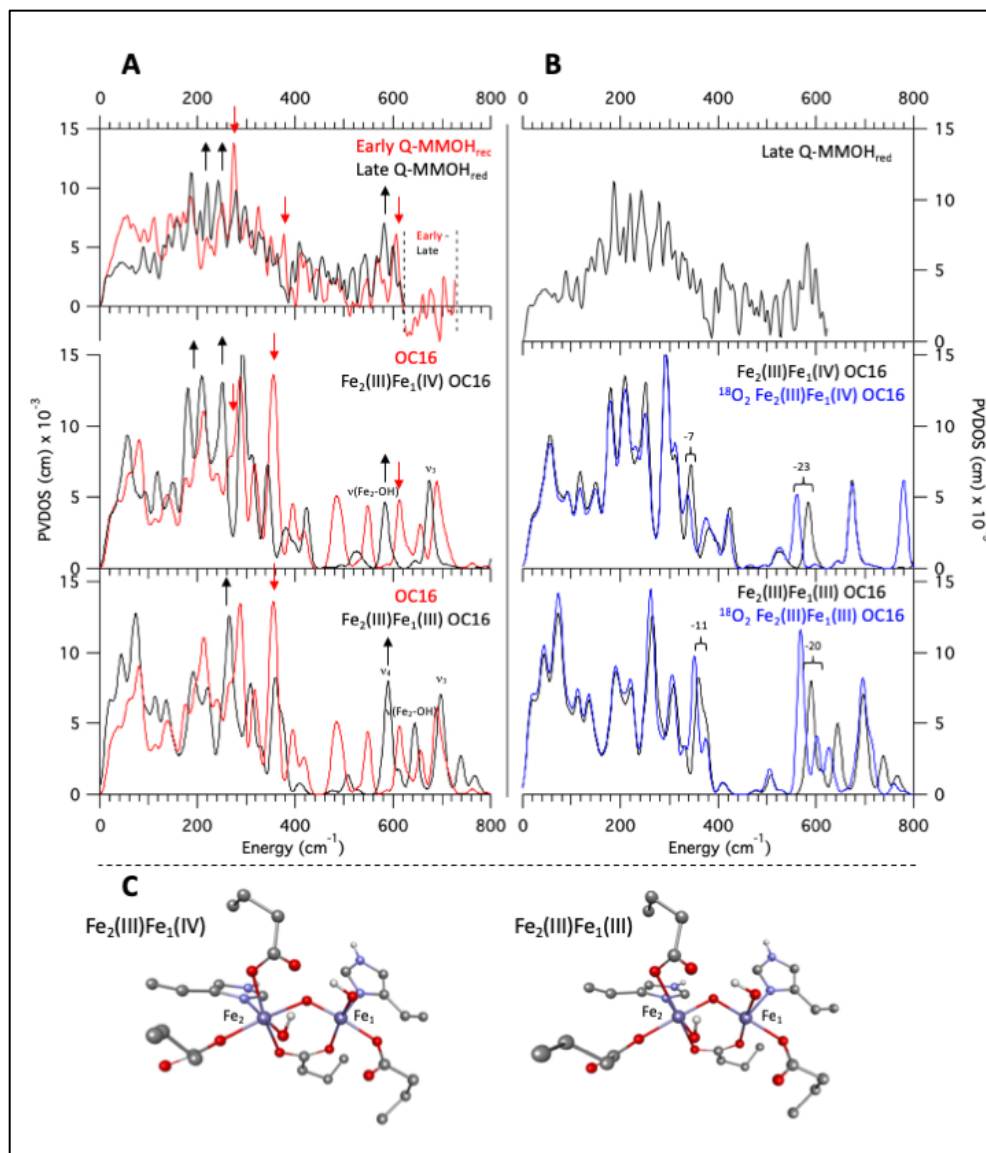


Figure S27 DFT-calculated cryoreduced NRVS spectra of **OC32**. All calculated spectra reported using B3LYP. Arrows indicate major differences between spectra. (A) Top: Experimental Early Q – MMOH_{red} (red spectrum) and Late Q-MMOH_{red} (black spectrum) NRVS data. 2nd from top: NRVS spectra for **OC32** (red) and its Fe₂(III)Fe₁(IV) congener (black). 2nd from bottom: NRVS spectra **OC32** (red) and its Fe(III)₂ congener (black). Bottom: NRVS spectra for **OC32** (red) and a 40%/60% mixture of the Fe₂(III)Fe₁(IV) and Fe(III)₂ spectra, respectively (**OC32 Decay**). (B) Top: Late Q-MMOH_{red} NRVS spectrum. 2nd from top: NRVS spectra of **OC32** Fe₂(III)Fe₁(IV) (black) and its ¹⁸O₂ isotopomer (blue). 2nd from bottom: NRVS spectra of **OC32** Fe(III)₂ (black) and its ¹⁸O₂ isotopomer (blue). Bottom: NRVS spectra of **OC32 Decay** (black) and its ¹⁸O₂ isotopomer (blue). The ν_3 (Figure 4, middle) mode is indicated, which decreases in energy in the Fe(III)₂ congener due to elongation of the Fe₁-OH bond. Note that even though the 600 cm⁻¹ feature in **OC32 Decay** is the ν_3 mode, it is too high in energy in **OC32** (~ 700 cm⁻¹) to be assigned the 605 cm⁻¹ feature in the Early Q – MMOH_{red} spectrum. (C) Geometry optimized Fe₂(III)Fe₁(IV) and Fe(III)₂ cryoreduced models of **OC32**.

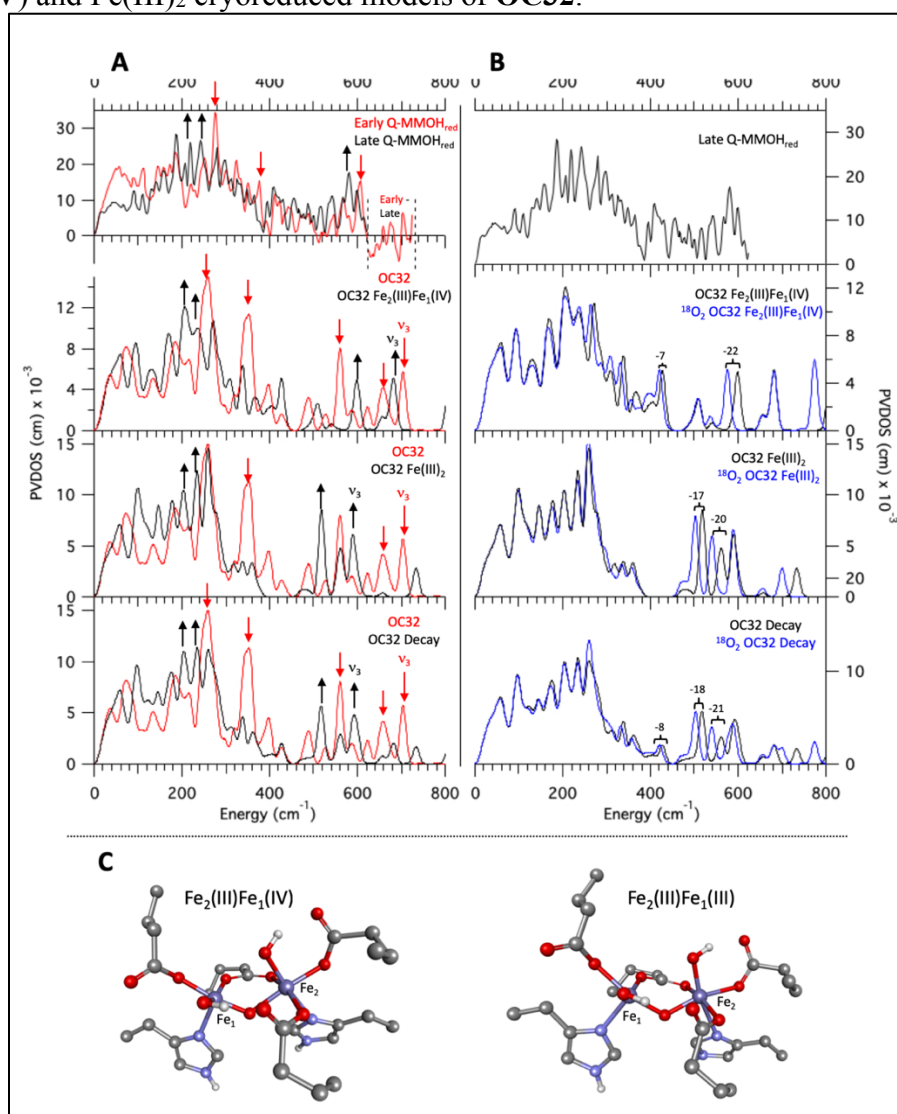


Figure S28 Badger's rule analysis for determination of the Fe₁-OH bond length required for a 605 cm⁻¹ vibration in OC -OH/-OH models. Several Fe(IV)-OH bond lengths from OC -OH/-OH models (and Fe(III)-OH bond lengths from cryoreduced models) were plotted against their “normalized” frequencies ($\nu_{\mu} = \frac{\nu}{\mu}$).²⁶ The rR-assigned ν_1 mode of **OC16** using B3LYP (685 cm⁻¹; see Figure 7B, middle) was used as an internal calibrant (Fe₂-OH = 1.774 Å). Blue dots indicate experimental data reported for Fe(III)-OH vibrations.²⁷ Red dots and black dots reflect Fe(IV)-OH and Fe(III)-OH bonds for OC -OH/-OH models and their calculated cryoreduced structures, respectively.

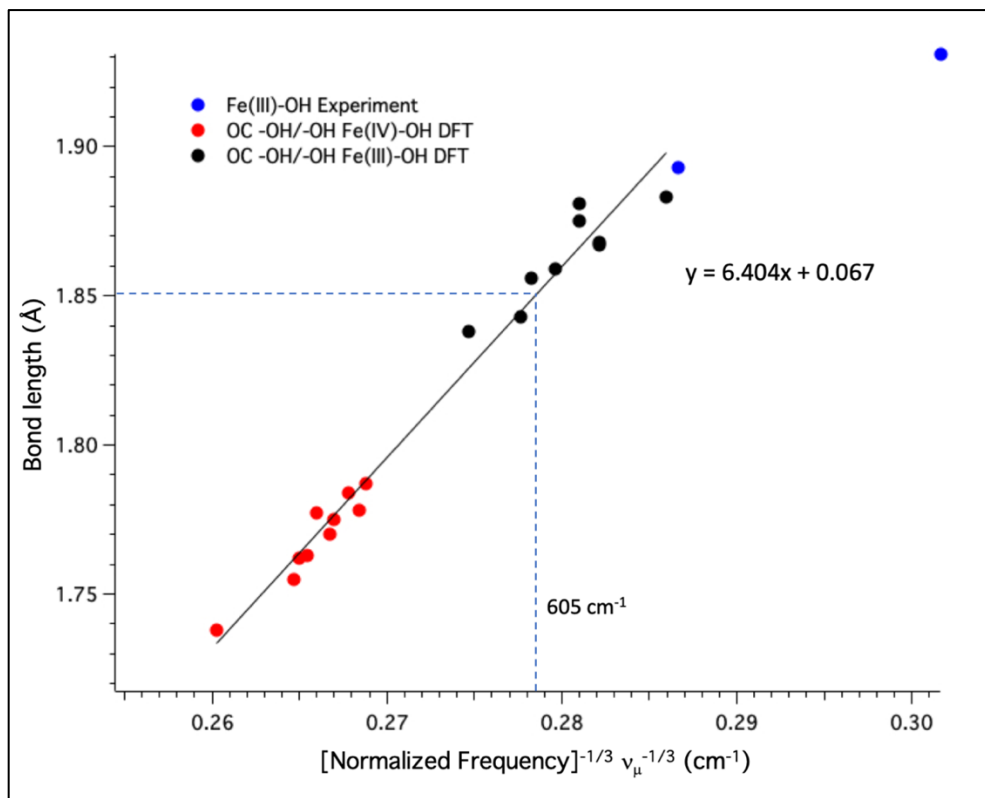


Figure S29 NRVS spectra for cryoreduced **bis(μ O)-H₂O-6** models calculated in B3LYP. Fe(III)₂Fe(IV)₁ lower in energy than Fe₂(IV)Fe₁(III) by 2.8 kcal. Arrows indicate major changes between spectra. (A) (i) Early Q – MMOH_{red} (red) and Late Q – MMOH_{red} (black) NRVS data. (ii) NRVS spectra **bis(μ O)-H₂O-6** (red) and **bis(μ O)-H₂O-6** Fe₂(III)Fe₁(IV) (black). (iii) NRVS spectra **bis(μ O)-H₂O-6** (red) and **bis(μ O)-H₂O-6** Fe(III)₂ (black). (B) (i) Late Q – MMOH_{red} data (black) ¹⁸O₂ shifts in inset. (ii) NRVS spectrum for **bis(μ O)-H₂O-6** Fe₂(III)Fe₁(IV) (black) and its ¹⁸O₂ labeled isotopomer (blue). (iii) NRVS spectrum for **bis(μ O)-H₂O-6** Fe(III)₂ (black) and its ¹⁸O₂ labeled isotopomer (blue).

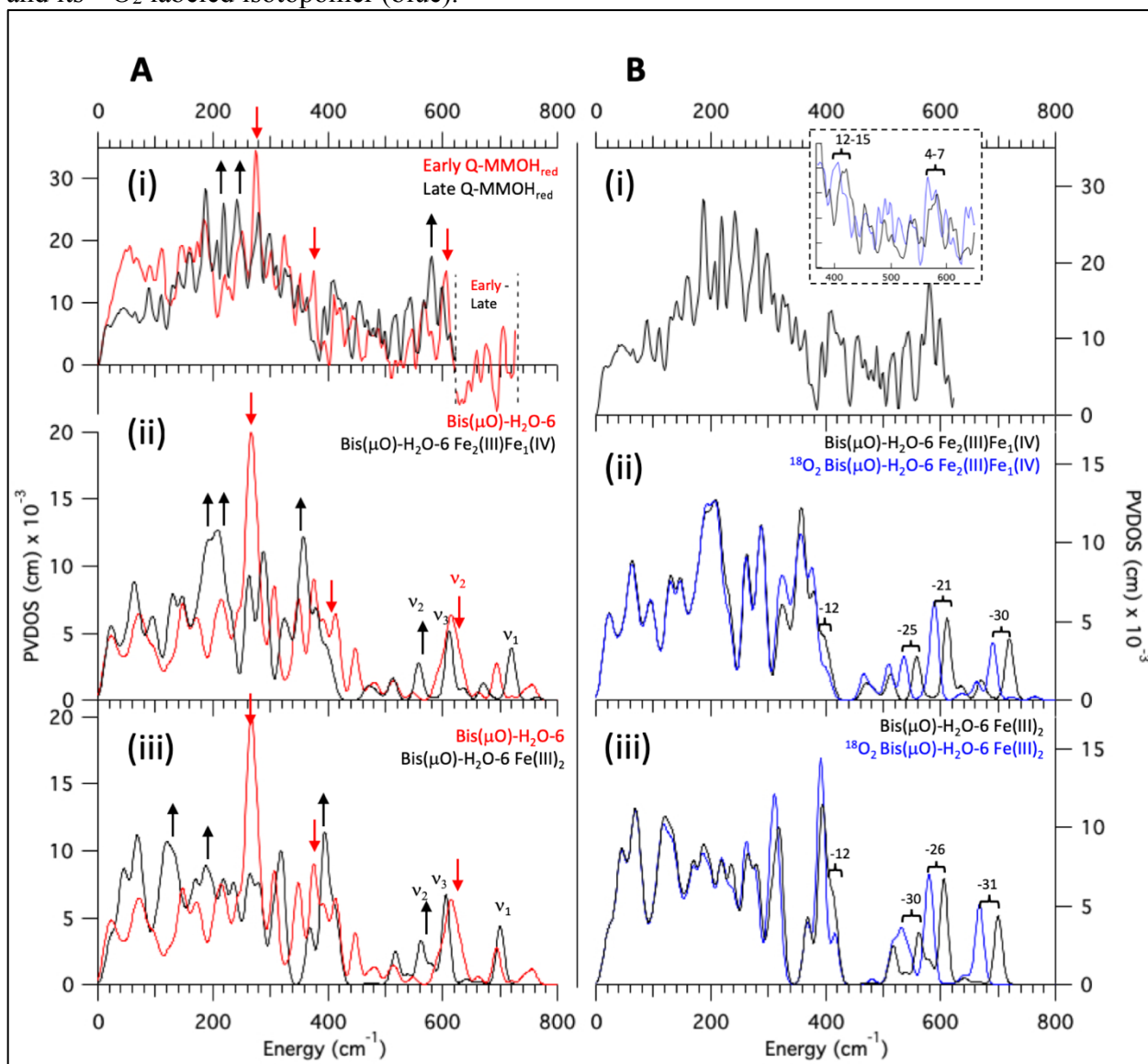


Figure S30 NRVS spectra for cryoreduced **bis(μ O)-OH-12** models calculated in B3LYP. $\text{Fe(III)}_2\text{Fe(IV)}_1$ lower in energy than $\text{Fe}_2\text{(IV)Fe}_1\text{(III)}$ by 1.5 kcal. Arrows indicate major changes between spectra. (A) (i) Early Q – MMOH_{red} (red) and Late Q – MMOH_{red} (black) NRVS data. (ii) NRVS spectra **bis(μ O)-OH-12** (red) and **bis(μ O)-OH-12** $\text{Fe}_2\text{(III)Fe}_1\text{(IV)}$ (black). (iii) NRVS spectra **bis(μ O)-OH-12** (red) and **bis(μ O)-OH-12** $\text{Fe}_2\text{(IV)Fe}_1\text{(III)}$ (black). (iv) NRVS spectra **bis(μ O)-OH-12** (red) and **bis(μ O)-OH-12** Fe(III)_2 (black) (B) (i) Late Q – MMOH_{red} data (black) $^{18}\text{O}_2$ shifts in inset. (ii) NRVS spectrum for **bis(μ O)-OH-12** $\text{Fe}_2\text{(III)Fe}_1\text{(IV)}$ (black) and its $^{18}\text{O}_2$ labeled isotopomer (blue). (iii) NRVS spectrum for **bis(μ O)-OH-12** $\text{Fe}_2\text{(IV)Fe}_1\text{(III)}$ (black) and its $^{18}\text{O}_2$ labeled isotopomer (blue). (iv) NRVS spectrum for **bis(μ O)-OH-12** Fe(III)_2 (black) and its $^{18}\text{O}_2$ labeled isotopomer (blue).

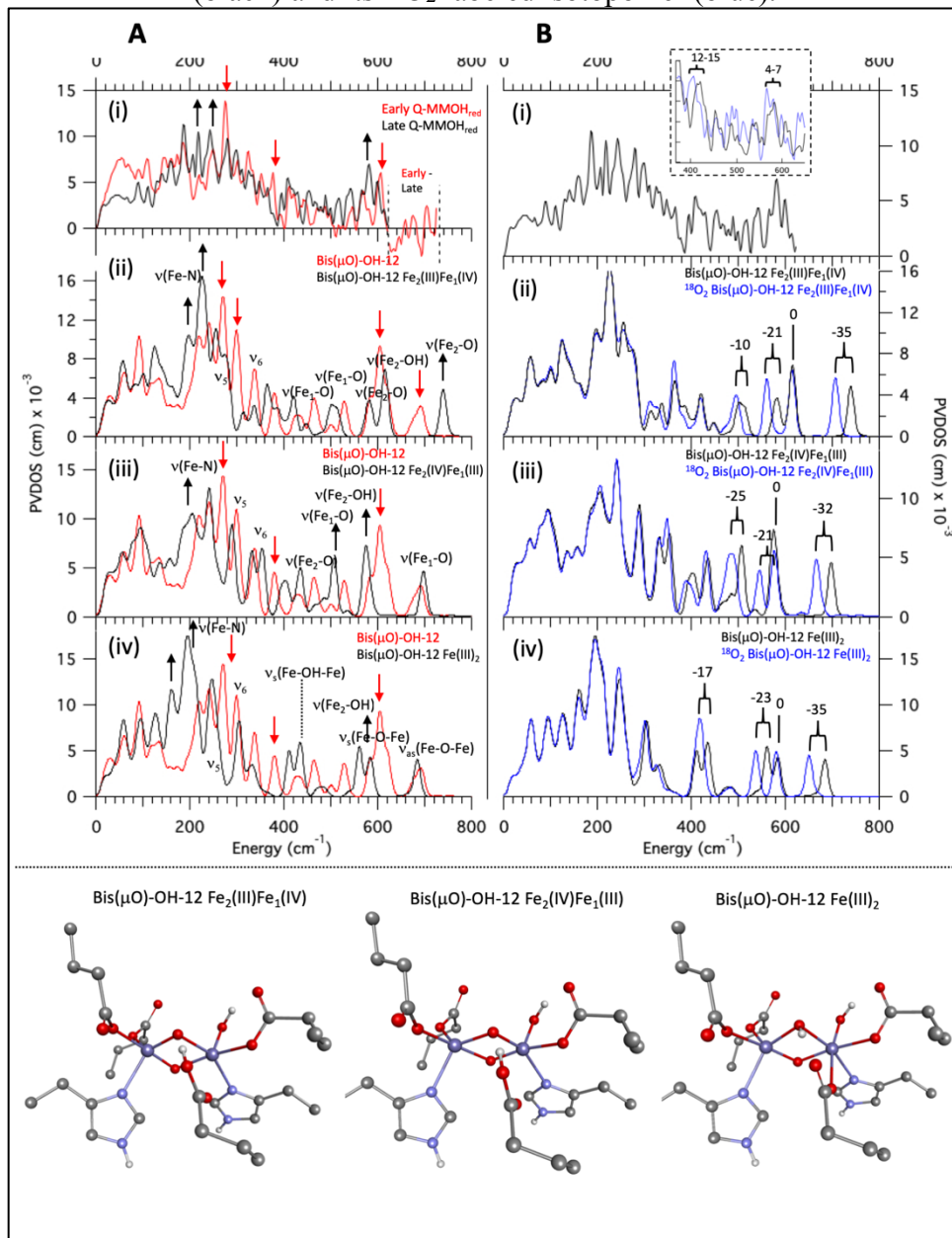


Table S13 Selected bond lengths for **bis(μ O)-OH-12** (B3LYP optimized) and its cryoreduced models.

	Q	Fe ₂ (III)Fe ₁ (IV)	Fe ₂ (IV)Fe ₁ (III)	Fe(III) ₂
Fe ₁ - N(His246)	2.174	2.210	2.171	2.216
Fe ₁ - O(Glu209)	1.845	1.903	1.938	1.998
Fe ₁ - O(Glu243)	1.88	1.942	1.927	1.964
Fe ₁ -O(H)	1.794	1.793	1.921	2.034
Fe ₁ -O	1.785	1.709	1.969	1.803
Fe ₂ - N(His147)	2.139	2.216	2.222	2.286
Fe ₂ - O(Glu114)	1.885	2.040	1.967	2.167
Fe ₂ - O(Glu144)	2.504	2.384	2.657	2.191
Fe ₂ -OH	1.837	1.849	1.869	1.879
Fe ₂ -O(H)	1.876	2.018	1.857	2.100
Fe ₂ -O	1.793	1.990	1.720	1.875

Comparison of bis(μ O)-OH models:

Of the bis(μ O)-OH models that can be correlated to all spectral data on Q (**bis(μ O)-OH 11-14, 16**), models **bis(μ O)-OH-11** and **12** have close to identical structures and are considered together (Figure 10, left). Models **bis(μ O)-OH-13-15** possess a highly rotated Glu144 residue which is no longer bound to either iron, and likely not a reasonable structural change during the catalytic cycle (see Table S1 for their structures). This leaves models **bis(μ O)-OH-12** and **16** (Figure 10, right) as possible structural assignments of Q. These models share a similar active site arrangement, with His246 as well as Glu243 and Glu209 coordinated monodentate to Fe₁, and His147, monodentate Glu114 and Glu144 protonated and hydrogen-bonded to a μ -O bridge all coordinated to the Fe₂-OH. In **bis(μ O)-OH-12**, the Fe₂-O(Glu144) bond distance is long (2.50 Å) indicating a weak bond, whereas in **bis(μ O)-OH-16** this bond is shorter (2.19 Å). However, in **bis(μ O)-OH-16**, the shorter Fe₂-O(Glu144) bond results in a stronger hydrogen bond between this protonated Glu144 and the μ -O bridge, which weakens this equatorial μ -O bond and results in a shorter Fe₂-OH bond (1.78 Å in **bis(μ O)-OH-16**, vs. 1.83 Å in **12**). This leads to a $\nu(\text{Fe}_2\text{-OH})$ mode that is higher in energy (656 cm⁻¹, see Figure S31) than the 605 cm⁻¹ NRVS feature in Q. Therefore, Q likely has a structure in-between **bis(μ O)-OH-12** and **16**, in which the Glu144 residue is bound to Fe₂ but weak enough to result in a relatively weak Fe₂-OH bond.

Figure S31 NRVS spectra for cryoreduced **bis(μ O)-OH-16** models calculated in B3LYP. $\text{Fe}_2(\text{IV})\text{Fe}_1(\text{III})$ lower in energy than $\text{Fe}_2(\text{III})\text{Fe}_1(\text{IV})$ by 5.6 kcal. Arrows indicate major changes between spectra. (A) (i) Early Q – MMOH_{red} (red) and Late Q – MMOH_{red} (black) NRVS data. (ii) NRVS spectra **bis(μ O)-OH-16** (red) and **bis(μ O)-OH-16** $\text{Fe}_2(\text{IV})\text{Fe}_1(\text{III})$ (black). (iii) NRVS spectra **bis(μ O)-OH-16** (red) and **bis(μ O)-OH-16** $\text{Fe}(\text{III})_2$ (black) (iv) NRVS spectra **bis(μ O)-OH-16** (red) and **bis(μ O)-OH-16 Decay** (black); **bis(μ O)-OH-16 Decay** derived from a 40%/60% mixture of **bis(μ O)-OH-16** $\text{Fe}_2(\text{IV})\text{Fe}_1(\text{III})$ and **bis(μ O)-OH-16** $\text{Fe}(\text{III})_2$. (B) (i) Late Q – MMOH_{red} data (black) $^{18}\text{O}_2$ shifts in inset. (ii) NRVS spectrum for **bis(μ O)-OH-16** $\text{Fe}_2(\text{IV})\text{Fe}_1(\text{III})$ (black) and its $^{18}\text{O}_2$ labeled isotopomer (blue). (iii) NRVS spectrum for **bis(μ O)-OH-16** $\text{Fe}(\text{III})_2$ (black) and its $^{18}\text{O}_2$ labeled isotopomer (blue). (iv) NRVS spectrum for **bis(μ O)-OH-16 Decay** (black) and its $^{18}\text{O}_2$ labeled isotopomer (blue).

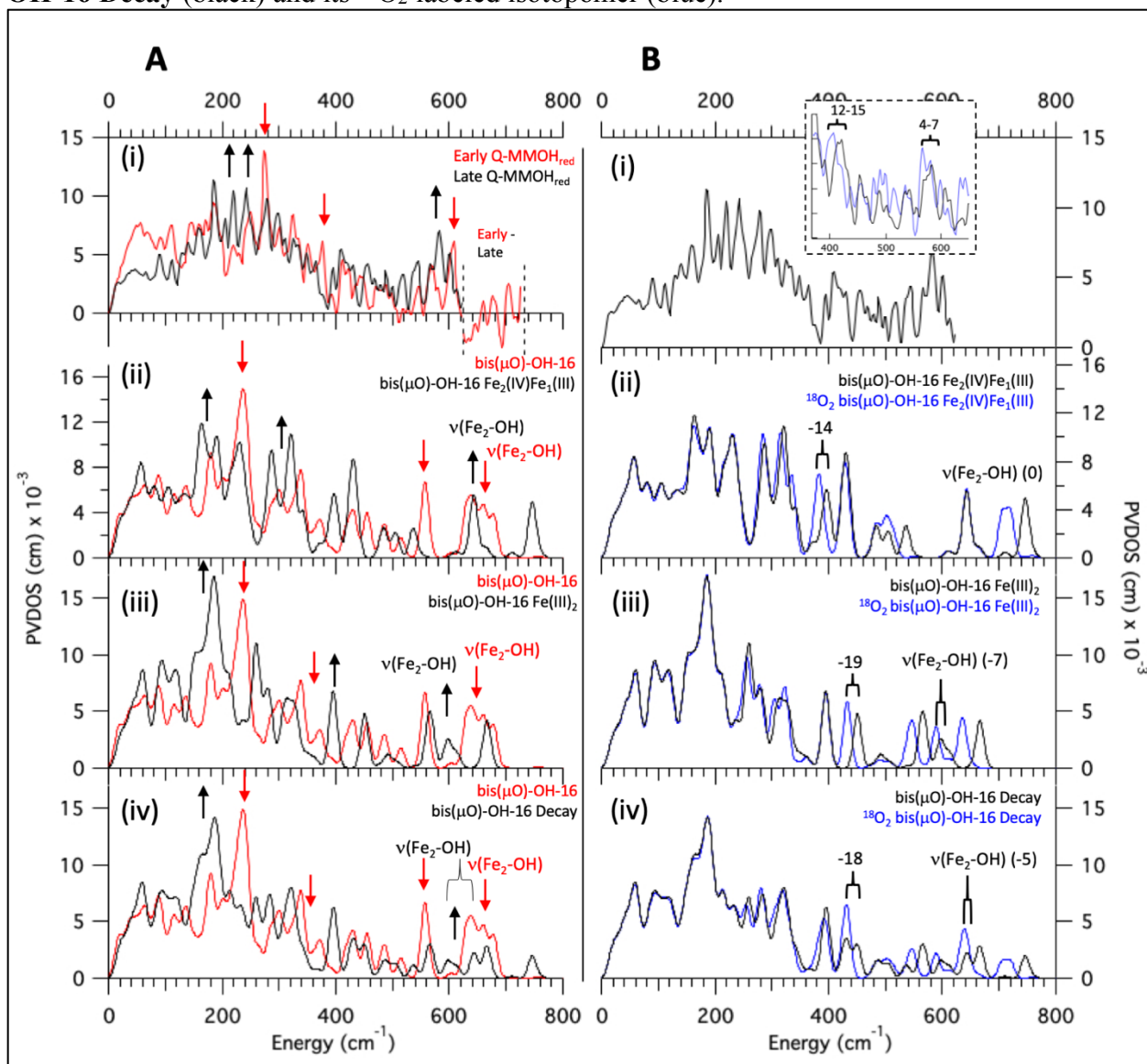


Figure S32 Derivation of Q models from the recently published XFEL MMOB-associated MMOH *M. trichosporium* OB3b structure.²⁸ A) Overlay of **bis(μ O)-H₂O-1** optimized (B3LYP/6-31g(d)) from the XFEL (orange) and *M. capsulatus* Bath cryo-crystal structure⁹ (green). B) Computed NRVS spectra of **bis(μ O)-H₂O-1** from XFEL (orange) and cryo-crystallography (green) show negligible differences. C) Computed NRVS spectra of **OC15** from XFEL (red) and cryo-crystallography (black), and D) computed NRVS spectra of **bis(μ O)-OH-12** from XFEL (red) and cryo-crystallography (black) show only minor differences in intensity at low (< 300 cm⁻¹) energy.

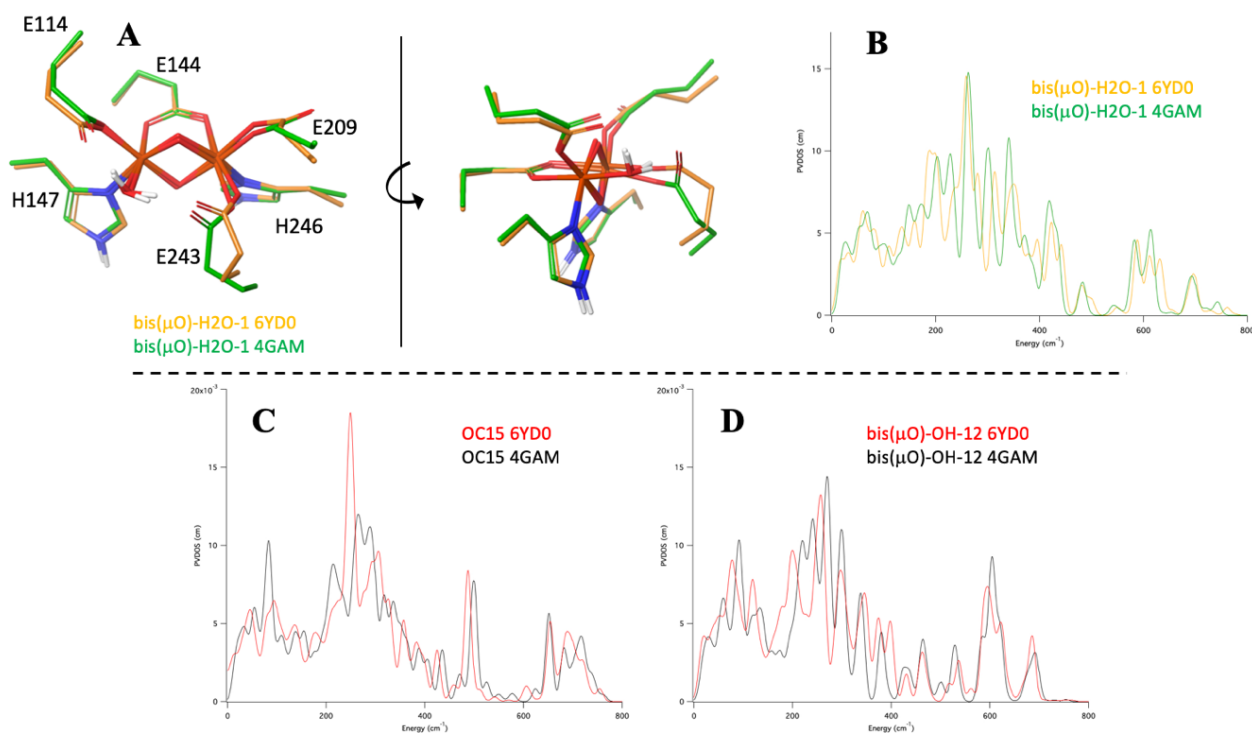


Figure S33 H-bond effect on the potential energy, enthalpy, and free energy of the HAT product of the OC -OH/=O reaction with CH₄.

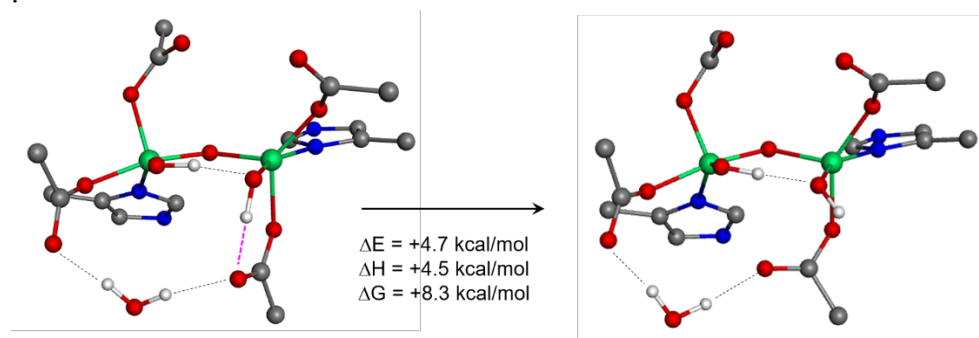


Figure S34 H-atom abstraction from CH₄ by the hypothetical Fe(IV)-OH system in SyrB2. (a) Reaction scheme. (b) Potential energy, enthalpy, and free energy changes and intrinsic barriers. (c) Geometry and Mayer bond order changes over H atom abstraction.

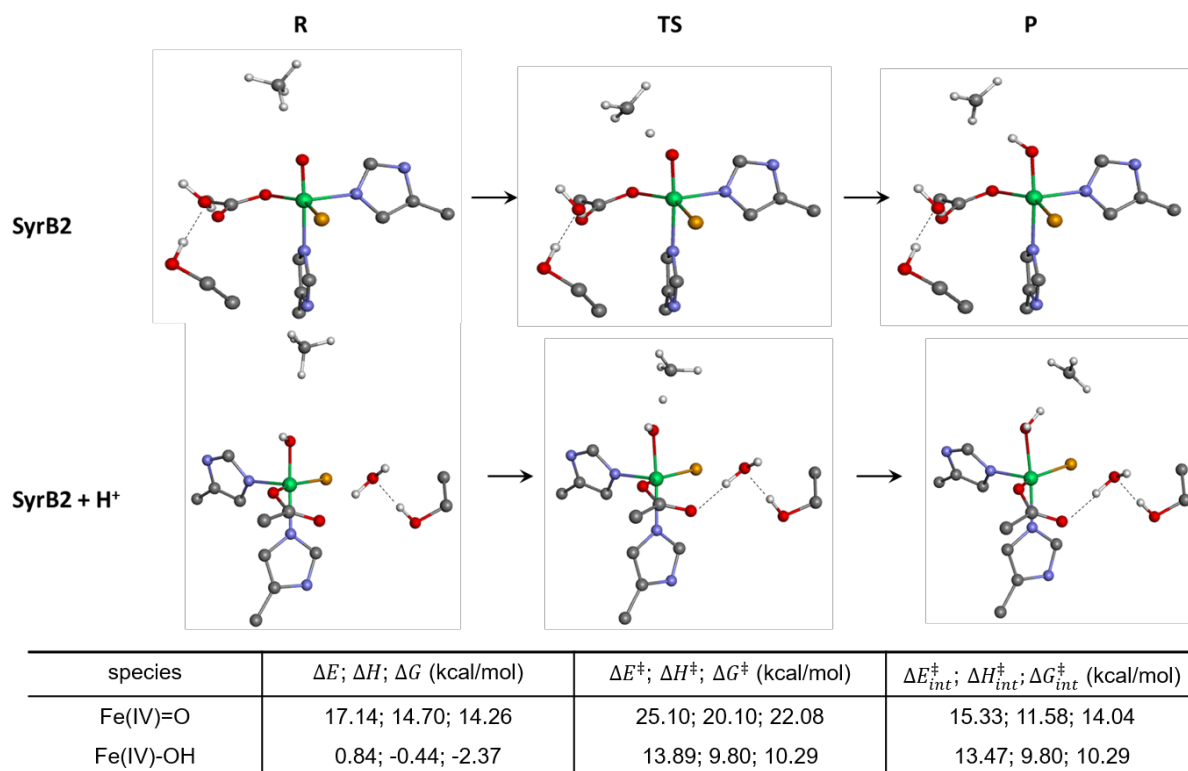
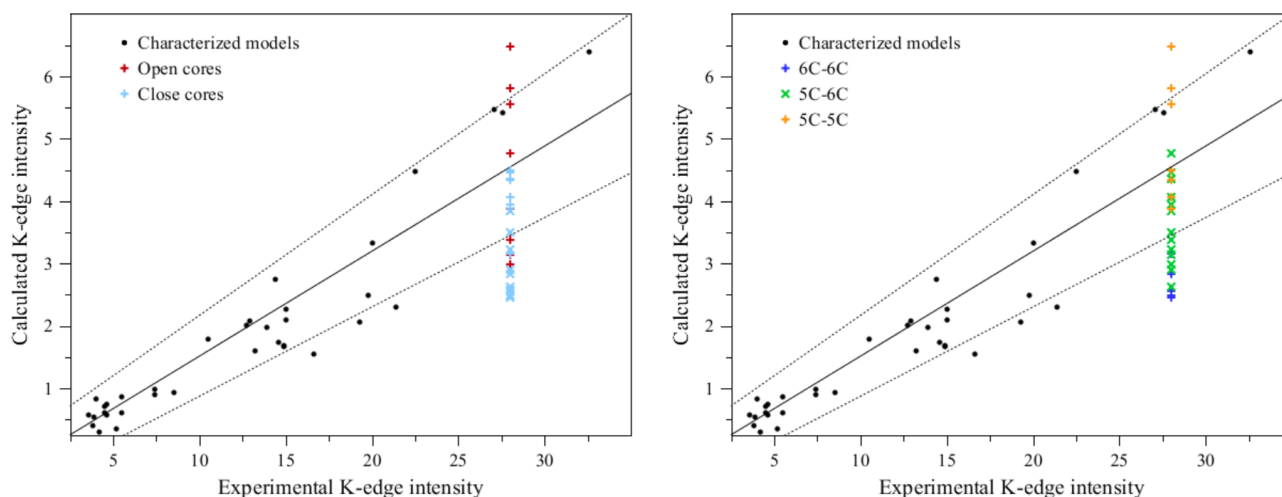


Table S14 Calculation of Mössbauer parameters for Q models. The Mössbauer parameters were calculated using ORCA version 4.0.1.2 using the B3LYP functional and the CP(PPP) basis set for the iron atom and def2-TZVPP for the other atoms along with the auxiliary basis set def2/J. The calibration of the isomer shift for this functional and basis set published by Römelt et al. was used.²⁹ Experimental values for δ and ΔE_Q are given at the top table for OB3b and Bath, and compared to calculated values below. An additional model **bis(μ O)-OH-16-H₂O** has been included which incorporates an additional, unbound H₂O ligand hydrogen-bonded to Fe₂-OH in **bis(μ O)-OH-16**. This model contains a long Fe₂-Glu144 bond (2.37 Å) compared to **bis(μ O)-OH-16** (2.19 Å), and a larger $\Delta E_{Q1}-\Delta E_{Q2}$ (0.60 vs. 0.17, respectively).

		δ_1	δ_2	$ \delta_1-\delta_2 $	ΔE_{Q1}	ΔE_{Q2}	$ \Delta E_{Q1}-\Delta E_{Q2} $
	Experiment	(mm/s)	(mm/s)	(mm/s)	(mm/s)	(mm/s)	(mm/s)
	Q (OB3b)	0.17	0.17	0.0	0.53	0.53	0.0
	Q (Bath)	0.21	0.14	0.07	0.68	0.55	0.13
Model Type	Model Name	δ_1	δ_2	$ \delta_1-\delta_2 $	ΔE_{Q1}	ΔE_{Q2}	$ \Delta E_{Q1}-\Delta E_{Q2} $
		(mm/s)	(mm/s)	(mm/s)	(mm/s)	(mm/s)	(mm/s)
bis(μO)-H₂O	bis(μ O)-H ₂ O-1	0.17	0.13	0.04	0.46	0.66	0.20
	bis(μ O)-H ₂ O-2	0.17	0.13	0.04	0.43	0.74	0.31
	bis(μ O)-H ₂ O-3	0.16	0.13	0.03	0.50	0.73	0.23
	bis(μ O)-H ₂ O-4	0.21	0.11	0.10	0.42	0.59	0.16
	bis(μ O)-H ₂ O-6	0.12	0.12	0.00	0.46	0.78	0.33
	bis(μ O)-H ₂ O-8	0.09	0.12	0.03	-0.78	0.53	0.25
	bis(μ O)-H ₂ O-10	0.12	0.12	0.00	-0.40	-0.39	0.01
	bis(μ O)-H ₂ O-11	0.15	0.14	0.01	0.68	-0.78	0.10
bis(μO)-OH	bis(μ O)-H ₂ O-13	0.16	0.18	0.02	-1.01	1.05	0.04
	bis(μ O)-OH-9	0.17	0.07	0.10	-0.88	-0.52	0.36
	bis(μ O)-OH-10	0.07	0.11	0.04	-0.25	0.44	0.19
	bis(μ O)-OH-12	0.10	0.12	0.02	0.37	-1.42	1.05
	bis(μ O)-OH-13	0.08	0.06	0.02	0.55	0.84	0.29
	bis(μ O)-OH-14	0.08	0.07	0.01	-0.26	-0.74	0.48
	bis(μ O)-OH-15	0.12	0.06	0.04	0.49	-1.34	0.84
	bis(μ O)-OH-16	0.10	0.12	0.02	-0.45	0.62	0.17
bis(μO)	bis(μ O)-OH-16-(H ₂ O)	0.12	0.16	0.04	0.46	1.06	0.60
	bis(μ O)-1	0.16	0.10	0.06	0.45	-0.71	0.26
OC -OH/=O	bis(μ O)-6	0.13	0.20	0.07	0.91	-0.64	0.28
	OC01	0.17	0.09	0.08	-0.34	0.63	0.30
	OC03	0.12	0.07	0.05	-0.26	0.79	0.53
	OC17	0.16	0.03	0.13	1.03	-0.67	0.36
OC -OH/-OH	OC26	0.09	0.12	0.03	0.49	0.45	0.04
	OC10	0.06	0.05	0.01	0.44	-0.77	0.33
	OC15	0.11	0.03	0.08	-0.39	-0.61	0.22
	OC16	0.11	0.01	0.10	-0.41	0.49	0.08
	OC32	0.05	0.11	0.06	0.35	-0.61	0.26

Figure S35 TD-DFT Fe K-edge calibration and calculations for models of Q. In order to calibrate the TD-DFT methodology, TD-DFT Fe K-edge XAS spectra were simulated for model complexes whose crystal structure and experimental Fe K-edge XAS have been previously published.^{30–34} These data (black dots) show a linear correlation between calculations and experiment (solid line) with their standard deviation plotted (dotted lines). The total intensity is reproduced by the TD-DFT simulations, allowing their use as a calibration for calculating the TD-DFT Fe K-edge intensity of models for Q. The experimental pre-edge intensity of Q is 28,³⁵ and the calculated intensities of different computational models were plotted against this value (colored symbols) at 28 on the x-axis. Both open and closed core models are predicted to show variable pre-edge intensity depending on their core structure (left). However, all open and closed core Q models possessing two 6C sites are predicted to have unreasonably low K-edge intensity (right; blue diamonds), whereas both 5C-6C (right; green “x”) and 5C-5C (right; orange “+”) models of Q are predicted to exhibit K-edge intensity in agreement with the experimental data.



Below, the effect of model coordination vs. pre-edge shape is also provided. Top: Experimental HERFD Fe K-edge XAS spectrum of Q,³ digitized. (Bottom) TD-DFT calculated spectra of a few representative

models with different coordination number: bis(μ O)-OH8 (6C-6C), bis(μ O)-OH16 (5C-6C), OC32 -OH/-OH (5C-6C), bis(μ O)-OH13 (5C-5C) and OC10 -OH/-OH (5C-5C). A shift of 150.8 eV was applied in the calculated energy, identical to the one determined with the functional B3LYP.³

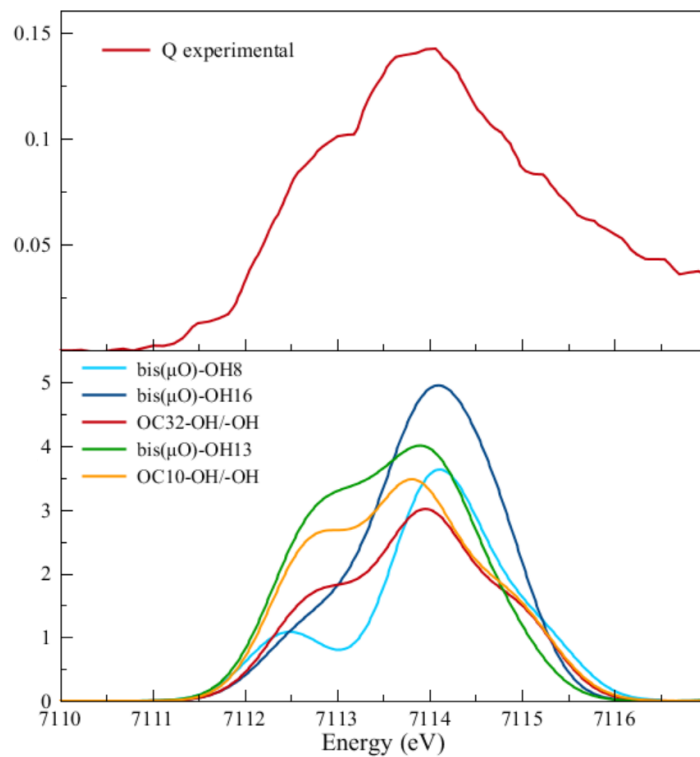


Table S15 A) DFT calculated energies for the A_g breathing mode in $^{16}\text{O}_2$, $^{16}\text{O}^{18}\text{O}$, and $^{18}\text{O}_2$ labeled bis(μO)-OH models of Q constrained to possess an Fe-Fe distance of 3.0 Å.

Model (Fe-Fe = 3.0 Å)	A_g $^{16}\text{O}_2$ (cm^{-1})	A_g $^{16}\text{O}^{18}\text{O}$ (cm^{-1})	A_g $^{18}\text{O}_2$ (cm^{-1})
bis(μO)-OH-12	636	626	612
bis(μO)-OH-14	637	628	616
bis(μO)-OH-15	650	641	625

Table S15 B) DFT calculated energies for the A_g breathing mode in $^{16}\text{O}_2$, $^{16}\text{O}^{18}\text{O}$, and $^{18}\text{O}_2$ labeled bis(μO)-OH models of Q for geometry optimized structures (compare to Table S15A).

Model	A_g $^{16}\text{O}_2$ (cm^{-1})	A_g $^{16}\text{O}^{18}\text{O}$ (cm^{-1})	A_g $^{18}\text{O}_2$ (cm^{-1})
bis(μO)-OH-12 (Fe-Fe = 2.76 Å)	676	667	635
bis(μO)-OH-14 (Fe-Fe = 2.73 Å)	700	690	663
bis(μO)-OH-15 (Fe-Fe = 2.75 Å)	693	676	667

Figure S36 NRVs spectra of bis(μ O)-OH12 (A), bis(μ O)-OH14 (B), and bis(μ O)-OH15 (C), optimized with B3LYP (red spectra) and optimized while freezing the Fe-Fe distance to 3 Å (black spectra).

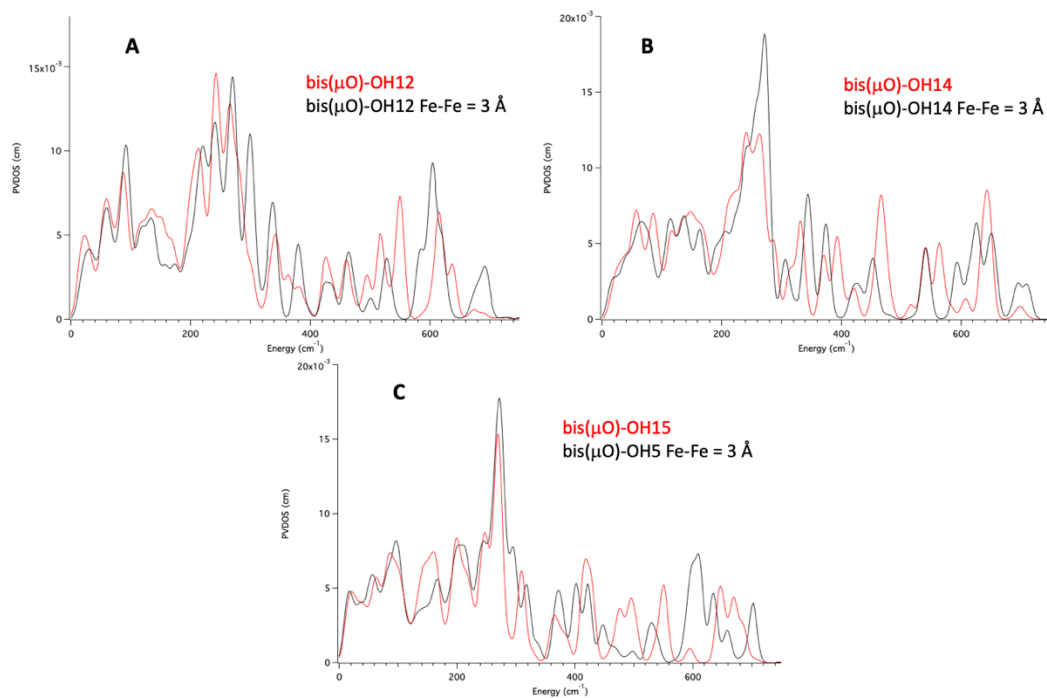


Figure S37 Geometry and Mayer bond order changes over H atom abstraction from CH₄ by the mononuclear Fe(IV)=O system.

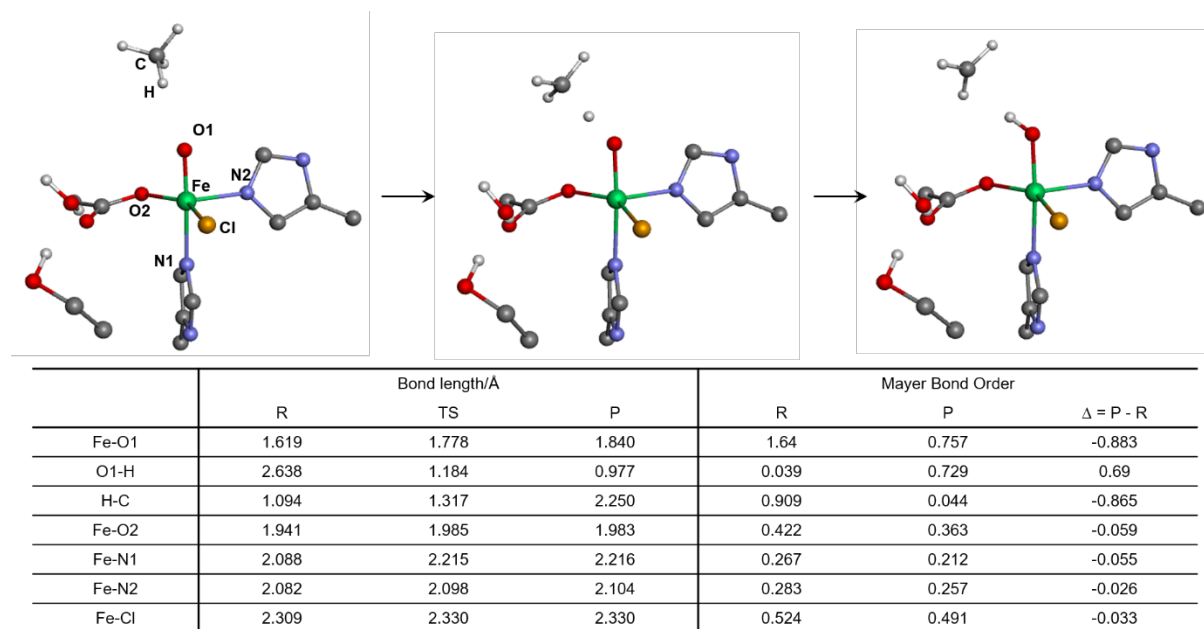
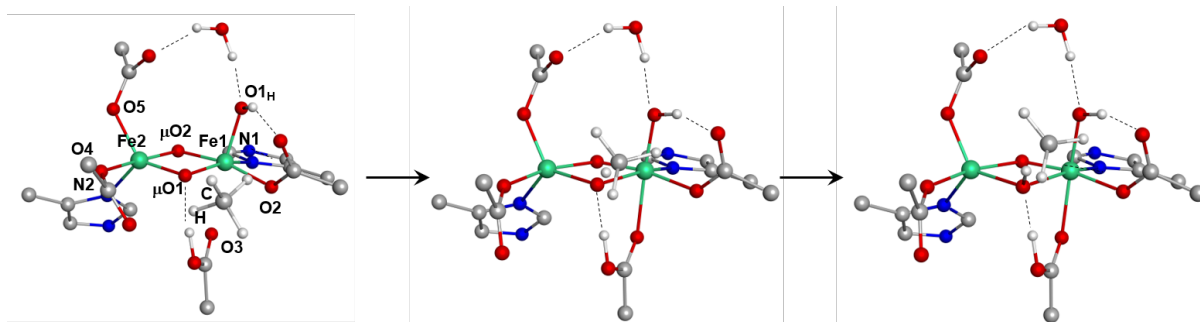


Figure S38 Geometry and Mayer bond order changes over H atom abstraction from CH₄ by the binuclear closed core model, bis(μ O)-OH12



	Bond length/Å			Mayer Bond Order		
	R	TS	P	R	P	$\Delta = P - R$
Fe1- μ O1	1.857	2.176	2.219	0.635	0.202	-0.433
Fe1- μ O2	1.804	1.701	1.690	0.674	1.137	0.463
Fe2- μ O1	1.799	1.982	2.060	0.804	0.317	-0.487
Fe2- μ O2	1.779	1.940	1.954	0.776	0.395	-0.381
μ O1-H	3.797	1.249	0.979	0.002	0.704	0.702
H-C	1.094	1.280	2.260	0.917	0.048	-0.869
Fe1-O1 _H	1.857	1.802	1.799	0.694	0.81	0.116
Fe1-O2	1.890	1.918	1.926	0.459	0.388	-0.071
Fe1-O3	2.486	2.155	2.125	0.083	0.203	0.12
Fe1-N1	2.114	2.187	2.181	0.282	0.241	-0.041
Fe2-O4	1.848	1.880	1.882	0.535	0.462	-0.073
Fe2-O5	1.897	1.898	1.896	0.278	0.274	-0.004
Fe2-N2	2.174	2.140	2.123	0.481	0.441	-0.04

Figure S39 (a) Reaction scheme, (b) potential energy surface (PES), and (c) energy profile for the conversion of CH₄ to CH₃OH by **bis(μO)-OH12**. After the hydrogen atom transfer from CH₄, the rebound of the CH₃• radical is associated with the opening of the μOH bridge. The PES in (b) shows that the O-C bond formation and the Fe₂(III)-μOH bond cleavage are not concerted and TS2, Int2, and TS3 have almost identical electronic energies.

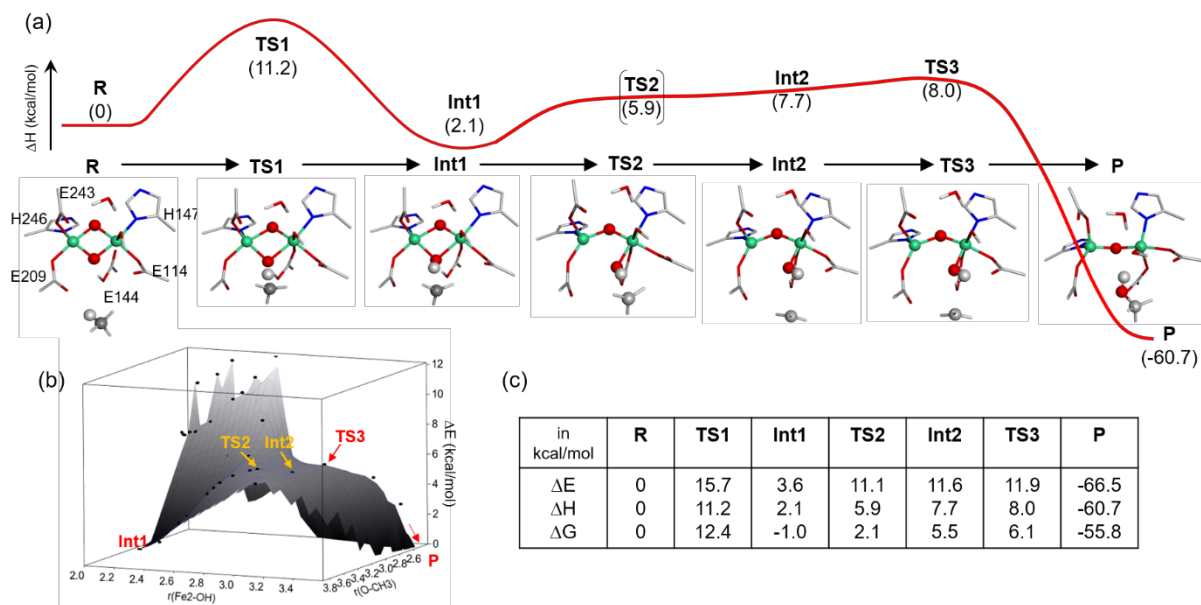


Figure S40 Energy profiles for the H atom abstraction from CH₄ by the out-of-plane OH group (top) and the in-plane OH group (bottom) of OC15.

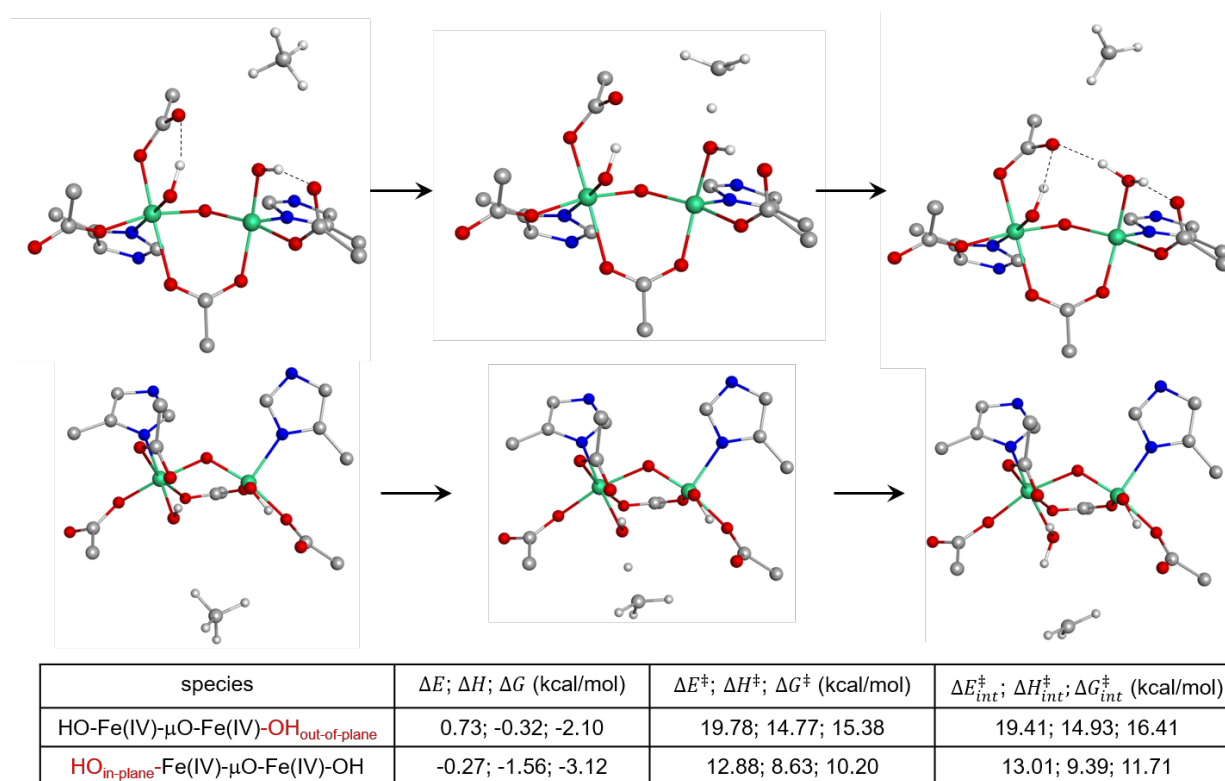


Figure S41 (a) Reaction scheme and (b) energy profile for the conversion of CH₄ to CH₃OH by OC15.

